Numerical Analysis of Oil Injection in Twin-Screw Compressors

Nausheen Basha

School of Mathematics, Computer Science and Engineering

Centre for Compressor Technology
Northampton Square, London, EC1V 0HB, U.K.

This dissertation is submitted for the degree of

Doctor of Philosophy

July 2021

I would like to dedicate this thesis to my loved ones …

Declaration

I hereby declare that except where specific reference is made to the work of others, the contents of this dissertation are original and have not been submitted in whole or in part for consideration for any other degree or qualification in this or any other university. This dissertation is my own work and contains nothing which is the outcome of work done in collaboration with others, except where specified in the text.

Nausheen Basha

July 2021

Acknowledgements

I would like to thank my supervisor Prof. Kovacevic, whose joy and enthusiasm for research has been contagious and motivational for me, even during tough times of my PhD pursuit. I am also thankful for the excellent example he has provided during my time at City, University of London. I would like to acknowledge Prof. Stosic's help and input throughout my work.

The past 3+ years have been interesting, to say the least. I would like to start by thanking my friends in the Centre for Compressor Technology at City, University of London. Afia, Yang, Sham, Sunny, Suraj and Sun– without their constant support, advices, agreement to drinking coffee at any time of the day and night, empathy, and genuine care, this would have been challenging. I am very grateful to each one of them for the time spent with me and for creating lasting memories.

I gratefully acknowledge the support that I received from Prof. Matar working at Imperial College London. His unfeigned care and leadership have been very powerful during my writing phase. I would also like to thank Julia, who has not just been a great mentor but also an amazing enabler to think outside the box from different perspectives. And most of all, for my supporting, encouraging, and patient loved ones who were with me throughout this journey, thank you.

Nausheen Basha

City, University of London

July 2021

Abstract

Compressors are widely used in the manufacturing, process, construction, and energy industries. They consume nearly 20% of the electricity generated worldwide [1]. Nearly 66% of this electricity comes from burning fossil fuel that greatly impacts the environment. Improving compressor efficiency by even a small percentage will considerably reduce electricity and energy consumption. This thesis focuses on improvement in the efficiency of oil-injected compressors. The injection of oil in the working chamber of a screw compressor increases volumetric efficiency and reliability, but it increases power losses. Also, the oil needs to be separated from the gas, which requires additional equipment and energy losses, not to mention the contamination of the environment with the oil carryover. The injected oil has a significant influence on compressor performance and the environment.

The distribution of oil injected in a compression chamber is critical for performance and reliability. Accordingly, investigations are carried out using Computational Fluid Dynamics (CFD), based on a Volume of Fluid (VOF) model, to determine the oil distribution. The predictions were compared with test results. This was applied to an industrial compressor with a traditional single oil injection point. Using different nozzle diameters allowed the evaluation of the oil and temperature distribution close to rotor surfaces to be determined. It was found out that the high gas temperatures coincided with the regions of low oil concentration. With increasing the oil flow rate through a single port, the cooling of these hot spots was not achieved beyond a certain point unless the second oil-injection port was introduced on the opposite rotor. The injection through ports on both rotors reduced the compressor chamber temperature by 30°-35°C and the specific power by 1.8%. Furthermore, the adaptive mesh refinement technique in a simplified compression domain was used to simulate the film formation and disintegration. The disintegration has shown various oil phase breakup levels due to interfacial shear, inertial, and centrifugal forces, leading to ligaments, lobes, and droplets.

This study shows that computational methods could be exploited for improving compressor energy consumption through oil distribution. One such way is the enhancement of oil distribution to cool high temperature spots. Another is understanding the oil phase breakup due to the forces acting in a compression chamber that can affect the oil droplet sizes and cooling surface area. Techniques used in this research can be applied to improve efficiency for a wide range of screw compressors.

Table of Contents

List of Figures

List of tables

Nomenclature

A	area	m^2
c_p	specific heat capacity	J/kg/K
C_D	discharge coefficient	
C_d	drag coefficient	
d	port diameter	mm
e	error	
F	external body forces	N
f	field variable	
g	gravity	m/s^2
h	enthalpy	J
k	turbulent kinetic energy	m^2/s^2
$\dot{m}$	mass flow rate	kg/s
N	rotational speed	rpm
n	number frequency	
Oh	Ohnesorge number	
P	pressure	bar
PW	power	W
Q	volume flow rate of air	m^3/min
$\vec{R}$	Interphase momentum transfer	
Re	Reynolds number	
T	temperature	°C
t	time	s
v	velocity	m/s
We	Weber number	
w	specific power	W/m^3/min
y^+	non-dimensional wall distance	

Greek Symbols

α	volume fraction	
γ	specific heat ratio of air	
δ	thermal conductivity	W/mK
η	efficiency	

θ	male rotor angle	degrees
μ	dynamic viscosity	kg/ms
ρ	density	kg/m^3
τ	torque	Nm
ω	specific dissipation rate	m^2/s^3

Subscripts

air	air phase
ad	adiabatic
comp	compressor
dis	discharge
dr	drift
drop	droplet
g	gas
i	indicated
in	fluid domain inlet
l	liquid
m	mixture
oil	oil phase
out	fluid domain outlet

Acronyms

AMR	Adaptive mesh refinement
CFD	Computational Fluid Dynamics
SMD	Sauter mean diameter
SST	Shear Stress Transport
UDF	User Defined Functions
UDND	User Defined Nodal Displacement
VOF	Volume of Fluid

Publications

Journal Publications:

1. **N Basha**, A Kovacevic, S Rane. 'Analysis of Oil-Injected Twin-Screw Compressor with Multiphase Flow Models'. *Designs Journal*. 12.2019;3(4):54. doi: 10.3390/designs3040054.
2. Y Lu, A Kovacevic, M Read, **N Basha**. 'Numerical study of customised mesh for twin-screw vacuum pumps'. *Designs Journal*. 12.2019;3(4):52. doi:10.3390/designs3040052.
3. **N Basha**, A Kovacevic, S Rane. 'Numerical Investigation of Oil injection in Screw Compressors'. *Applied Thermal Engineering Journal*. 2021;193:116959 doi: 10.1016/j.applthermaleng.2021.116959

Peer-Reviewed Conference Proceedings:

1. **N Basha**, S Rane, A Kovacevic. 'Multiphase Flow Analysis in Oil-injected Twin Screw Compressor'. *3rd World Congress on Momentum, Heat and Mass Transfer (MHMT'18).* doi: 10.11159/icmfht18.132.
2. **N Basha**, A Kovacevic, N Stosic, I Smith. 'Effect of oil-injection on twin-screw compressor performance'. *IOP Conf. Series: Materials Science and Engineering* 425 (2018) 012009. doi:10.1088/1757-899X/425/1/012009.
3. **N Basha**, A Kovacevic, S Rane. 'User defined nodal displacement of numerical mesh for analysis of screw machines in Ansys Fluent'. *IOP Conf. Series: Materials Science and Engineering* 604 (2019) 012012. doi:10.1088/1757-899X/604/1/012012.
4. S Abdan, **N Basha**, A Kovacevic, N Stosic, A Birari, N Asati. 'Development and Design of Energy Efficient Oil-Flooded Screw Compressors'. *IOP Conf. Series: Materials Science and Engineering* 604 (2019) 012015. doi:10.1088/1757-899X/604/1/012015.
5. Y Lu, A Kovacevic, **N Basha**, M Read. 'CFD Analysis of Twin Screw Vacuum Pump with Ansys Fluent'. *9th International Conference on Compressor and Refrigeration, 2019, in Xi'an, China*.

Chapter 1 Introduction

1.1 Background

World energy consumption has increased drastically since the 1950s due to economic development, rising population and technological advancements. And it is expected to increase in the coming years, with EIA (US Energy Information Administration) projecting an increase of 50% from 2019 to 2050 [2]. The industrial sector is the largest consumer of energy, comprising more than 50%, and 85% of this energy comes from burning fossil fuels [3]. The remaining half are transportation, commercial and residential users (shown in Figure 1). This industrial sector includes refining, mining, manufacturing, agriculture, and construction, where most compressors are used. The world industrial sector in 2019 consumed around 259 trillion kJ (245 quadrillions Btu), which released 10 $GtCO_2$ per annum. This again is projected to increase by 30% from 2019 to 2050 [2][4]. In the UK alone, compressors consume 10% of industrial energy, releasing 470 kt CO2 each year [5]. This is a significant amount of CO_2 emissions coming from compressors that has irreversibly damaged our environment. Thus, a way forward to reduce emissions is by reducing compressor power consumption or improving its efficiency.

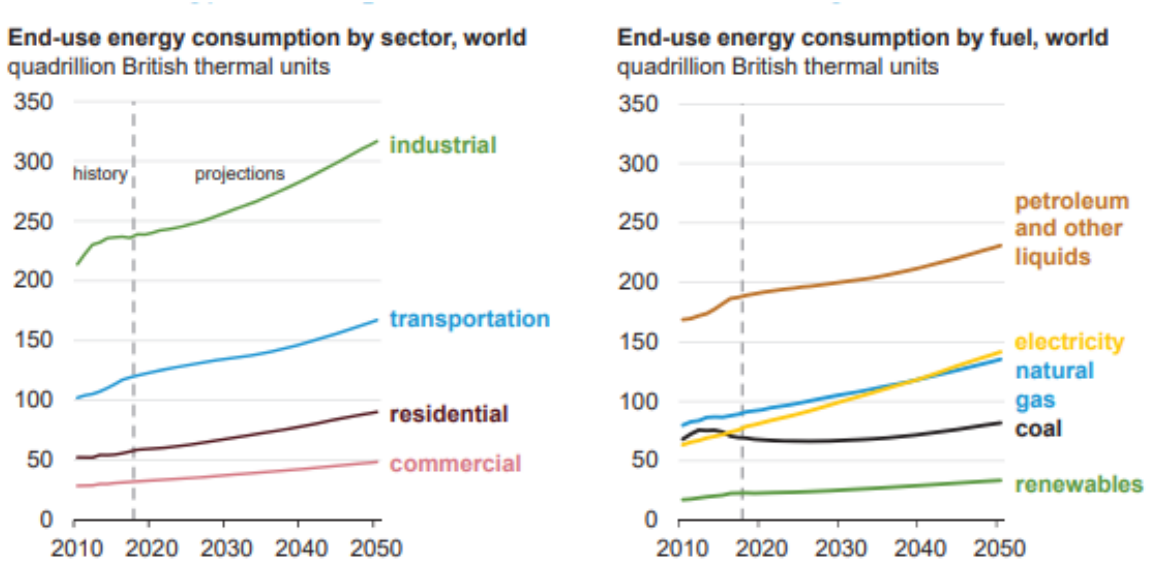

Figure 1. Worldwide growing energy consumption by sector (left) and fuel (right)[2].

These compressors can be classified according to the chart in Figure 2. Twin-screw compressors are a type of rotary positive displacement machines preferred for applications where low discharge pressure and a broad range of air mass flow rates are needed compared to reciprocating, centrifugal and axial compressors (Figure 3). Within twin-screw compressors, the most common are oil-injected compressors with an 88% share. The popularity of oil-injected machines compared to oil-free and water injected machines is because they can achieve high pressure within a single stage, operate with a smaller number of mechanical components and is of low maintenance.

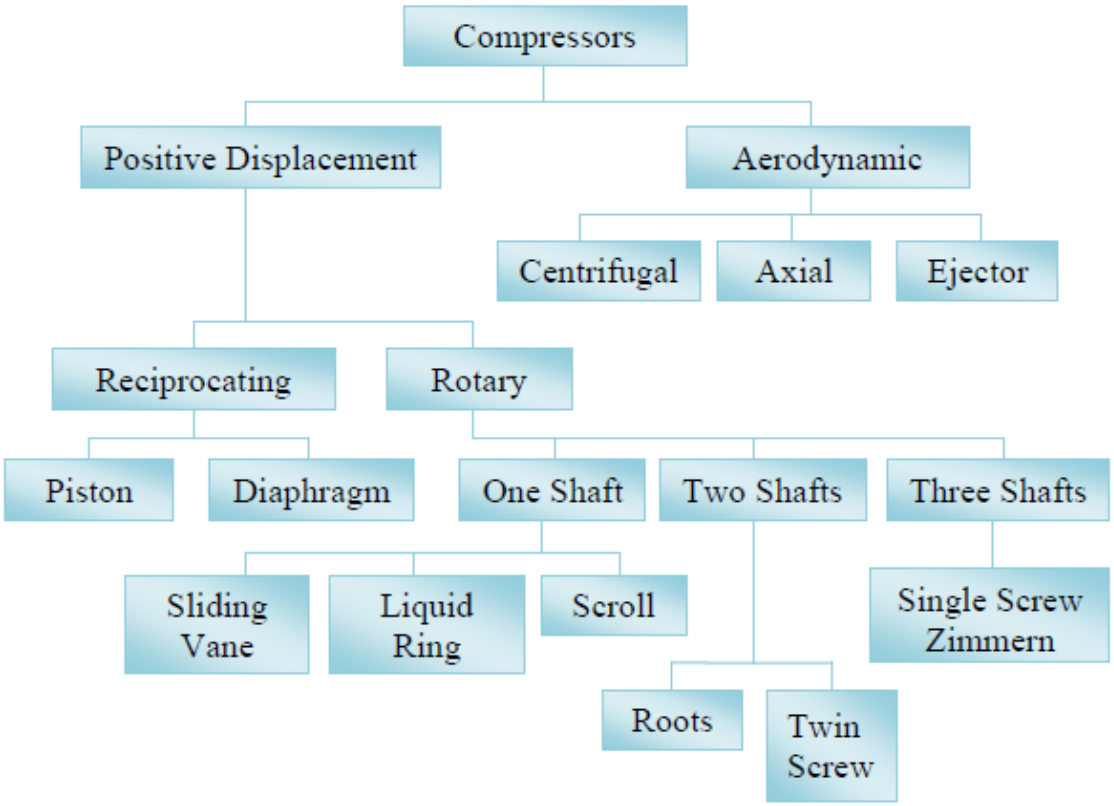

Figure 2. Classification of compressors [6].

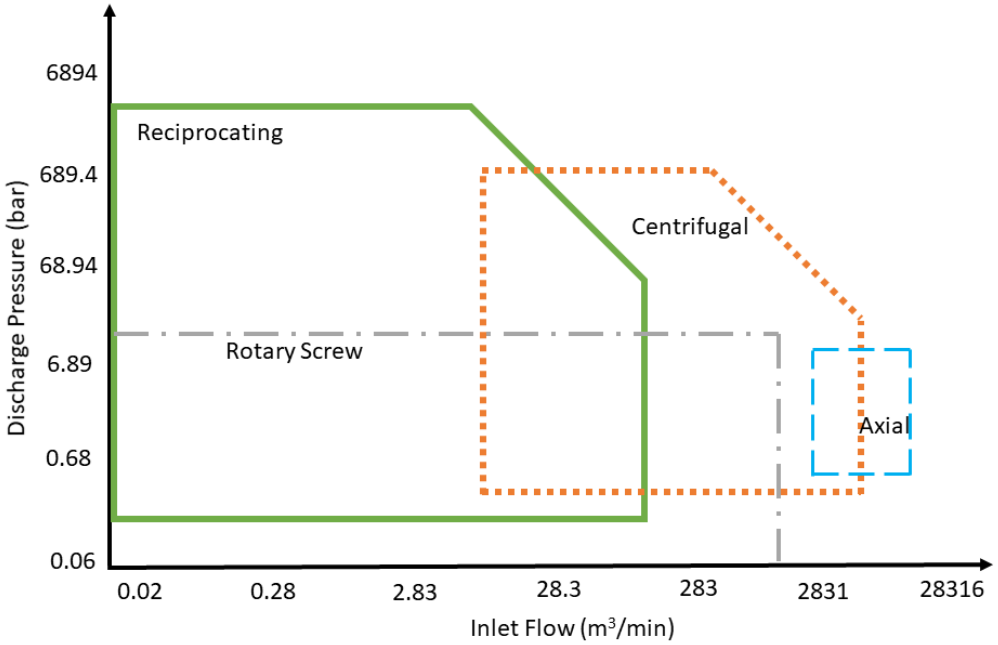

Figure 3. Application range for various types of compressors (reproduced from reference [7]).

1.2 Oil-injected screw compressor

The first oil-flooded twin-screw compressor was developed in 1954 and was made commercially available in 1957. Since then, these machines have been in operation with a thriving economic market projected to grow at a compound annual growth rate (CAGR) of 5.4% from 2020-2027 to reach a market size of $13.6 Billion by 2027[8]. The principle over which this machine functions is simple and was published in foreign languages during the early years of 1960 [9], followed by publications in English in the early 1990s [10][11].

Single-cycle operation is shown in Figure 4, with numbers indicating the state at which the gas exists. Here, the male rotor engages with the female rotor and the enclosed casing to form a closed interlobe region containing fluid. With the rotation of helical rotors, the enclosed fluid is gradually compressed, starting from the suction side until it reaches the discharge port. This gradual change in volume results in a pressure increase.

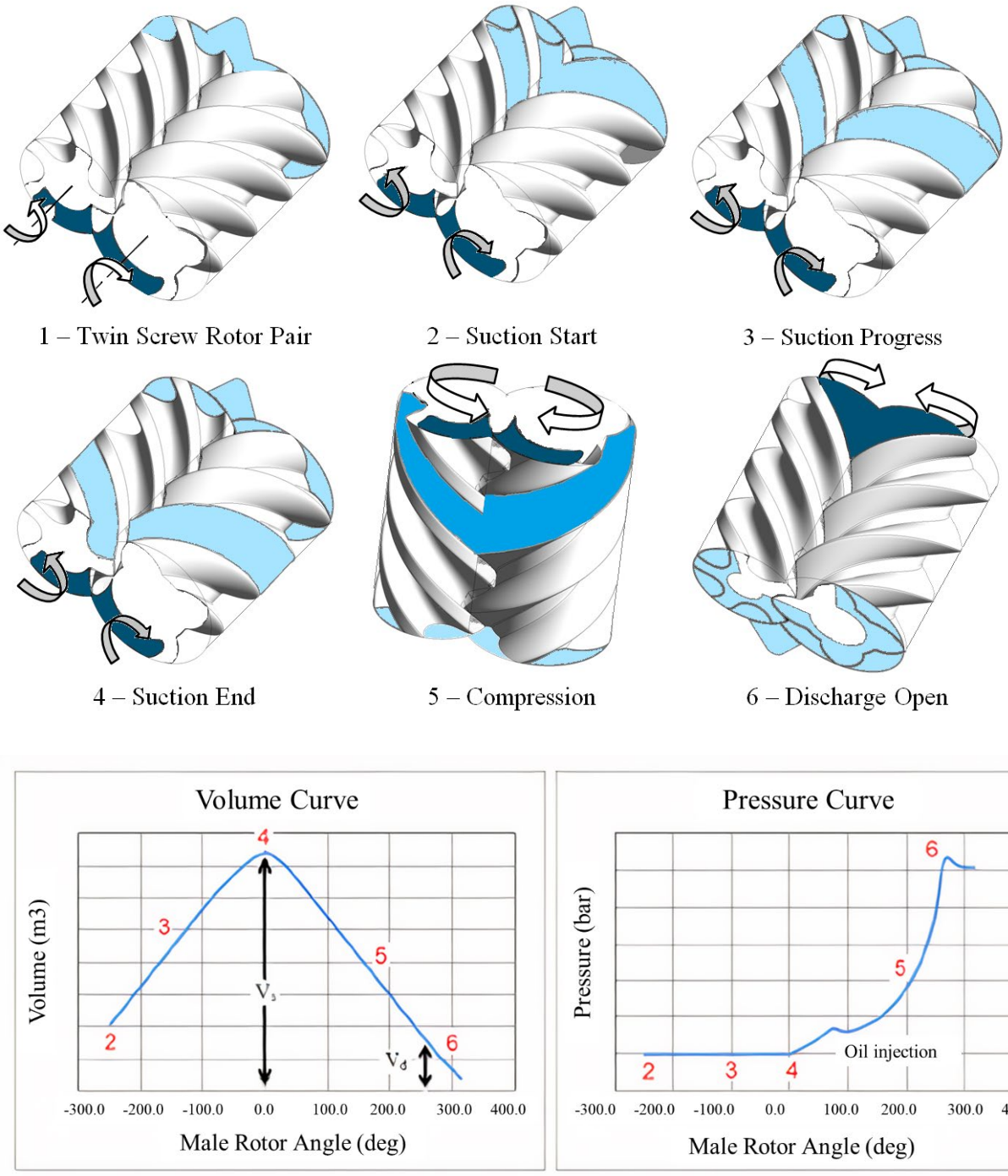

Figure 4. Operating stages in twin-screw compressor [6].

An increase of pressure in the compression chamber results in a temperature rise. For instance, an oil-free twin-screw compressor with working fluid as air and operating at a speed of 6000 rpm and pressure ratio of 6 will result in an average discharge temperature higher than 320°C [12]. Oil injection can substantially reduce this temperature. Thus, the oil serves an important purpose of cooling the compression chamber. Secondly, the oil seals leakage gaps improving volumetric efficiency and lastly, oil lubricates the rotors and the bearings. The rule of thumb in the screw compressor industry is that oil contribution by mass to cooling, sealing and lubrication is in the proportion of 100:10:1, respectively. Although injecting oil has many advantages, too large or too low oil injection quantities can result in additional power losses.

Figure 5 shows the oil injection parameters and their expected effects in the form of oil mass flow rate, oil droplet size in the compression chamber, oil injection port position and oil injection temperature. These parameters are coloured according to their intensity of affecting compressor performance. A black coloured box with a high oil flow rate shows the highest influence compared to the light grey coloured box with the injection temperature showing the least influence on compressor performance [13]. Hence, the oil flow rate can affect compressor efficiency more than the oil injection temperature.

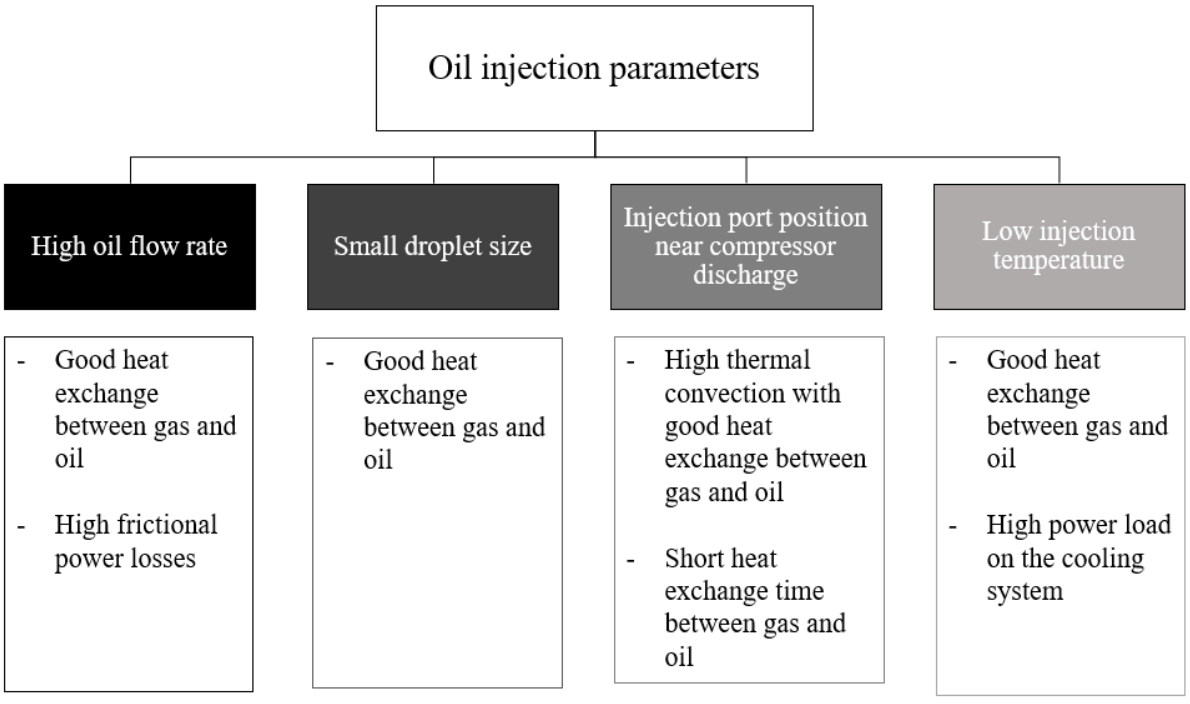

Figure 5. Various oil-injection parameters with their expected effects.

These effects can be further explained as,

i. High oil injection flow rate - in a thermodynamic system, heat exchange between gas-oil depends on the mass flow rate of the oil injected. Increased oil mass flow rate can reduce discharge temperature and increase the compressor's volumetric efficiency and adiabatic efficiency. However, excess oil can lead to power losses during injection and transport through compression chambers as its density is several magnitudes than the gas.
ii. Small oil droplet size - small oil droplet sizes have a high surface area for exchanging heat with the hot gas, which can cool the temperature in the compression chamber.
iii. Oil injection position - if the oil injection port is positioned so that the oil injection temperature is close to the gas temperature, there will be low convection between gas and oil. If the oil injection port is positioned close to the discharge port, then the residence time for oil will be low, and heat transfer between air and oil will not largely benefit the compression chamber. Therefore, optimal positioning of oil injection will help in controlling the compression chamber temperature.
iv. Oil temperature - low oil injection temperature is preferred for better heat exchange but cannot be achieved without the high load on the cooling system.

Overall, it is important to understand how the above parameters will affect the temperature in the compression chamber, which will impact compressor performance. The temperature in the compression chamber is directly dependent upon the interaction between gas and oil. Therefore, the spatial distribution of oil in the compression chamber needs to be explored for improving compressor performance.

1.3 Motivation

The motivation for this research is,

- Exploring oil distribution in a chamber will provide information on the temperature distribution in the compression chamber. This information can be related to the key oil injection parameters, such as oil flow rate, and then the key parameters can be modified to achieve near isothermal compression. The actively used lumped parameters models [14][15][16][17] are insensitive to reflect on the performance change when the oil-injection port position or the number of ports are varied while maintaining the same oil injection mass flow rate. They do not provide three-dimensional spatial information of the oil or temperature distribution.
- Exploring oil distribution which includes the transition of oil from continuous phase to droplets, will give information on the interphase area available for heat exchange or representative droplet size such as Sauter mean diameter. The temperature in the compression chamber is a determinant of the compressor performance.
- Lastly, three-dimensional computational studies on oil distribution in simple bearing chambers, gears and rotary compressors have shown that by improving cooling, the input power can be reduced [18][19][20][21]. However, such computational studies on screw compressors showing oil distribution are only a few due to their more complex rotor geometry and high pressure operating conditions.

Therefore, exploring oil distribution will broaden the knowledge of oil behaviour and effects within the compression chamber that can help make design-based improvements for better efficiency and reliability (inadequate oil distribution has led to operational seizures [22]). Accordingly, this study is carried out to estimate both oil and temperature distribution within a screw compressor compression chamber and its effect on performance.

Chapter 2 Literature Review

This chapter will evaluate different investigation approaches of oil-injected screw compressors, such as mathematical modelling using lower-order and higher-order methods and experimental techniques. In the analysis of higher-order methods, special attention will be given to computation and grid generation methods applied to these machines. An additional part of the literature review is understanding the form of oil distribution. The second phase (i.e oil) can be distributed in the form of continuous phase or droplets depending on the forces acting in the chamber. Computational methods will be explored that could capture the form of oil distribution and droplet sizes adequately.

2.1 Screw compressor

2.1.1 Mathematical modelling

Since the 1980s, studies with lumped parameter models that explored oil-injected twin-screw compressor performance were published in international conferences [12][14][16][22][23]. These were based on the classical approach of solving the equations of conservation of mass and energy applied to a control volume. Here the compression chamber was considered the working chamber, and the suction and discharge ports were an open thermodynamic system. The energy balance depended on the diameter of an oil droplet, mass flow of oil, differential temperature between air and oil and specific heat capacity of oil. More information on lumped parameter models or thermodynamic chamber model can be found in Appendix 1.1.

Using the above model, Stosic et al. [15] [16] considered various parameters such as oil inlet temperature, oil to gas mass ratio, the position of oil port and oil viscosity which were varied to evaluate for specific power—out of all the evaluated parameters, increasing oil to the gas mass ratio from 0 to 8 improved specific power by 38%.

Another parameter that needs to be considered is the oil droplet size. Singh and Bowman [23] estimated that changing from conventional injection to high pressure injection at ~15 bar results in a droplet size of 100μm. The resulting droplet size is empirically determined than measured. Nevertheless, the small droplet size in the analytical model reduced discharge temperature by 11°C and improved specific power by 9%. Similarly, studies based on the random wavelet

finite element method showed that reducing oil droplet size to 250µm has reduced discharge temperature by 10°C [25] (more information on random finite element method can be found in Appendix 1.2)

By increasing oil mass flow rate and reducing oil droplet size, performance gains can be achieved on one side; on the other side, there could be compressor power or system losses. 97% of losses occur in clearances, where oil shears through clearance, surges in front of clearance and loses momentum when accelerated through clearance [26] (Figure 6). The excess mass flow of oil rate could contribute to momentum and hydraulic frictional losses over cooling the compression chamber. The cooling effect and the losses are also affected by compressor operating conditions, rotational speed, and pressure ratio [27]. At higher rotational speeds, momentum imparted to oil could help in breaking down into small oil droplet sizes, which can promote cooling. However, higher oil velocities, when accelerated through the rotor tips and clearances, can increase momentum and hydraulic frictional losses. Similarly, a higher pressure ratio can lead to increased leakages and hydraulic frictional losses.

It can be implied from the above paragraphs that the oil mass flow can contribute to performance gains or losses depending on the spatial distribution of oil in a three-dimensional compression chamber. It is challenging for the lumped parameters to capture the compression chamber as a three-dimensional domain with geometric properties, along with a change in volume and air-oil interaction with time.

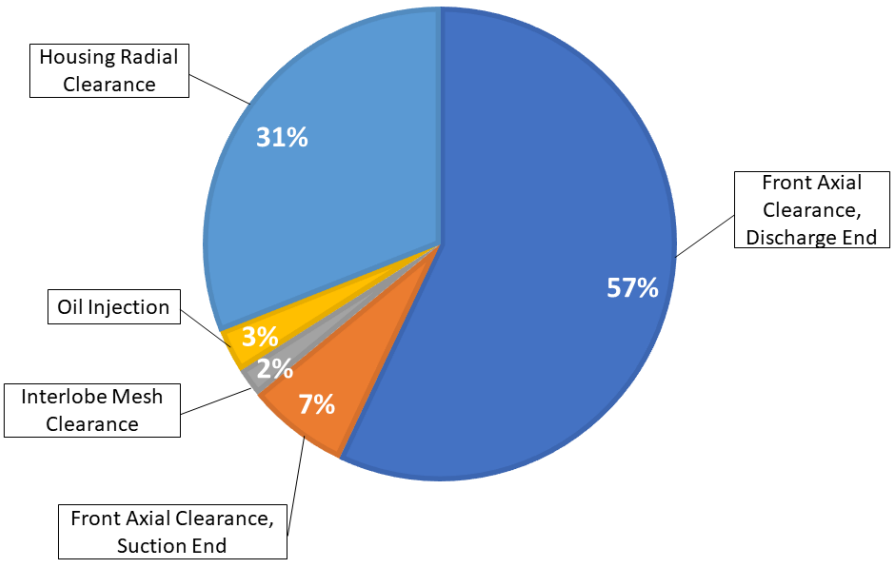

Figure 6. Distribution of power losses caused by the oil in the working chamber (reproduced from the reference [26]).

Also, in Figure 6, only 3% of losses are obtained with a conventional oil injection system when oil accelerates and loses momentum near the injection point. However, if external pumps are used to achieve small droplet sizes, then the loss at the injection point will be much higher in addition to the power consumed by the pump that will add to significant system power losses. Additional system power losses could very well overwhelm the performance gains achieved by small droplet sizes. Therefore any high pressure oil injection system should be used with very careful consideration.

2.1.2 Experimental evaluation

Experimental investigations were conducted by varying oil mass flow rate from 0.13 kg/s to 0.79 kg/s (mass ration of oil to air: 1.3 to 7.9) in a single screw compressor [28] and 0.42kg/s to 1.37 kg/s (mass ration of oil to air: 1.5 to 5.0) in a twin-screw compressor [29]. Oil mass flow beyond 0.52 kg/s in a single screw compressor and 0.79 kg/s in the twin-screw compressor had little or no effect in improving volumetric or adiabatic efficiency. The reasons provided were that the excess oil beyond an optimal point does not contribute to cooling or sealing in the compression chamber.

Other experiments used special nozzles such as flat fan, full cone and hollow cone nozzle to assess twin-screw compressor performance improvements. It was expected that these nozzles would increase oil-gas interaction surface area that will enhance cooling. However, negligible or very minor improvement in input power was reported- no improvements with flat flan, 0.05% improvement with full cone nozzle and 0.3% improvement with hollow cone nozzle is achieved compared with conventional single bore injection [30], [31]. Large improvements in input power by nearly 3% was reported with positive displacement vane compressors when a pressure swirl nozzle is used [32]–[34]. A pressure-swirl nozzle is an atomiser that generates liquid droplets imparting a swirl motion to the fluid before entering an orifice. The centrifugal forces break the liquid as soon as it leaves the nozzle. Nevertheless, similar advantages in performance using pressure swirl nozzles cannot be expected in a twin-screw compressor as the uninterrupted axial length from the point of injection to the end of the machine is much longer in vane machines than in screw machines. Long axial length is important for a pressure swirl atomiser to achieve a small droplet size, 122 μm with an injection diameter of 1.2 mm and a pressure of 9 bar in vane machines (Figure 7).

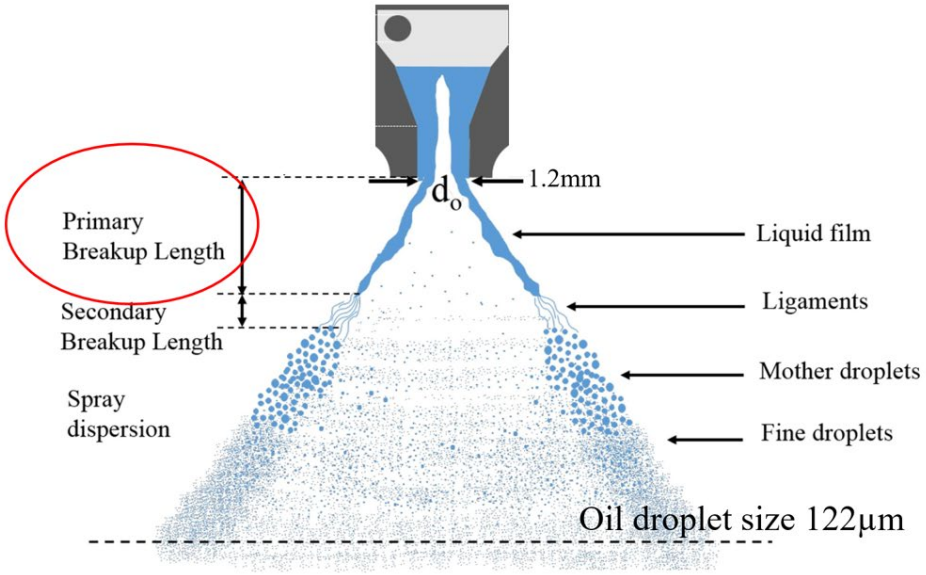

Figure 7. Oil injection with pressure swirl atomiser [35].

All the above-explained studies looked into the end result of varying mass flow rate or using special nozzles. A thorough investigation of oil distribution and behaviour in a compression chamber affecting compressor performance could not be easily found in literature as there is no optical axis in these machines. Nor there are any measurements of oil Sauter mean diameters sizes in the compression chamber. The only measurement for oil droplet size is achieved at the discharge of the screw compressor, which is shown along with other types in Figure 8.

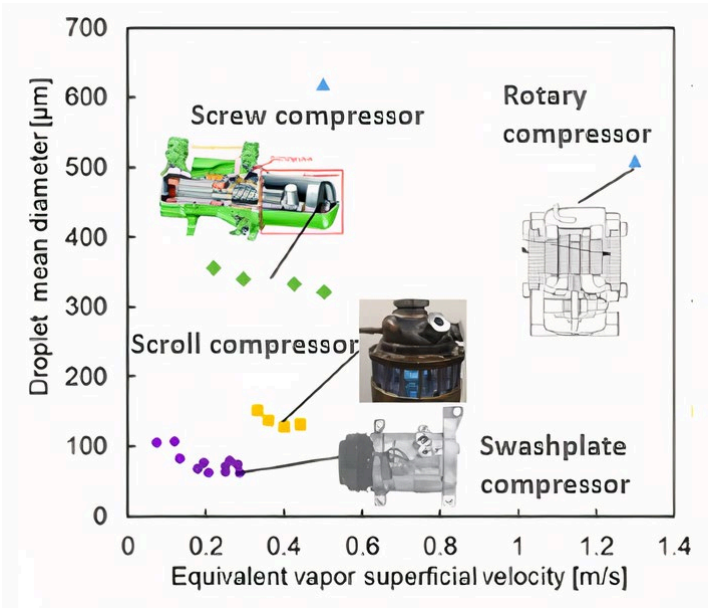

Figure 8. Oil droplet volume-mean diameter size for various compressors [36].

Again, the difficulty of optically accessing the screw compressor working domain makes it very challenging for imaging or quantification of oil distribution in these high pressure and temperature compression chambers. Thus, three-dimensional computational fluid dynamics (CFD) will be explored for this purpose.

2.1.3 CFD analysis

It is necessary to introduce higher fidelity modelling techniques to understand the spatial distribution of oil and its influence on the gas temperature in screw machines. Computational Fluid Dynamics (CFD) may be a suitable candidate to understand flow characteristics in deforming domains of screw machines.

Screw compressor rotors have a complex geometrical shape, and due to rotation, the domains are deforming with time. Developing grid generation methods to account for these deforming domains using the numerical Finite Volume Method (FVM) is a challenging task.

Eiseman et al. [37] classified the grid systems used by numerical methods such as structured, unstructured or mixed, depending on how grid points are connected, as shown in Figure 9 [38]. Structured grid systems can be further classified as single or composite grids. A single grid is based on the single boundary fitted coordinate system, an untraditional type in this category is the cartesian cut cell method [39]. A composite grid consists of two or more single grids assembled; this assembly can be completely discontinuous (overlapping mesh), partially discontinuous (non-conformal mesh) and completely continuous (conformal mesh), as shown in Figure 10 [38] [40].

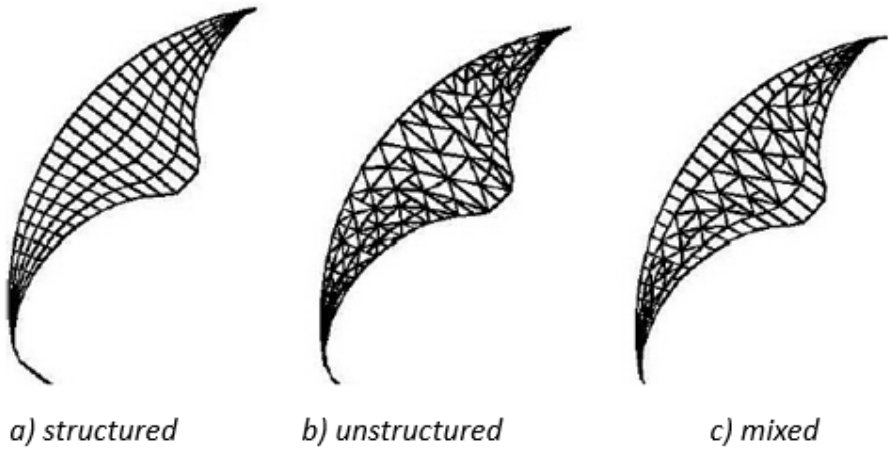

Figure 9. Types of grid system [38].

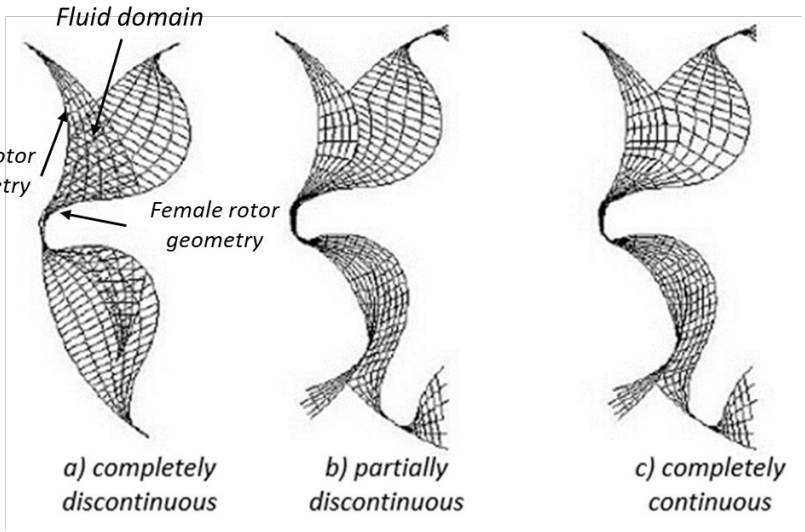

Figure 10. Types of composite structured grids [38].

Common methods to generate boundary-fitted or boundary confirming grids are algebraic methods, differential methods and hybrid methods. More information on these methods can be found in the book by Lisekin [41]. These methods have been applied for the successful generation of grids in twin-screw machines.

Kovacevic [42] described the first version of numerical grid generation software SCORG^{TM} (Screw Compressor Rotor Grid Generation) to generate a high-quality numerical grid for a screw compressor. This was a breakthrough as prior to this, there were no techniques available to generate robust grids for twin-screw machines. These original grids were of the rotor to casing type generated using an algebraic grid generation method which introduced a non-conformal interface between the male and female rotor domain. Vande Voorde [43] used a differential approach to generate grids for screw compressors. Based on the feature of the rotor to casing type grid generated from Kovacevic [38][44] and the hybrid differential method form similar to Vande Voorde, Rane et al. [45] proposed new developments. These developments led to a conformal interface between the two rotor domain; grid quality was further improved for this type by smoothening the partition between the two rotors [46].

Apart from the customised grid generation techniques mentioned in the above paragraph, grids can also be deformed with other methods in commercial solvers. These are spring smoothing, hexahedral layering, tetrahedral remeshing, and key-frame remeshing [47][48]. In the sping-based smoothing method, the edges between the two mesh nodes are idealised as a network of interconnected springs, where a displacement at a given boundary node will generate a force proportional to the displacement along all the springs connected to the node. In hexahedral

layering, layers of cells can be added or removed adjacent to the boundary, based on the height of the moving surface. In some cases, with large boundary displacement where spring-based smoothing is applied, the cell quality can deteriorate, invalidating the mesh. Here, the mesh can be locally updated with new tetrahedral cells called tetrahedral remeshing. Along with this, interpolation is done from previous time steps as all cells will have changed connectivity known as key-frame remeshing.

Nevertheless, the magnitude of boundary deformation with these techniques is low and cannot exceed 50% of cell size per step [49]. For instance, key-frame remeshing was applied for the screw compressor, but it failed due to the complex geometry [50]. Thus, customised grid generation techniques are more suitable for resolving flow in twin-screw machines.

Also, one of the alternative approaches to remeshing/deforming grids is immersed boundary method [51]. This method has been applied for the simulation of gear pumps where the presence of a moving gear body is represented using a forcing term in the momentum equation [52]. The forcing or the source term forces the flow to follow the boundaries of the immersed body. Though this method is good for capturing rotational velocities in the computational domain, the capability of capturing increasing pressure with the change in computational domain volume still needs to be practically explored. Hence, the discussion in this thesis is inclined towards the customised grid generation techniques.

Since the 1980s, various commercial CFD solver packages have emerged [53], and many of them like Ansys CFX, Ansys Fluent, Star CCM+ can be used with customised grids [54]. Kovacevic [44] used the COMET solver package for the rotor to casing type grids in an oil-free, oil-injected and refrigeration compressor. Further to this, both rotor to casing and casing to rotor mesh was used with Ansys CFX for oil-free twin-screw compressor analysis. Conformal mesh or casing to rotor mesh showed improved accuracy in performance predictions [55][56]. Also, rotor to casing mesh was used with PUMPLINX [57], the overlapping mesh was used with StarCCM+ [58], and Cartesian cut-cell mesh was used with CONVERGE CFD software package [59] for an oil-free compressor analysis.

Analysis for oil-injected compressor has been successfully conducted with Ansys CFX using the Eulerian-Eulerian approach, and predictions of airflow and power are close to experimental measurements. This study also provided good visualisation of oil distribution and local gas temperatures in the compression chamber [12]. Similarly, an oil-injected compressor with casing to rotor mesh was analysed using the VOF model in Pumplinx [60]. An oil-injected

expander with grids generated through differential methods was analysed using the Eulerian-Eulerian model in Ansys Fluent [61]. More details on multiphase flow models with CFD can be found in Appendix 2. Nevertheless, it can be implied from these studies that either Ansys CFX, Ansys Fluent or PUMPLINX can be used for analysing oil distribution in twin-screw machines.

Ansys CFX was explored for modelling oil-injected compressor with both the Eulerian-Eulerian and VOF model. Only the Eulerian-Eulerian model was stable and accurate [62]. This exposed the limitations with the variety of multiphase flow models in Ansys CFX compared to Ansys Fluent. Firstly, extensive choice of interface reconstruction schemes necessary for solver stability and accuracy is not available in Ansys CFX as compared to Ansys Fluent [63]. Secondly, a facility for improvising on the standard code or features by writing user-defined functions isn't available with Ansys CFX but available in Ansys Fluent. Lastly, Ansys Fluent models have been customised to successfully analyse for cooling, lubrication and hydraulic losses for rotating gears (screw rotors and meshed gear geometry is alike to some extent) [21], [64]–[67]. The achieved oil distribution in gear chambers is very close to the distribution achieved through high-speed imaging at a range of operating conditions. Thus, varied multiphase flow modelling options, along with the user-defined functions, makes Ansys Fluent a preferred CFD software package to visualise oil in this case. Ansys Fluent can only resolve for conformal mesh between the deforming male and female rotor domains, for which casing to rotor mesh is available through the SCORG^{TM} grid generation software package.

2.2 Gas-liquid Phase

The disintegration of the oil phase in the gas medium can occur when it is accelerated at the injection port or through the clearances in the compression chamber.

2.2.1 Liquid injection and breakup

Oil injection in an air compression chamber can be considered as a simple liquid jet entering a gaseous medium.

Non-dimensional numbers such as liquid Weber number, gas Weber number, Reynolds number and Ohnesorge number play an indicative role to identify the fragmentation of the injected oil. These numbers are described in equations (1)-(4). We_l is used for determining Oh. The reference to weber number or We in this thesis is the gas Weber number. d_o denotes injection orifice diameter.

$$We_l = \frac{\rho_l v_l^2 d_o}{\sigma} \quad (1)$$

$$We = \frac{\rho_g v_g^2 d_o}{\sigma} \quad (2)$$

$$Re_l = \frac{\rho_l v_l d_o}{\mu} \quad (3)$$

$$Oh = \sqrt{\frac{We_l}{Re_l}} \quad (4)$$

Based on the Ohnesorge number and Reynolds number, the type of liquid fragmentation is shown in Figure 11 [68] [69]. These are,

i. Rayleigh Regime - at low Reynolds number, jet disintegrates solely due to surface tension effects.
ii. First and second wind-induced regime - with increasing Reynolds number, inertial forces overcome the surface tension effects leading to jet integration.
iii. Atomisation Regime - at high Reynolds number and Ohnesorge number, jet disintegrates to atomise into small droplets.

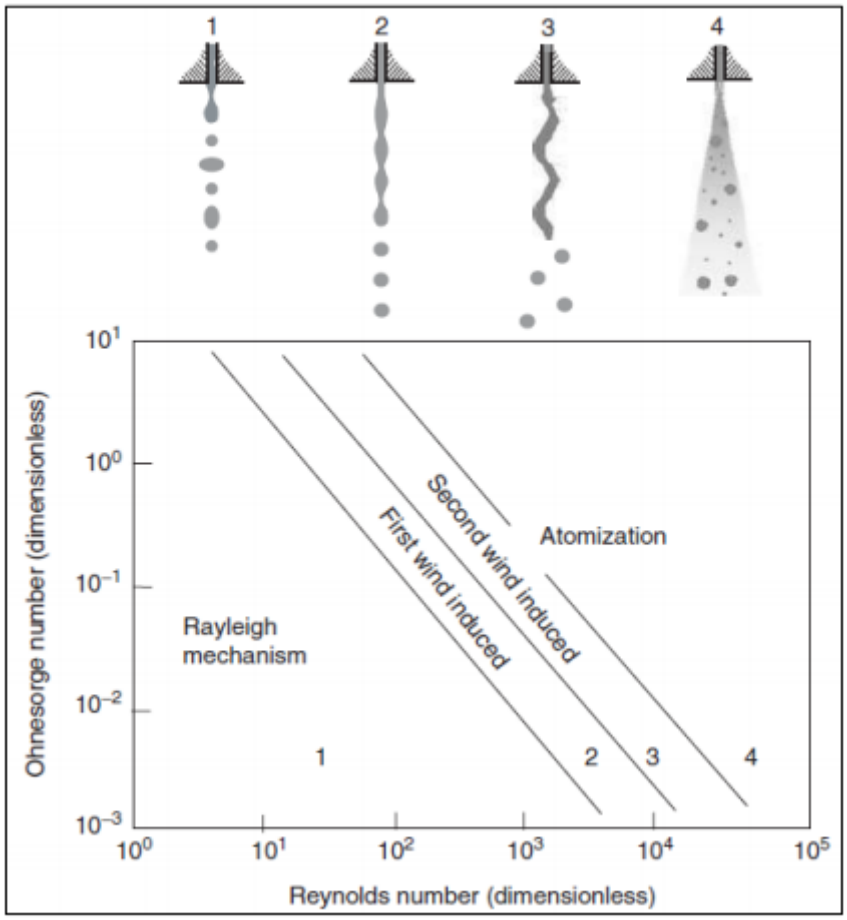

Figure 11. Liquid fragmentation types when injected through an orifice [68][69].

Injected oil in a twin-screw compressor will undergo an atomisation regime as Re_l >1000 and Oh >1.

A case of liquid water jet with increasing injection velocity and Weber number is shown in Figure 12. Water is injected through a circular orifice of 1cm. At the highest Weber number, there is high instability, and small droplets are formed. If the same liquid is injected in crossflow where gas is flowing at some velocity, then the instability will be much higher, and the droplets will be much smaller [70]. This situation is closer to oil injection in a compressed gas chamber.

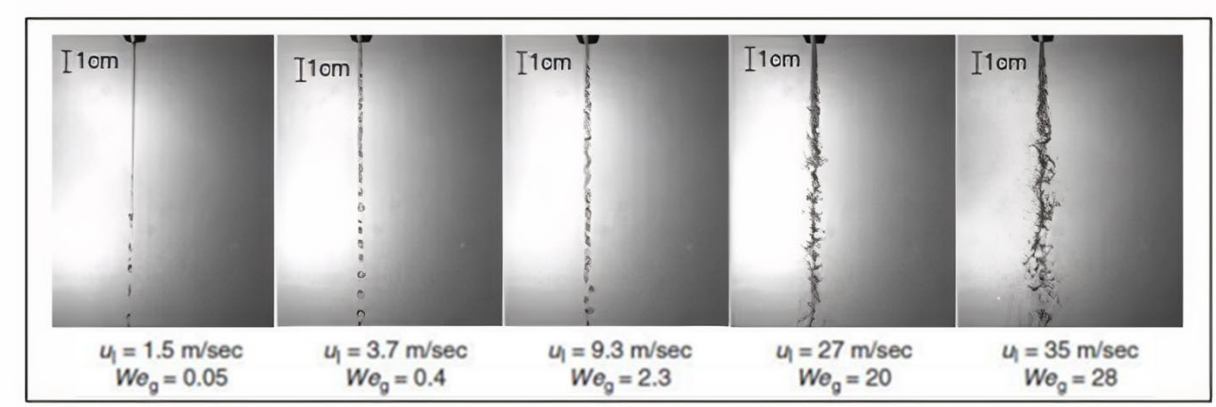

Figure 12. Jet disintegration with increasing Weber number-primary breakup [69].

The regimes mentioned above with Figure 11 are a part of a primary breakup. The liquid jet can also undergo secondary breakup to form spherical droplets. Both primary and secondary breakup occurring due to the liquid injection through an orifice is shown in Figure 13.

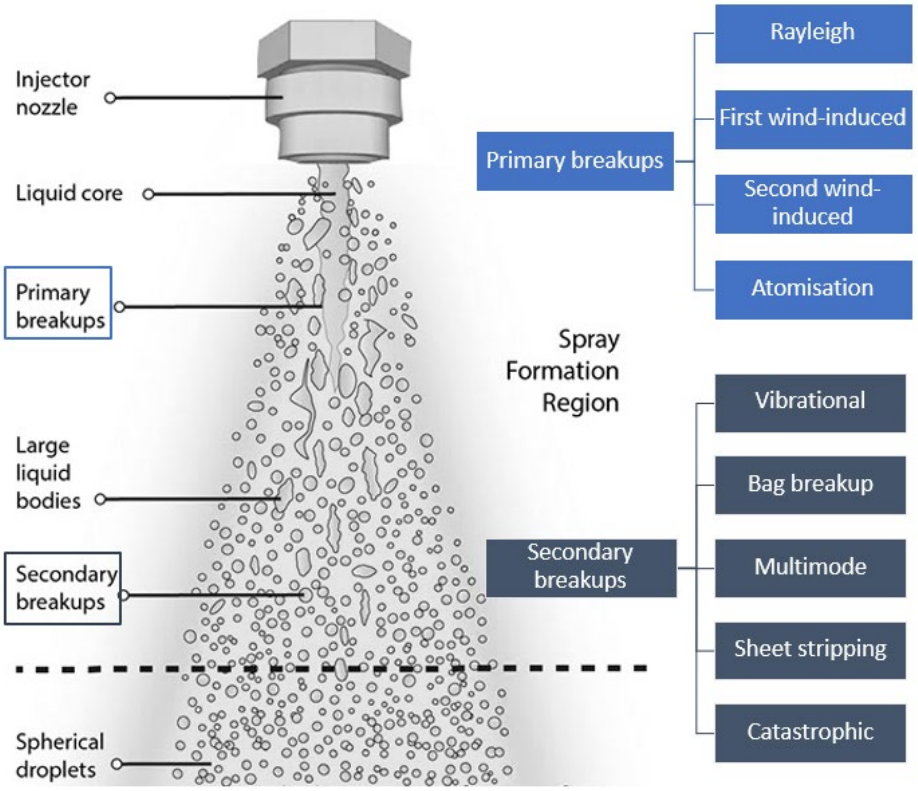

Figure 13. The primary and secondary breakup of the liquid jet [71].

Secondary droplet formation and deformation rate are driven by the density ratio between the liquid and the gas, Weber number and initial shape of the column or primary liquid breakup feature [72]. These breakup mechanisms, according to the Weber number, are shown in Figure 14. It can be noted here that flow with a very high Weber number (>350) can result in a

catastrophic secondary breakup, leading to a multitude of small-sized droplets, and the opposite is for the flow with Weber number <12.

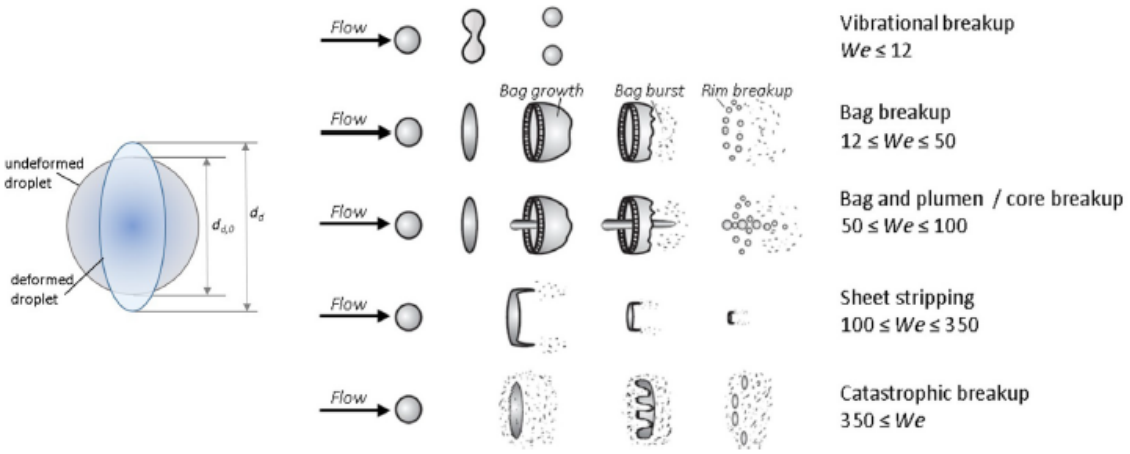

Figure 14. Schematic of secondary drop deformation and breakup mechanisms according to Weber number [73].

Furthermore, looking at the flows with varied density ratios and narrowing down Weber number below 120, a range of bag breakup mechanisms can be classified according to Figure 15. The density of oil to air in a twin-screw compressor is ~950, which can result in sheet-thinning, backward bag/lobe with sheet-thinning and forward bag with stamen depending on the Weber number.

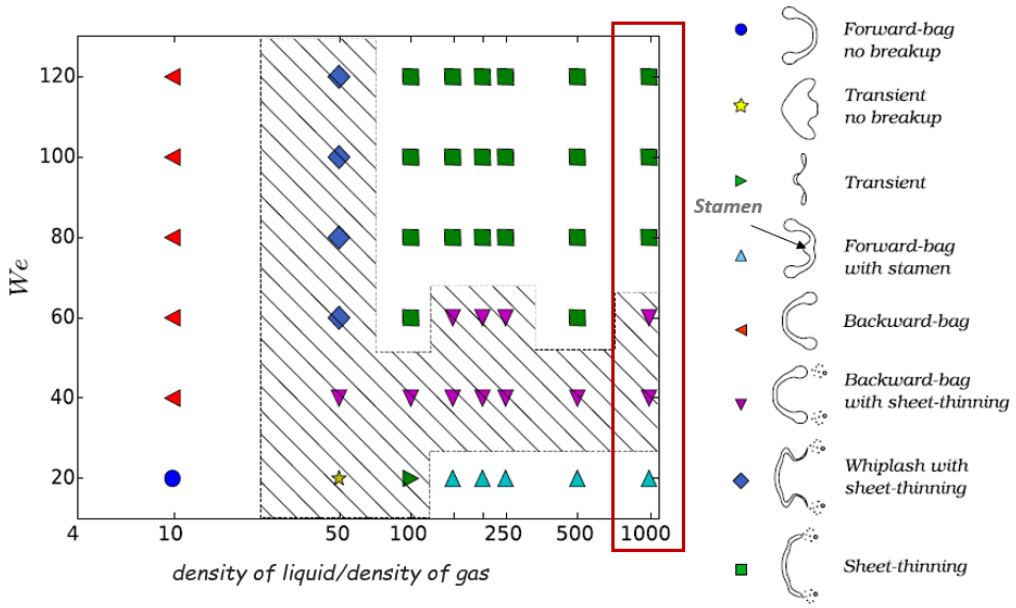

Figure 15. Breakup mechanisms depending on the liquid to gas density ratio and Weber number 4-120 [74]. The region highlighted in red represents the density ratio in an oil-injected compressor.

A combination of primary and secondary breakup based on the Weber number will determine the resulting droplet size. Thus, visualising the oil breakup process in a compression chamber will help understand the resultant droplet sizes.

2.2.2 Liquid distribution and breakup

After the oil is injected, it is distributed in the compression chamber until it leaves for the discharge port. Oil in a gas-filled compression chamber should be considered a two-phase gas-liquid system in various multiphase flow regimes.

Figure 16 shows a generic chart of the multiphase flow regime based on the volume fraction/velocity of gas on the x-axis and volume fraction/velocity of liquid on the y-axis. A bubbly flow regime can be observed when there is a high liquid volume fraction and liquid velocity compared to gas volume fraction and gas velocity. In the bubbly regime, the bubbles are present in the region at the top of the pipe. On increasing the gas velocity, the bubble size becomes larger and coalesce to give the elongated bubble or the slug regime. With still higher gas velocity, the slugs join together to form a continuous gas layer in the upper region of the pipe. This is known as the stratified-smooth flow. With higher gas velocity than the liquid velocity, the fast-flowing gas will cause instabilities at the interface resulting in a stratified-wavy flow. With further increasing liquid velocity, the wave instability increases, forming large crests. The gas breaks through these crests, resulting in the liquid being distributed over the pipe walls as thin film and at the centre of the pipe as droplets. This is known as the annular regime.

Since flow regimes are not obtained for the compression chamber, some similarities can be drawn with a pressurised gas-oil pipe. The flow regime in a pressurised gas-oil pipe can fall under stratified flow or an annular flow [75]. This is simply due to the high velocity and volume fraction of the gas phase compared to the liquid phase.

If $v_g >> v_l$, then it is a stratified flow and if $v_g > v_l$, then it is annular flow.

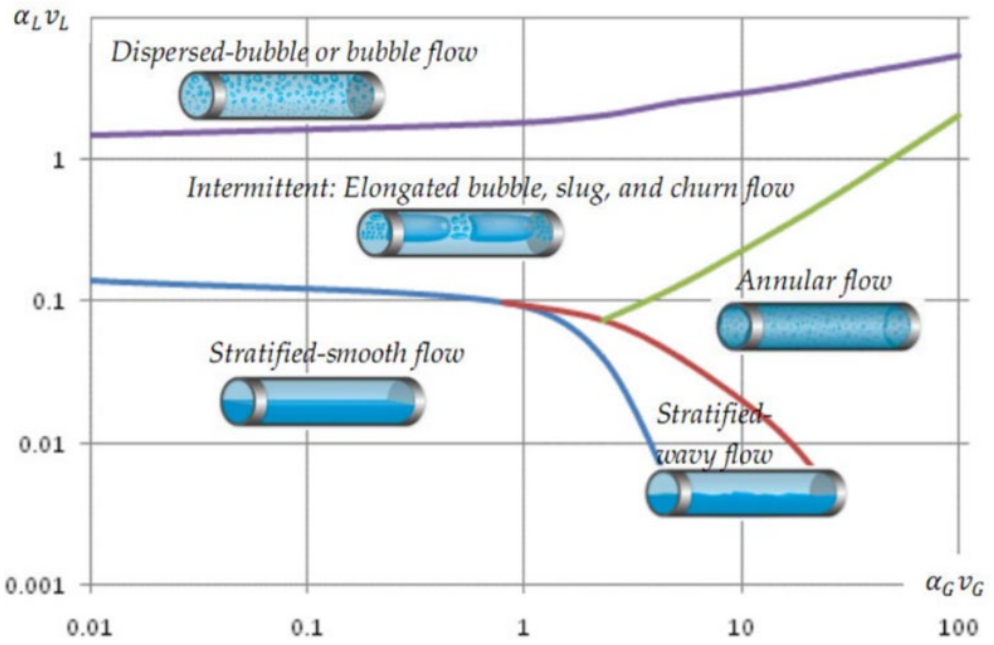

Figure 16. Two-phase flow regimes of gas and liquid in a horizontal pipe [76].

With stratified flow, the gas exerts shear stress on the liquid surface film and even drives the film [77],[78],[21]. This shear stress can lead to film separation, which can break up to create droplets [79],[80], transitioning to annular flow. However, in Figure 17, instability is observed on the liquid film, and the angle of the bent geometry will influence the film separation. During film separation, the remainder of the fluid (bulk flow) can either stay attached to the wall or fully separate from the wall depending upon the inertia acting in that region [81],[82] (Figure 17). Liquid films where $H^* > 1.06$ (H^* is the ratio of film thickness to the curvature) are more likely to separate [83].

Figure 17. Film separation from a bend [81].

A higher number of atomised droplets can be found in annular flows than stratified flow, as gas and liquid velocities are comparable [84]. This added inertia helps in quickly shedding liquid sheets, ligaments and droplets. Forming small spherical droplets is faster in the annular type of flow regime than stratified flow [85].

Therefore, the atomisation resulting in small droplet sizes can occur during oil injection and due to the forces acting on the oil phase in the compression chamber. However, in order to estimate the potential oil droplet sizes close to the injection point, semi-empirical models from the literature are explored.

2.2.3 Semi-empirical models for droplet diameter prediction

If the information on the number of liquid droplets and their diameter sizes is available in a system, then Sauter mean diameter (SMD) and Volume-mean diameter can be calculated according to equation (5) and (6).

$$Volume\ mean\ diameter = \left[\frac{\sum n_{drop} d_{drop}^3}{\sum n_{drop}}\right]^{1/3} \tag{5}$$

$$Sauter\ mean\ diameter = \left[\frac{\sum n_{drop} d_{drop}^3}{\sum n_{drop}\, d_{drop}^2}\right] \tag{6}$$

If the information on droplets is not available, and the liquid injection falls under the atomisation regime, then Sauter Mean Diameter (SMD) can be obtained through the key correlations achieved by semiempirical modelling in Table 1.

Table 1. Semi-empirical formulation of oil-injection through a plain orifice.

Literature	Correlations	Tested conditions
Harmon, 1995 [86]	$SMD = 330 d_o^{0.3} \mu_l^{0.07} \rho_l^{-0.648} \sigma^{-0.15} v_l^{-0.55} \mu_g^{0.78} \rho_g^{-0.052}$	Water d_o~ 3mm P_i= 20-80bar
Merrington and Richardson, 1947 [87]	$SMD = \frac{500 d_o^{1.2} v_l^{0.2}}{\mu_l}$	Various fluids d_o= 0.8-8mm P_i up to 25bar
Elkotb, 1982 [88]	$SMD = 3.08 v_l^{0.385} (\sigma \rho_l)^{0.737} \rho_g^{0.06} \Delta P_l^{-0.54}$	Diesel fuel d_o= 0.5-1.2mm P_i= 78-115bar

Also, researchers have conducted experiments on measuring and determining Sauter mean diameter size for oil and its injection conditions similar to that in an oil-injected compressor [31][89]. The oil injection conditions with the measured Sauter mean diameter is presented in Table 2.

Table 2. Measured Sauter mean diameter size of oil droplet for oil injection at variable injection conditions.

Literature	Mass flow rate of injected oil [kg/s]	Air (injection medium) conditions	Orifice diameter [mm]	Measured SMD [mm]
Paepe, Bogaert and Mertens [31]	0.104	Temperature= 100ºC	2.0 2.5 3.0	0.96 1.97 3.53
Lin, Fan and Jin [89]	0.158 0.205	Pressure= 4.0 bar	1.6 2.0 3.0	0.75 1.46 3.8

This allows comparing Sauter mean diameter size predictions of oil from correlations with the measured Sauter mean diameter size for the injection conditions specified in Table 2.

Figure 18 compares measured values in literature with the predictions from various semi-empirical models. This can be used to find a suitable semi-empirical model that can be used to predict Sauter mean diameter size of oil for oil injection conditions in this thesis.

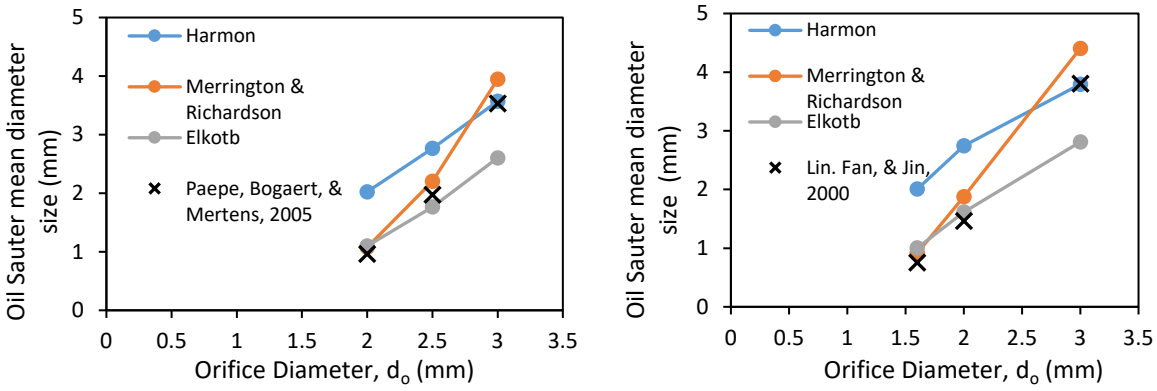

Figure 18. Comparison of Sauter mean diameter predictions from semi-empirical models with the measured data from Paepe, Bogaert and Mertens [31] and Lin, Fan and Jin [89].

From the figures, SMD predictions using Merrington and Richardson's model follow a similar trend with an offset of 7.4% when compared with the measured data in the literature for various orifice diameters. The SMD predictions from the Harmon model lie close to experimental data for large orifice diameter such as 3mm. Oil injection port diameter for the compressor studied in this thesis and the typical industrial compressor have diameters close to or, in many cases, larger than 3mm. Therefore, the Harmon model will be used for oil droplet diameter prediction for a compressor case study in this thesis as orifice diameters are bigger than 3mm (Section 6.2).

2.2.4 Computational modelling methods

This section explores various modelling methods in CFD that can be used for capturing oil phase breakup in a gas medium.

The modelling methods need to account for the abrupt changes in physical properties at the interface between gas and liquid, and this interface is known as the free-surface. Various techniques can be used to capture the interface, classified mainly into Eulerian and Lagrangian frameworks. These frameworks describe the observer's reference frame. In the Eulerian approach, the reference observes the fluid that flows through a control volume fixed in space,

and the direction of flow inside the control volume can change frequently. Like in Figure 19a, the control volume located at position $s_{0,}$ which is identical to s_1 etc.

For the Lagrangian formulations, the local reference frame moves with the fluid flow [90]. In this reference frame, the position of the observer constantly changes. At the beginning of time, the control volume is at position s_0, at which the flow velocity is v_0. With time the control volume travels to s_1 and s_2, as shown in Figure 19b. Here, the connection between position vectors allows for the reconstruction of particle trajectory. Resolving the two-phase flows can be done using two frameworks alone or in combination.

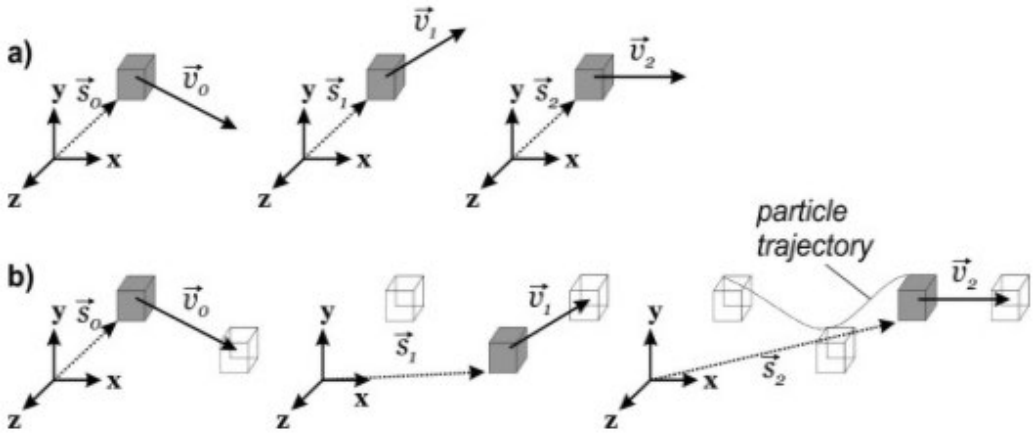

Figure 19. (a) Eulerian frame of reference: fixed in space and (b) Lagrangian frames of reference: moving in space [91].

The disintegration of the liquid jet with the forces acting on it is very complex to model. Close to injection, the dense volume fraction of liquid is found, but the droplet cloud disperses far from the nozzle. For the dense volume fraction of liquid, Eulerian-Eulerian approaches are suitable. The discrete model or Euler-Lagrangian approach is more suitable to track the dispersed droplets. To capture the breakup scales between these two, Adaptive Mesh Refinement (AMR) with Eulerian-Eulerian modelling can be adopted [92], [93]. The applicability of different approaches is shown in Figure 20.

The Eulerian-Lagrange technique has been used for modelling free-surface flows [94], mainly considering studies related to the rise of gas-liquid bubble columns [95][96]. The inert/massless particles are placed inside cells with the fluid present, the local velocities move the particles, and by some linear interpolation, the coordinates are determined.

The details and governing equations for various multiphase flow models is explained in Appendix 3.

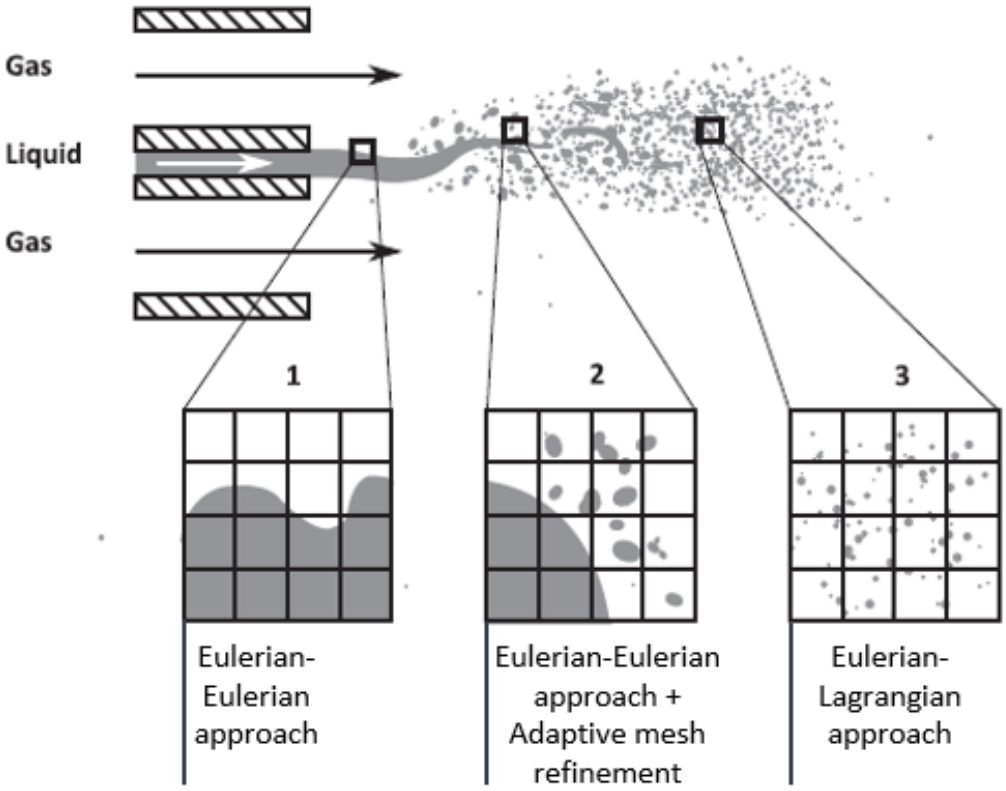

Figure 20. The multi-scale aspect of a liquid breakup [93].

Initial studies carried out regarding fuel injection atomisation would track fuel droplets in a two-dimensional medium; these studies did not reflect the 3D structure and development of real-life sprays [97][98]. A 2D modelling was done to save a huge amount of computational power needed for a large number of droplets. As a balance, ELSA (Euler-Lagrange Spray Atomization) model was developed [99]. However, for this model, some form of information is required on initial conditions of the particles- initial particle distributions, positions and velocities etc. This information had to be determined experimentally or by other means before carrying out modelling. Therefore, techniques based on the Euler-Lagrangian approach are not attractive for screw compressor case as no information is available on initial droplet distributions.

Next is the Eulerian-Eulerian approach, where both phases are treated as a continuum. This solution is attractive to describe the evolution of spray characteristics, whilst keeping the computational cost reasonable. The Volume of Fluid (VOF) is a suitable approach to capture the gas-liquid interface [100]. Still, a simple VOF model with no dynamic refinement during calculation cannot capture the small deformation structures [101]. Adaptive mesh refinement is primarily used to refine the cells to better capture the rapidly deforming interfaces and reduce

the computational burden [92]. Complex flows such as ligament formation and breakups have been predicted with this approach (shown in Figure 21) and validated with the experimental data [102].

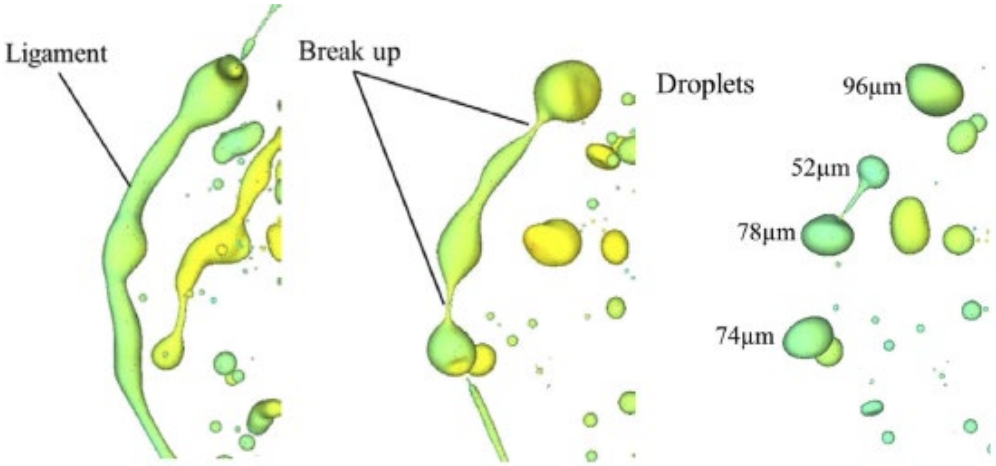

Figure 21. The development of ligament from the liquid and its result into droplets with increasing time [102].

In addition to VOF modelling with adaptive mesh refinement, some approaches should be applied to estimate the size of oil droplets in the computational domain. These approaches rely on the assumption that small, detached interfacial structures are spherical due to the dominant influence of surface tension [103]. Specifically, during calculations, checks are carried in Ansys Fluent to identify the detached interfacial structures known as lumps [104].

The checks carried out to identify lumps in the computational domain are,

a) Diameter range of the lumps
b) Asphericity below threshold
c) Minimum liquid volume fraction above 0.9
d) Liquid of volume fraction 0.9 surrounded by liquid volume fraction zero (i.e, it is an isolated lump)

To calculate asphericity, every facet of the lump surface (gas-liquid interface) and a vector from the lump's centre of gravity to the centre of the lump boundary facet is computed. These vectors are shown in Figure 22. This vector is then normalised and then used in dot product with the facet unit normal. The dot product is calculated to obtain a measure of relative orthogonality in the range 0-1. Then the values for the faces are area-averaged and then subtracted from 1 to obtain the asphericity value. For instance, if the asphericity is close to zero, the code will allow only the perfect spheres to be considered as droplets/lumps [104].

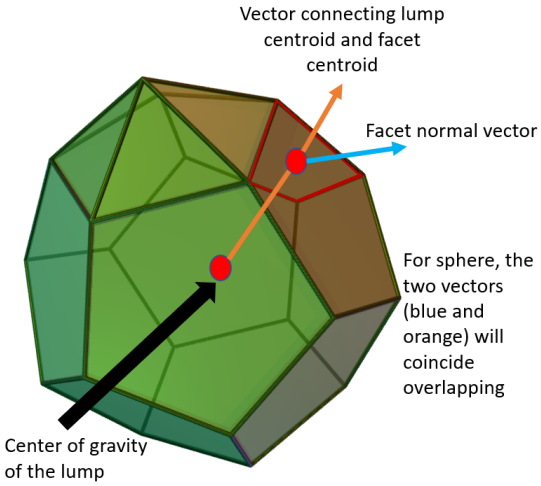

Figure 22. Representation of asphericity criteria in Ansys Fluent.

These approaches have been successfully applied for the case of liquid injection in crossflow [105], round jet with the annular flow of liquid and gas [106] or liquid sheet atomisation [93]. Droplet sizes and distribution from these studies have reasonably agreed well with the experimental data.

The VOF model with adaptive mesh refinement approach has also been applied to complicated case studies such as fuel injection in diesel engine [107], oil injection in intermeshed rotating gears [64] (Figure 23) and oil distribution in rotating bearing chambers [21]. These studies have captured the transition of the oil phase to droplets that represents a realistic situation. Thus, the VOF model with adaptive mesh refinement can be applied to visualise the form of oil distribution resulting in droplets within the twin-screw compression chamber.

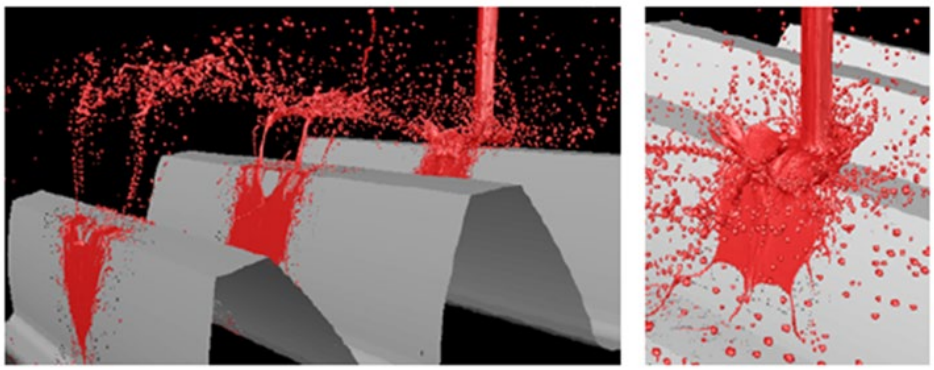

Figure 23. The transition of continuous oil phase to droplets showing the splashing oil with gears [64].

2.3 Summary

Key conclusions from the literature study are,

- Analytical modelling of screw compressors has shown that the oil mass flow rate and oil droplet size will have a good effect on integral screw compressor performance. However, the balance between cooling benefits and frictional losses will depend on the spatial distribution of oil in the compression chamber.
- Experiments using conventional single port injection with increasing oil mass flow rate have shown that no further increase in efficiency is noticed beyond optimal oil mass flow. Hence, it is important to investigate the reasons for this with an understanding of oil distribution in the compression chamber and its effect on compressor performance.
- The analytical models cannot represent the geometrical three-dimensional compression domain, and experiments could not have an optical axis for visualisation of oil distribution. Therefore, CFD is an apt methodology to study oil distribution in a compression chamber.
- Commercial CFD software packages such as Ansys CFX, Ansys Fluent and PUMPLIX have been used to study oil-injected twin screw compressors. Limitations with Ansys CFX and PUMPLIX are observed on available multiphase modelling techniques and customisation of standard codes compared to Ansys Fluent. Therefore, the Ansys Fluent software package will be used in this thesis, and customised grids are available through SCORG.
- The injected oil phase in the compressor can undergo primary and secondary level breakup to form droplets. Also, the oil film on the casing walls can break up to form droplets.
- Sauter mean diameter of oil from the oil injection port in a twin-screw compressor can be estimated through Harmon's semi-empirical model.
- Special treatment like adaptive mesh refinement must be performed to capture the oil breakup mechanisms leading to atomisation and oil droplet size estimation.

In summary, the oil distribution related to oil mass flow and compressor performance will be studied using Ansys Fluent. In addition to this, the computational study will be extended through adaptive mesh refinement to account for the oil phase breakup and atomisation. This research will broaden the understanding of oil distribution's effect and form in a screw compressor.

Chapter 3 Objectives and Contribution to Knowledge

3.1 Objectives

The aim of the thesis is to explore the state-of-the-art oil-injection techniques and improve the performance of an oil-injected compressor by numerical modelling. The research is carried out on the oil-injected screw compressors designed in the project with industrial sponsor Kirloskar Pneumatic Company in order to achieve a competitive edge in compressor efficiency and reduced energy consumption.

The main objectives are:

- Develop user-defined functions which will enable performing three-dimensional computational modelling in screw compressors using commercial software Ansys Fluent based on the structured body fitted numerical meshes produced by in-house software SCORG. (Chapter 4)
- Evaluate the accuracy of two-phase computational models for performance prediction and analysis of oil-injected screw compressors. (Chapter 5)
- Modify the existing oil-injection system in order to improve the performance of the oil-injected screw compressor. (Chapter 6)
- Explore the formation of the oil film and its disintegration in a compression chamber, and estimate oil droplet sizes within the screw compressor chamber (Chapter 7)

3.2 Methodology

Figure 24 shows the research approach adopted to achieve the research objectives in this thesis. The main challenge was in developing a method to visualise oil distribution for an industrial oil-injected compressor. Hence, the focus is on implementing the computational technique and using it to demonstrate oil distribution with a variety of oil injection conditions.

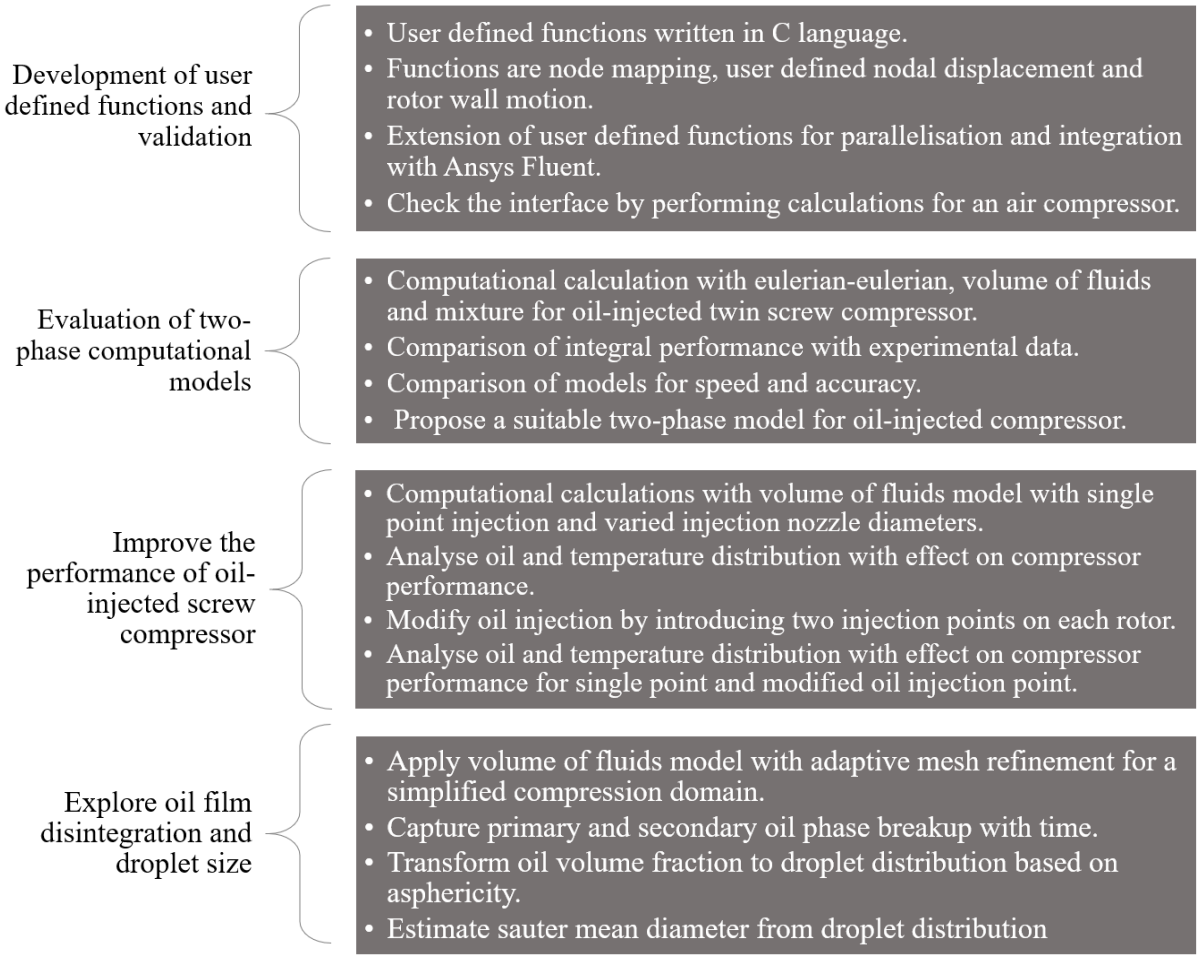

Figure 24. Research Methodology.

3.3 Expected contributions

The major contributions expected to arise from the present research work are in these areas:

- Development of the user-defined functions to handle numerical meshes for dynamic calculation of rotating compressors in parallel mode within the Ansys Fluent solver.
- Achievement of a method to evaluate oil and temperature distribution in a compression chamber and related compressor performance based on oil injection conditions. The investigation using this method will help in improving compressor performance.

Additional contributions include,

- Recommendation of the most suitable multiphase models and setup for analysis of oil-injected screw machines.
- Understanding of disintegration of the oil film as an atomising feature in a twin-screw compressor. It is expected to demonstrate that the oil disintegration in a compression chamber with simplified geometry is caused by the interplay of shear, inertia, surface tension, and centrifugal forces. This method will help to estimate a Sauter mean oil droplet size.

It is expected that the computational methods presented in this thesis will be suitable for modelling screw compressors which could lead to improvements in their performance and efficiency.

Chapter 4 Development and Validation of the UDF for Mesh Manipulation in Ansys Fluent

4.1 Introduction

Two-phase modelling of an oil-injected twin-screw compressor is challenging due to the complex geometry of the machine. The chosen solver should be robust, flexible and customisable to resolve two-phase flows in this machine. Ansys Fluent solver contains various modelling options for calculating multiphase flows along with two-phase interface reconstruction schemes necessary for solver stability. Also, in Ansys Fluent, the standard solver features can be improved by the addition of user-defined functions. Further, Ansys Fluent has been applied widely for various geometries and cases similar to screw compressor, such as oil lubrication in gears where oil distribution in the domain matches well with the experimental visualisation. These studies are explained in Section 2.1.3. Hence, Ansys Fluent is used in this thesis for exploring the oil injection system of twin-screw compressors.

To enable calculation of an oil-injected screw compressor using Ansys Fluent, it is necessary to develop a User Defined Function (UDF) because there are no readily available techniques in the solver to integrate with the external meshes. These functions will enable the import of an initial mesh generated in SCORG into Ansys Fluent with the mesh movement by User Defined Nodal Displacement (UDND) routine performed before each time step. Like any other CFD solver, Ansys Fluent requires extensive resources to calculate multiphase flows. It is necessary to enable calculation on multiple cores in parallel mode. UDF developed in this thesis will import and manipulate grids for twin-screw machines in a parallel mode. This will enable the parallel running of simulations for a twin-screw compressor.

This chapter describes the development of the parallel UDND routine. It presents a validation of the interface on two cases for oil-free air screw compressors with 128mm diameter of the male rotor at pressures of 3 bar and speeds of 6000 and 8000 rpm. The calculated performance is validated against the experimental results obtained at City, University of London.

4.2 Integration of grids with the Ansys Fluent solver

Customised grid generation techniques such as rotor to casing, casing to rotor and single domain method are available for screw machines within an in-house software package SCORG. More details on these techniques can be found in Section 2.1.3 and Appendix 1. A single domain mesh is used in this study. It is chosen because of the accuracy that can be achieved on such mesh than other types, as explained in Appendix 1.3 through the test case. These customised grids from SCORG should be integrated with the computational fluid dynamics solver to perform calculations.

Most of the commercial CFD solvers allow interfacing of the solver and customised grids through specialised routines. Ansys CFX uses a Fortran based interface called 'junction box routine' to exchange customised meshes with the solver. Similarly, STAR-CCM+ has a C++ library that works with the user-defined vertex motion module to pass the node locations to the solver at each time step. PumpLinx has a mesh deformation function that reads an external node file and updates the node's position in the solver. There wasn't such routine available for Ansys Fluent, and therefore, an interface using User Defined Functions (UDF) and Dynamic mesh technique was required. This development is explained in this section.

The User Defined Functions are developed in three parts with extension to work in parallel mode and are hooked to the Ansys Fluent solver through a macro. More information on macros can be found in Appendix 3. The three steps are,

i. Node Mapping

Rotor grid files are generated with SCORG at various rotor angles starting from the first male rotor lobe to the next rotor lobe representing the rotation with time. Each of these rotor grid files contains mesh nodes by the node number and corresponding x,y, and z position. Figure 25 shows an example of a format for the 'rotor.1' file, '1' denoting the first position, generated through SCORG. For this case, the total domain nodes are 907 732, but the node numbers have been clipped to 14 for representation purposes. Files of a similar format are generated for all the rotor positions. All the rotor position files need to be present in the same folder as that of the UDF code in order to extract the information on node numbers and positions.

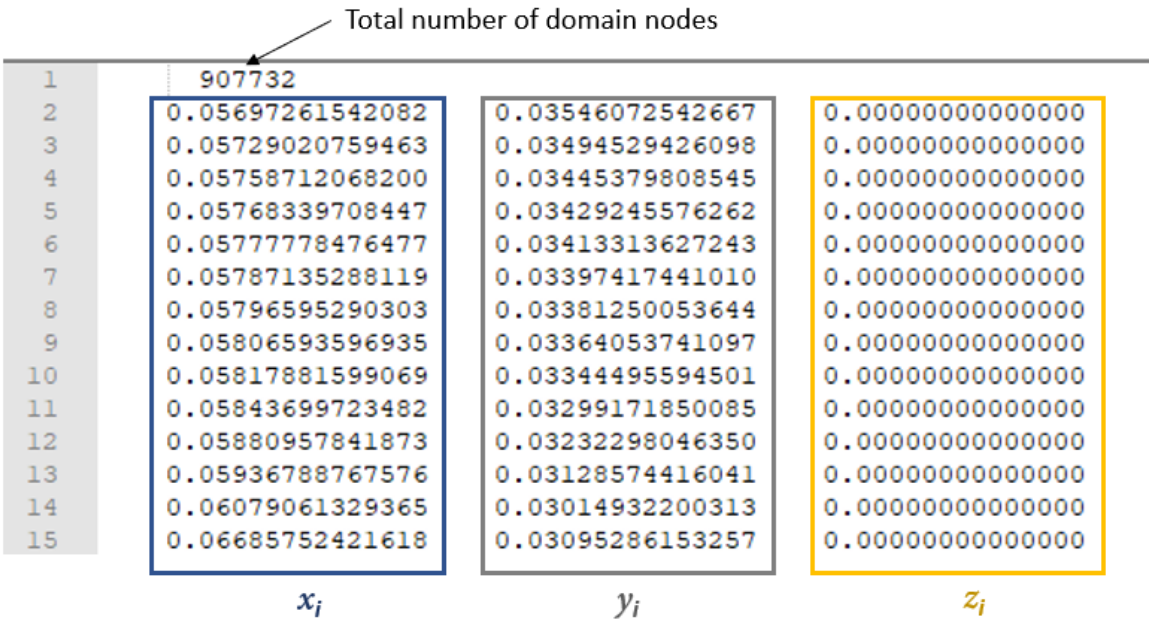

Figure 25. Snapshot of the 'rotor.1' file generated through SCORG.

The initial rotor mesh loaded in Ansys Fluent is allocated certain mesh node numbers, which does not necessarily match the numbers specified in the grid files. When importing mesh for the next time step, these mesh nodes need to be matched to allow mesh movement with time. This process is called 'Node mapping'. The criteria for determining the node numbers is the shortest distance between the nodes of the existing and imported mesh. Distance is calculated from equation (7), where 'j' is a subscript for nodal information in a mesh loaded in Ansys Fluent and 'i' is a subscript for the nodal information in the rotor grid file. The loop will run until the shortest distance is found between the nodes. This procedure is based on the procedure developed for numerical simulations of sliding vane rotary machines explained in [49].

$$distance = \sqrt{(x_j - x_i)^2 + (y_j - y_i)^2 + (z_j - z_i)^2} \quad (7)$$

A typical case of the compressor has around 1 million nodes in the rotor domain mesh, which could take about nearly 24 hours for node mapping on a serial mode. This statement is made based on a serial mode in a Xeon E5v3 32GB processor machine. This lengthy node mapping time will directly affect the case setup time. Therefore, there is a strong need to perform this node mapping operation on a number of processors in order to save the computational setup time.

When node mapping is performed with multiple computer processors, the information passed between the computer processors should be synchronised and time efficient. To achieve this,

it is suggested for a few computer nodes to operate in a serial mode and perform operations of transferring and receiving the data. At the same time, other computer nodes operate in a parallel model performing calculations. This is a part of a standard OpenMP framework in Ansys Fluent [108].

In this case, the parallel computer nodes are used for computing intensive part of the code, such as finding the least distance. Serial node 'node 0' is used for receiving and transferring the data between the parallel nodes. The host or main computer node is used for reading and writing the external data. Operations performed with parallel computer nodes are highlighted with yellow boxes. Serial computer node 0 is highlighted with a grey box, and the serial host node is highlighted with a blue box in Figure 26.

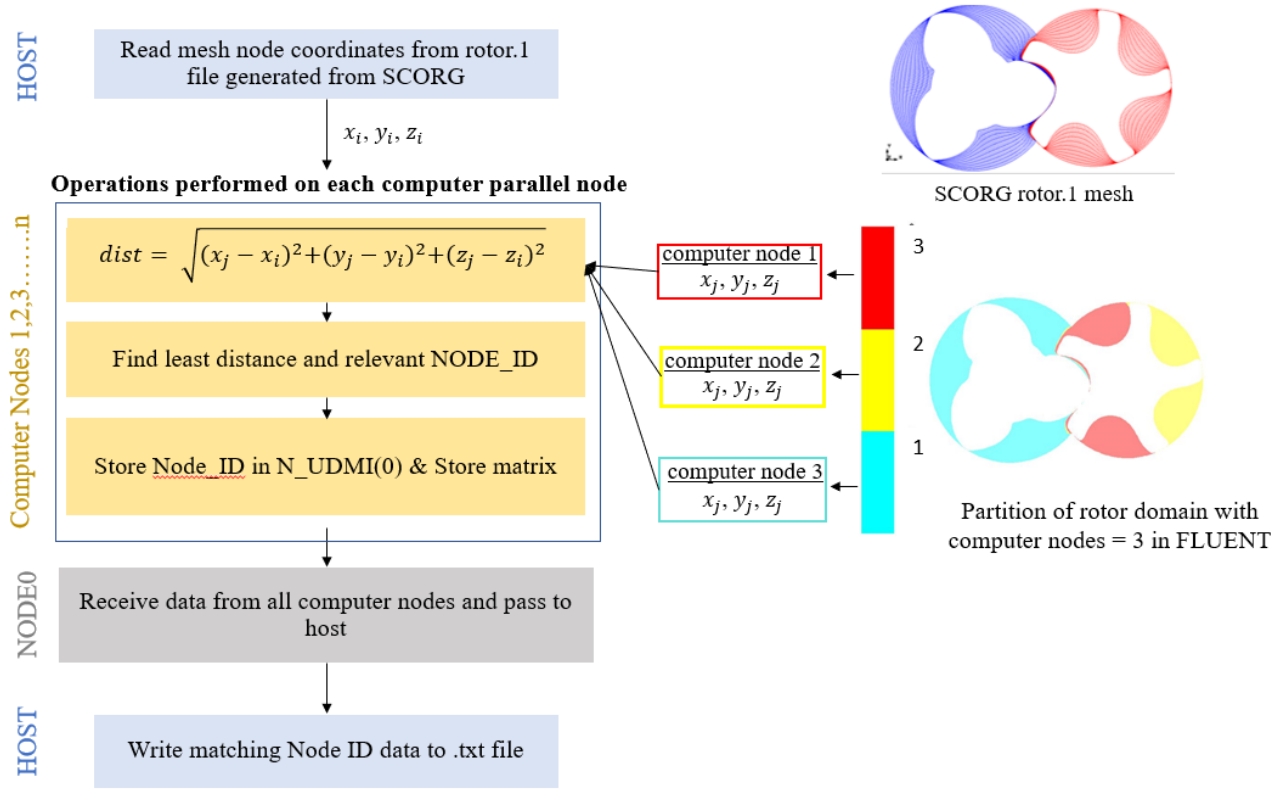

Figure 26. Flow chart for node mapping with parallel mode.

Rotor position files generated from SCORG contain information on x,y,z positions (x_i, y_i, z_i) for each node in the mesh. Among these, the file with the initial rotor position 'rotor.1' is chosen for node mapping, and the information from this file is assigned to an array in the HOST/serial computer node. Array on x_i, y_i, z_i node coordinates are passed to each parallel computer node. The array is passed to all three parallel computer nodes in this case.

The rotor domain mesh in Ansys Fluent is split according to the number of chosen parallel computer nodes, three in this case. Hence, each computer parallel node has certain mesh nodal information x_j, y_j, z_j which is compared with the array data x_i, y_i, z_i through a loop until the minimum distance is found. Then the node number 'NODE_ID' from the SCORG data file that corresponds to the minimal distance is stored in the user-defined memory of Ansys Fluent mesh node 'N_UDMI(0)'. This means that each mesh node in Ansys Fluent will have information on node number matching with the SCORG data file after successful node mapping. Lastly, as a backup, the matching node data information is written to a text file so the information can be easily loaded to N_UDMI(0) if the simulation fails during the calculation. This part of the UDF code written in C language is executed with the Ansys Fluent macro 'DEFINE_ON_DEMAND' before running the CFD calculation.

Figure 27 demonstrates the rotor cross-section at z=0 at the initial time step, indicating the initial mesh loaded with node numbers in Ansys Fluent before the node mapping process. And after the node mapping process, the stored node numbers N_UDMI(0) are shown. The node numbers shown in the figure are the mesh node numbers in a single cross-sectional plane in 2D. Therefore, other colours on the node number are not visible in 2D. However, the figure represents a change in node number positions after node mapping.

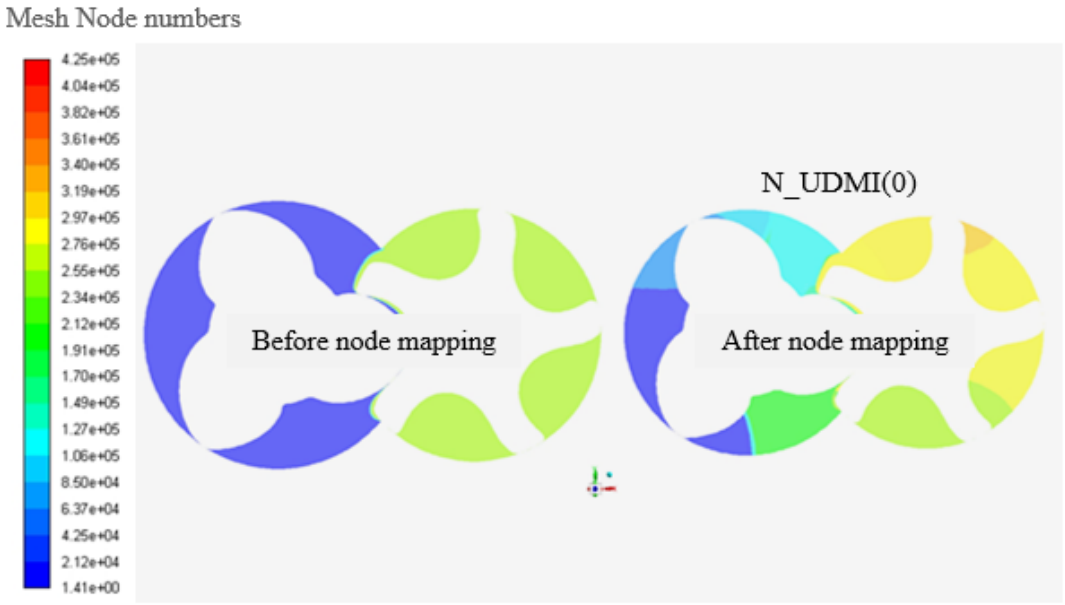

Figure 27. Rotor domain at the cross-section, before and after the node mapping process.

With the same 3-5 lobe combination as depicted above, three cases with different node numbers are compared for the node mapping time with serial and parallel computer nodes on a Xeon

E5v3 32GB processor. Node mapping with parallel mode becomes more prominent when a large number of mesh nodes close to 1 million are present in the rotor domain. Almost a linear improvement in node mapping time is achieved based on the parallel computer nodes compared with the serial mode (Figure 28). When four parallel computer nodes are used, the node mapping process is nearly four times faster than the serial mode for tested mesh nodes from 11,640-907,732 (Table 3).

Table 3. Comparison between the time taken by serial and parallel solver for node mapping.

Case No.	**No. of domain nodes**	**Serial**	**Parallel**		**Improvement in time with parallel mode**
		Time taken (s)	**Computer nodes**	**Time taken (s)**	
Case 1	11,640	~100	4	20-25	3.0-4.0 times
Case 2	58,850	580 (9.6 mins)	4	140 (2.3 mins)	3.1 times
Case 3	523,867	41400 (11.5 hours)	4	11020 (3 hours)	3.2 times
Case 4	907,732	84960 (23.6 hours)	4	24480 (6.8 hours)	3.4 times

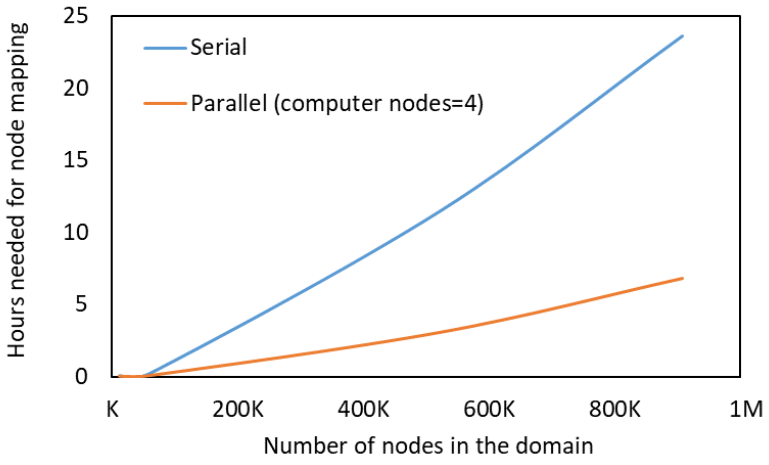

Figure 28. Serial and parallel computing time for node mapping process for various mesh sizes.

ii. User Defined Nodal Displacement

User Defined Nodal Displacement is a fully conservative approach to deform customised grids [49]. This method is used here to deform rotor grids with time.

SCORG grid files are generated for every angular step change defined by the number of angular divisions per rotation. The number of rotor grid files per revolution is dependent on the number of angular divisions. The angular divisions, which are basically the number of mesh divisions from one male rotor lobe to another lobe, are shown in Figure 29. 1° crank angle step was adopted, which means one rotor file for every 1° of rotation. If the rotor file is not available for every 1°, then the linear interpolation is performed between the previous rotor angle and the current rotor angle. The programme written in 'C' decides if interpolation is needed based on the input for the total number of lobes on the male rotor and rotor grid files. For instance, the next section's validation study has a male rotor with 3 lobes, and 50 angular divisions. The rotor will rotate for 2.4° between two consecutive positions defined in the files for which the code will choose interpolation option. Also, in Chapter 5, a computational study performed for an oil-injected compressor with the male rotor with 4 lobes and angular divisions is 90- the rotor will rotate 1° between the positions and the code will avoid the interpolation option.

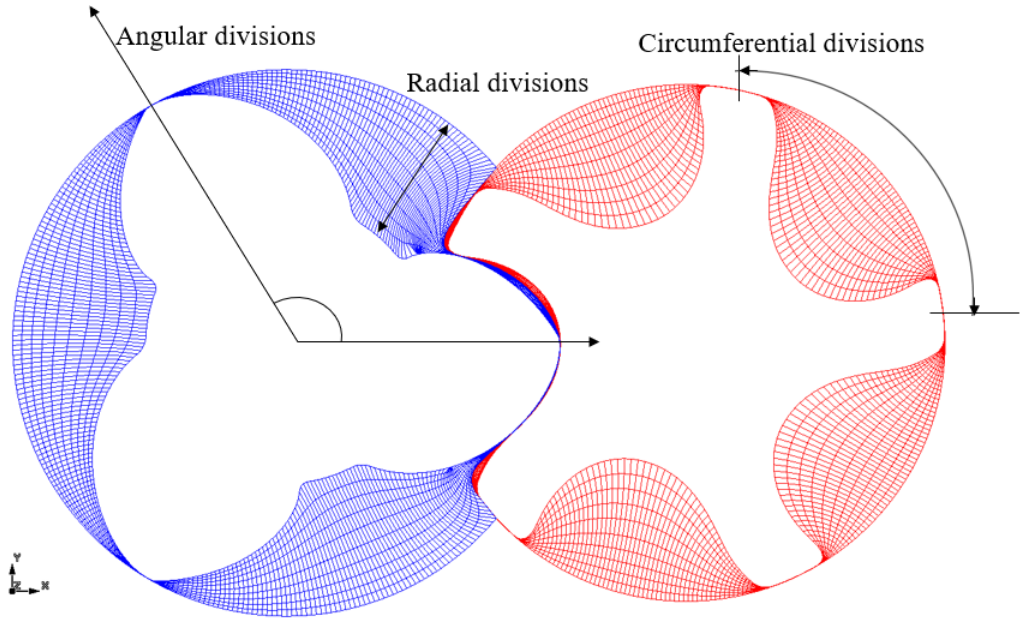

Figure 29. Mesh divisions on the rotor domain.

Figure 30 shows the flow chart with steps required to perform user-defined nodal displacement. The first step (a) is to read rotor text files corresponding to the current angle of rotation. The

coordinates from this text file are passed on to an array that has the same size as the total number of nodes in the Ansys Fluent mesh. This contains just reading and assigning operation, and therefore, it is performed in the serial mode.

After the node mapping was completed by executing the 'DEFINE_ON_DEMAND' macro, each mesh node in Ansys Fluent has a mesh node number information stored in user-defined memory locations. These stored numbers relate to the matching mesh node in the rotor text file generated by SCORG at the initial position. The matching mesh node number information is used to access the x,y,z coordinate information in an array. The x,y,z coordinate information from the array is transferred to the user-defined memory locations N_UDMI (x,y,z) in step (b). Each of the mesh nodes in the domain has a user-defined memory location N_UDMI. In this memory location, the mapped mesh node information (x,y,z coordinates) for that particular node is stored; this is N_UDMI(x,y,z). The stored x,y, and z coordinates are then transferred to the mesh node, translating the node position in the computational domain. In a similar pattern, each mesh node is translated resulting in a deforming domain. This is the third and last step (c). Steps (b) and (c) are performed in parallel computer mode on several processors. Steps (a), (b) and (c) are then repeated for various rotor angles to achieve screw rotor rotation. The developed code performs these steps to account for the deformation of numerical mesh within the screw rotor domain with time. It is programmed within the 'DEFINE_GRID_MOTION' macro.

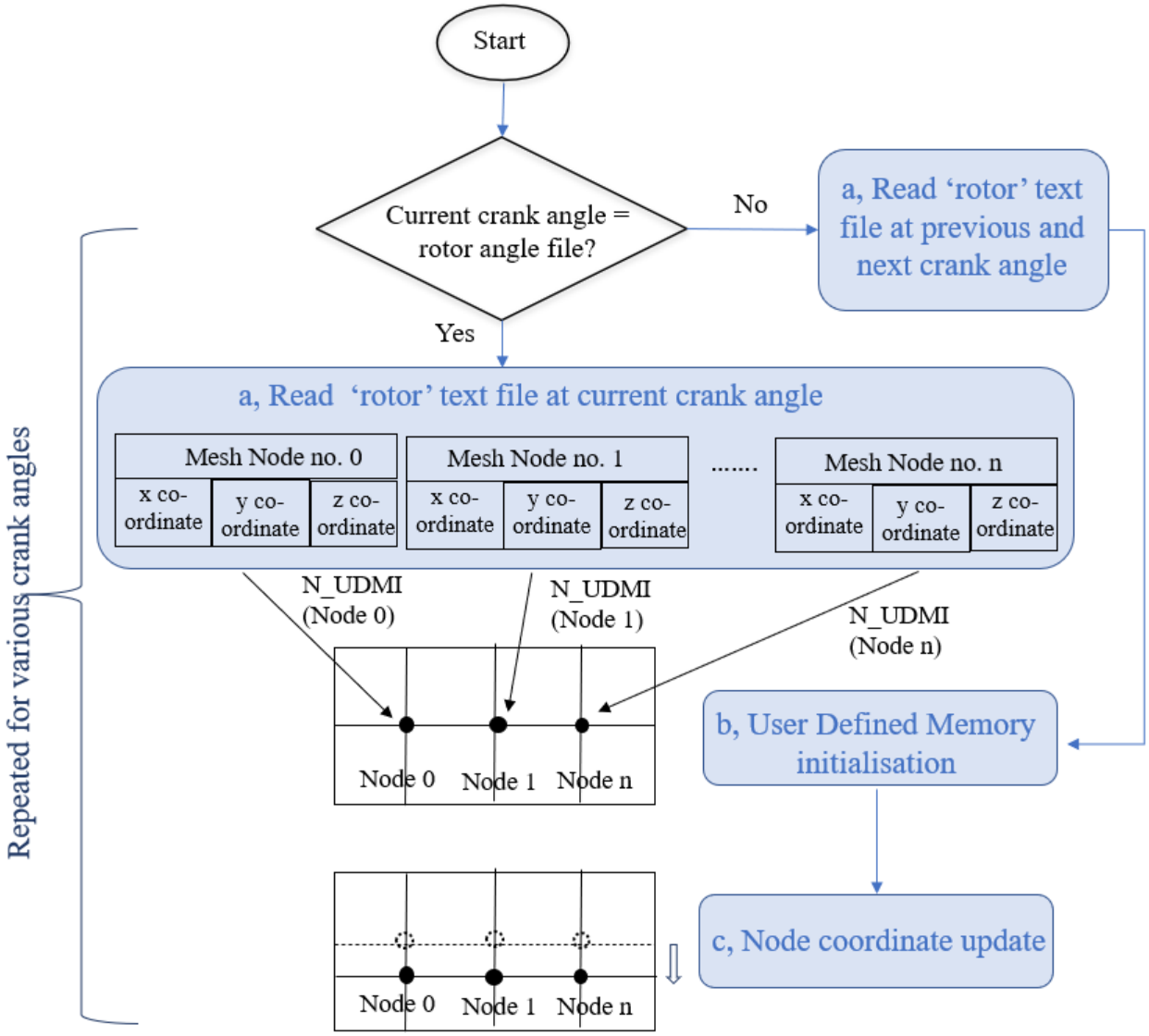

Figure 30. Flow chart for user-defined nodal displacement.

iii. Motion of rotors

The last part of the UDF is to define the wall boundary condition for the male and female rotor walls. Male and female rotor walls are selected through the UDF code, and the rotational speed in rad/s is assigned to the mesh nodes present at the wall region. The predefined male rotor rotational needs to be updated in the code by the user. This value is directly assigned to the male rotor. For the female rotor, this rotation speed is multiplied by the gear ratio.

This code is programmed in the 'DEFINE_CG_MOTION' macro in Ansys Fluent.

Table 4 lists the Ansys Fluent macros in the Ansys Fluent UDF used to perform the functions mentioned above.

Table 4. Summary of user-defined functions with Ansys Fluent macros.

Function	Macro	Execution
Node mapping	DEFINE_ON_DEMAND	Before calculation
User defined nodal displacement	DEFINE_GRID_MOTION	During calculation
Motion of rotors	DEFINE_CG_MOTION	During calculation

4.3 Validation of the User Defined Node Displacement procedure

The developed user-defined functions described in the previous section are applied for a test air compressor to assess:

- If the developed interface between the user-defined functions and the Ansys Fluent solver can successfully calculate cases in a parallel mode?
- How do the setup methods and solution speed in Ansys Fluent compare to another solver such as Ansys CFX?
- How do the results from the Ansys Fluent solution compare with the experimental data and another solver Ansys CFX?

Validation with the test case is necessary to demonstrate confidence in this method before applying a complex calculation of oil-injected twin screw compressors.

4.3.1 Test case details

For simplicity, the oil-free air compressor is chosen for this study. The rotors of configuration 3/5 lobes in male and female rotors respectively are with 'N' profile. The rotors in this profile are generated by the combined rack generation procedure and are optimised to reduce the leakage area between the rotors. More information on the coordinates of this profile can be found in Stosic et al. [109].

The details of the compressor are shown in Table 5. Here the 'Volume index', is the ratio of the volume of the gas trapped between the lobes of the screw compressor at the start of the compression process to the volume of trapped gas between the lobes when it begins to open into the discharge port.

The selected operating condition for this machine is 6000 rpm and 8000 rpm. A uniform pressure of 1.0 bar was specified at the suction, while the discharge pressure is 2.0 bar.

Table 5. Geometrical specifications of the tested oil-free compressor.

Items	Specification
Number of male rotor lobes	3
Number of female rotor lobes	5
Rotor centre distance	93.0 mm
Male rotor diameter	128.0 mm
Rotor length	204.8 mm
Volume index	1.8
Wrap angle	285.0°
Design clearances	120.0 microns

The fluid domain is divided into three zones: rotor domain, suction port, and discharge port (Figure 31). The developed user-defined node mapping functions, user-defined nodal displacement and rotor motion are applied to the rotor domain only. User defined displacement mesh nodes are translated from SCORG to Ansys Fluent to achieve deformation of rotor mesh with time.

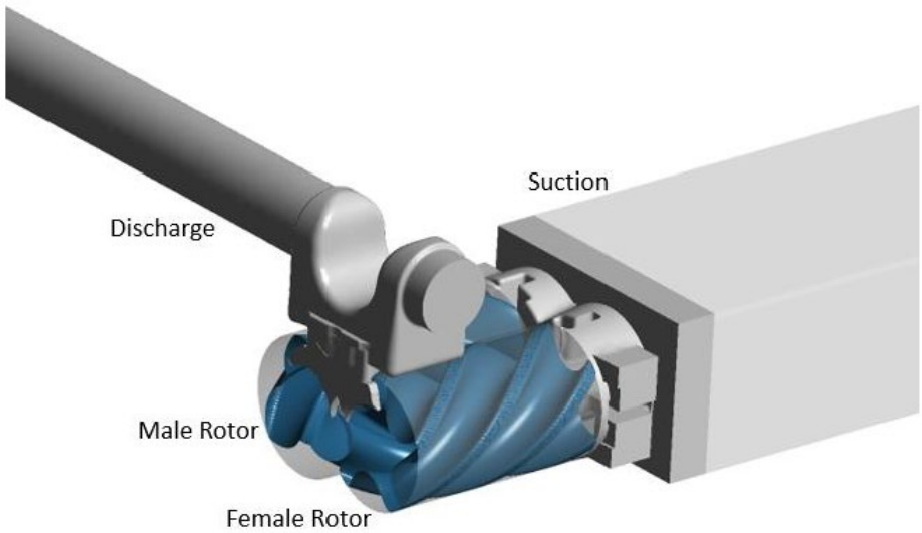

Figure 31. The extracted fluid domain from the CAD model.

Rotor grid mesh generated with SCORG has 350 circumferential divisions with 50 divisions in the interlobe region, 10 radial divisions and 50 angular divisions. The male rotor will rotate 2.4° for every rotation, and therefore linear interpolation with the rotor grids will be performed here. 907,732 hexahedral cells are generated for the rotor domain. The rotor mesh of one cross-section is shown in Figure 29. Suction and discharge have a combined mesh size of 300,736,

which means that the total calculated mesh size is 1,208,468 cells. Grids in the CFD model are generated with the uniform clearances of 60 micrometres in the interlobe and radial gaps which is reduced from the nominal value of 150 micrometres to compensate for the thermal distortion of rotors. The CFD models used in the study do not consider clearance changes, and the axial end clearances are not included to simplify the model further.

Meshed domain and the operating conditions are kept the same for both Ansys CFX and Ansys Fluent solvers. However, Ansys CFX uses the coupled pressure-velocity scheme while Ansys Fluent, in this case, uses a segregated approach with a SIMPLE pressure balancing scheme. Typical Reynolds number for this case is the range of $6.85 \times 10^5 – 9.35 \times 10^5$ depending on the male rotor shaft speed, for which SST k-ω model for both Ansys CFX and Ansys Fluent.

Table 6 and Table 7 summarise and compare boundary conditions, settings and parameters used within the two solvers. Initialised air properties are shown in Table 8.

Table 6. Boundary conditions used.

Parameters	Type- CFX	Type- Ansys Fluent	Value
Inlet Boundary Condition	Opening	Inlet	P_{in} = 0 bar T_{in} = 27°C
Outlet Boundary Condition	Opening	Pressure outlet	P_{outlet} = 2.0 bar
Heat flux for rotor, casing and port walls	Adiabatic walls	Adiabatic walls	0 W/m^2

Table 7. Numerical setup used for CFX and Ansys Fluent.

Parameter	Settings- CFX	Settings- Ansys Fluent
Inlet Boundary Condition	Opening	Inlet
Outlet Boundary Condition	Opening	Pressure outlet
Pressure-Velocity Coupling	Coupled	SIMPLE [110]
Turbulence Scheme	First order upwind	First order upwind
Transient Scheme	First order upwind	First order implicit
Energy Scheme	First order upwind	First order upwind
Transient Inner loop coefficients	10 iterations per time step	30 iterations per time step
Convergence Criteria	1e-03	1e-03
Relaxation parameters	0.1	0.1

Table 8. Air properties.

Phase	Fluid Type	Specific Heat Capacity (kJ/kg K)	Dynamic Viscosity (kg/ms)	Thermal Conductivity (W/m K)
Air	Ideal gas	1.0044	1.831×10^{-5}	2.61×10^{-2}

4.3.2 Test case results

This section shows the CFD simulation results for the test compressor case detailed in the previous section. This simulation is run in parallel mode, demonstrating the successful application of the developed user-defined functions. The results, such as compression chamber pressure, air flow rate, indicated power and specific power, are compared with the results from Ansys CFX and experimental data for accuracy. More information on the test rig, setup, instrumentation and measurement accuracy can be found in the literature [55].

Calculations performed in Ansys Fluent and Ansys CFX are run for nearly 1950 time steps: nearly 13 full rotations of the male rotor. The comparison of solution time per time step is shown in Table 9. Ansys Fluent calculations can be performed in parallel mode with four computer cores in this case.

For this tested case, the solution with Ansys Fluent solver is three times faster than Ansys CFX, and the average error in the air mass flow rate cycle remains similar with both solvers. One main reason for speed is that segregated solver in this case is faster in numerical handling than the coupled solver.

Table 9. Comparison of solver time and mass imbalance.

Solver	Solution mode	Calculation time/time step/core (minutes and seconds)	Error in cycle averaged mass flow (%)
Ansys CFX	Parallel- 4 cores	7 mins and 30 secs	1.01
Ansys Fluent	Serial	2 mins and 40 secs	0.99
Ansys Fluent	Parallel- 4 cores	2 mins and 41 secs	0.99

Predictions of chamber pressure over a compression cycle agree well with experimental data and are close to Ansys CFX predictions (Figure 32 and Figure 33). However, backflow of pressure at discharge is not observed with Ansys Fluent predictions at 8000 rpm (Figure 32) due to the nature of the 'pressure outlet' boundary condition in version 18.2 that does not accept backflow. This boundary condition has been updated with version 19.0 for the case with a male rotor speed of 6000rpm (Figure 33).

Figure 34 shows the integral performance predictions through Ansys Fluent solver and its comparison with experimental data and Ansys CFX. Ansys Fluent solver predicted air flow rate and indicated power with an error of 5.9% and 3.8%, respectively, compared to experimental data. Also, predictions from the Ansys Fluent solver are closer to Ansys CFX predictions by 6.1% for air flow rate and 4.6% for indicated power, respectively.

For this study, grid independence tests have not been conducted. The assessment is limited to:

i) checking the integration of the developed grid interface with the Ansys Fluent solver for transient screw compressor calculations.
ii) checking the case set up for transient compressor calculation.
iii) checking the integral performance data predicted by the Ansys Fluent solver is realistic and comparable to the experimental results.

However, for the case of an industrial oil-injected compressor, grid independence tests have been carried out in Chapter 6, where accuracy in predictions is critical.

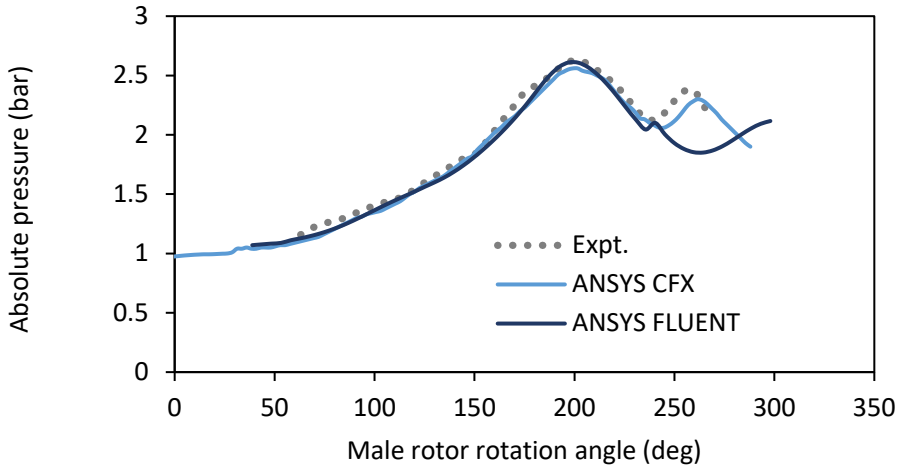

Figure 32. Pressure-male rotor angle plot for 8000rpm.

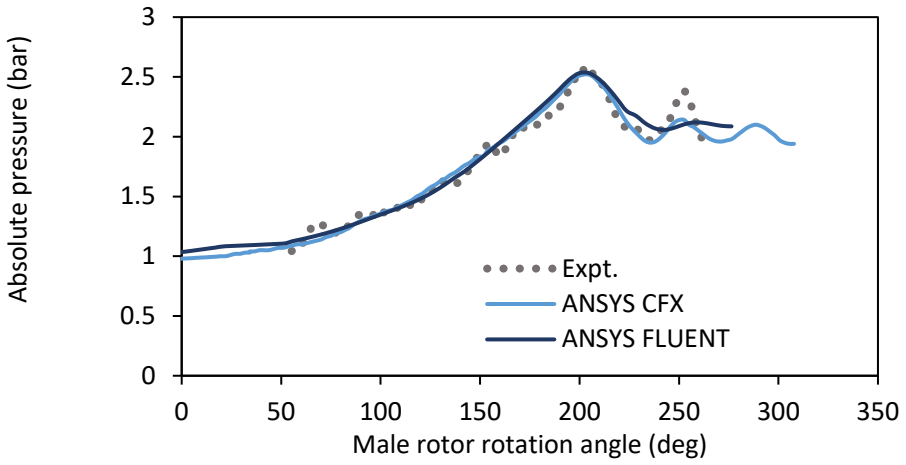

Figure 33. Pressure-male rotor angle plot for 6000rpm.

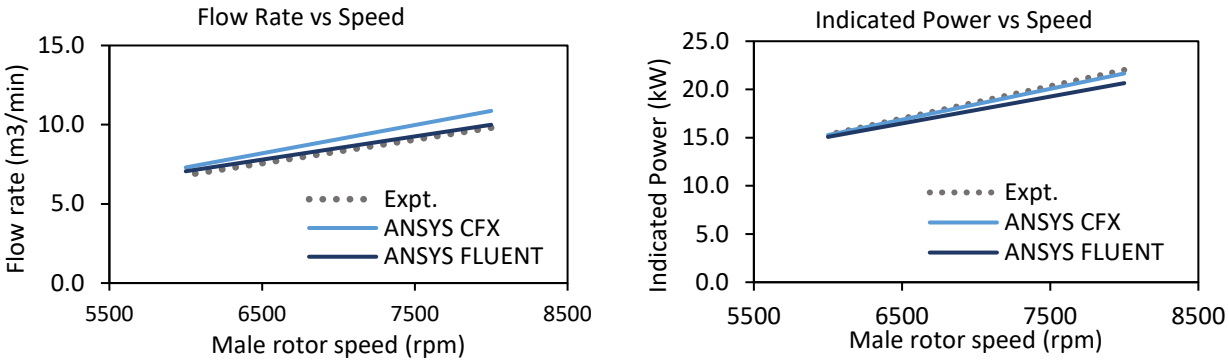

(a) (b)

Figure 34. Comparison of experimental data and CFD predictions for (a) flow rate (b) indicated power.

4.4 Summary

This chapter focuses on customising Ansys Fluent solver for CFD analysis of twin-screw compressors by developing user-defined functions to translate grids generated from SCORG with the rotor rotation parallel framework. The developed framework is then tested for a dry air screw compressor at male rotor shaft speeds of 6000 rpm and 8000 rpm and discharge pressure of 2 bar.

- The development of user-defined functions is carried out in three steps that are node mapping, user-defined nodal displacement and motion of rotor walls.
- Node mapping is a computationally time-intensive process when performed on a serial mode, and therefore it is extended to work on parallel mode.
- Depending on the computer nodes, almost a linear improvement in time is observed when node mapping was performed in parallel. This has enabled a faster setup of simulation case than in the serial mode.
- Achieving user-defined nodal displacement functions in a parallel framework has enabled the Ansys Fluent solver calculations to be performed in parallel mode.
- The integral performance predictions by Ansys Fluent for an industrial air compressor shows that the results agree well with the experimental data. This confirms the case calculation setup with Ansys Fluent.

Lastly, this study ascertains that the developed interface and setup can be used to solve flows in a rotating domain, particularly, industrial oil-injected twin-screw compressor. A developed parallelisation interface with Ansys Fluent will be helpful as the computational time required for multiphase flows is significantly higher than for single-phase flows.

Chapter 5 Comparison of Multiphase Flow Models for Oil-Injected Compressors

5.1 Introduction

Two-phase models are needed for 3D computational modelling of oil-injected twin-screw compressors. Oil injected in screw machines for 3D CFD simulation is treated as immiscible with gas. Models such as Volume of Fluids (VOF), mixture and Eulerian-Eulerian are available within most CFD solvers, including Ansys Fluent solver. They can be applied to calculate gas-liquid flows, and more information on these models along with the governing equations, can be found in Appendix 2. Among these models, it is important to find a suitable one that can be applied for calculations of oil-injected twin screw compressor.

This chapter looks into finding a suitable model whilst applying the user-defined nodal displacement from Chapter 4 with the relevant numerical setup. The simulation is done for an industrial oil-injected twin-screw compressor from Kirloskar Pneumatics Company Limited. The evaluation of the two-phase models is based on solver stability, computational time and accuracy. Choosing and recommending an appropriate model is necessary to conduct multiple simulations of varying oil injection conditions in this thesis.

In this chapter, boundary fitted grids are generated in the SCORG software package, and user-defined nodal displacement explained in Chapter 4 is used to transition the mesh nodes at each solution time step based on the male rotor rotation. The tested oil-injected air compressor operates at a discharge pressure of 7.0 bar and the male rotor shaft speed of 6000 rpm. The performance parameters of air flow rate, power and specific power obtained from the multiphase flow models are compared between the models and the experimental data.

5.2 Compressor description

In this study, the rotors of the oil-injected compressor are with 'N' rotor profile with a 4/5 lobe combination. The male and female rotor profile is shown in Figure 35, where PCD indicates pitch diameters. The full 3D CAD model and the components such as bearings, plugs, screws, dowels etc., are shown in Figure 36. The resolution for the casing is edited to be transparent to show the internal working compression chamber. Figure 37 is a cross-sectional view depicting an oil-injection port. The configuration and dimensions of the compressor are shown in Table 10. More information on oil injection port position can be found in the section 6.2 of Chapter 6.

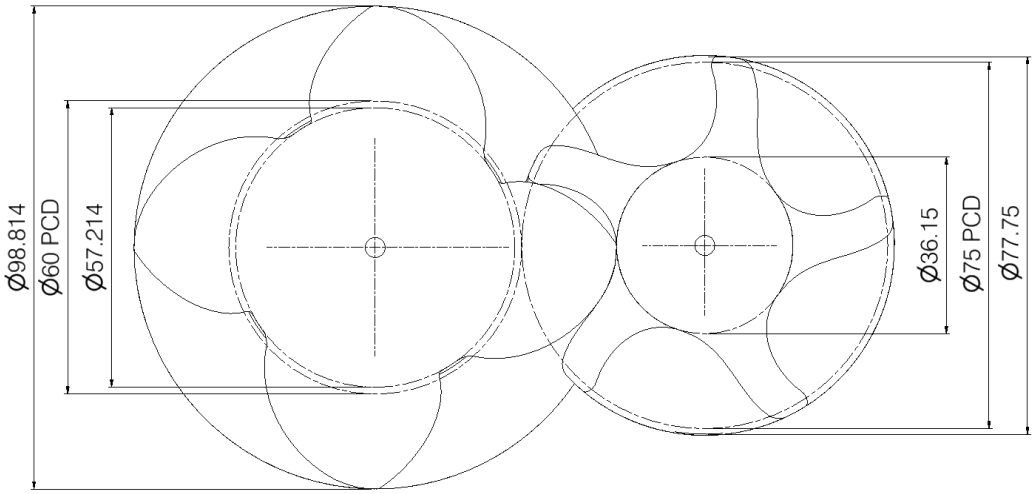

Figure 35. 'N' rotor profile with geometric details for the male and female rotor.

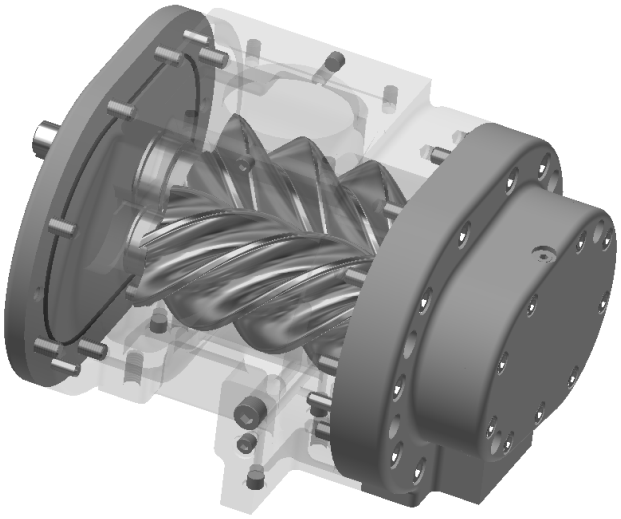

Figure 36. CAD model of oil-injected compressor.

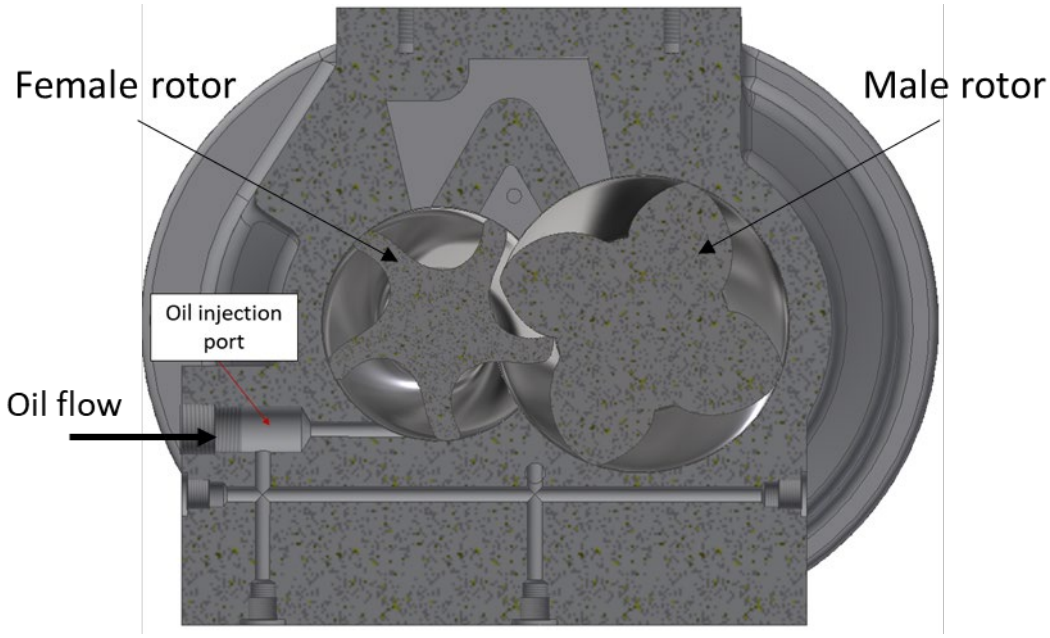

Figure 37. A cross-sectional view of the oil-injected twin-screw compressor illustrating the oil-injection port.

Table 10. Screw compressor geometric characteristics.

Parameter	**Value**
Rotor profile	'N' silent
Rotor lobe combination	4/5
Rotor centre-distance [mm]	67.5
Male rotor outer diameter [mm]	98.8
Female rotor outer diameter [mm]	77.8
Rotor length [mm]	153.14
Male rotor wrap angle [degrees]	306.647
Built-in volume ratio	4.6
Oil port position with male rotor angle [degrees]	68.7
Oil injection port diameter [mm]	5

5.3 Computational domain

The CAD model shown in Figure 36 is simplified by dismissing various elements such as bearings, seals, plugs etc. The compressor elements included in the model for CFD analysis include the male rotor, female rotor, clearances, suction port, discharge port and oil injection ports. The extracted internal fluid domain is shown in Figure 38a. The nominal interlobe, radial and axial leakage gaps are 50 μm.

The screw compressor domain comprises of the deforming and stationary fluid domains, as shown in Figure 38a. The structured numerical mesh for the single moving subdomain around the male and female rotors consists of only hexahedral cells. Grids for the moving fluid domains around rotors were generated in several transverse planes using the in-house software SCORG. The 3D mesh is generated by assembling 2D grids from these transverse cross-sections. One of the transverse 2D grids is shown in Figure 38b. The mesh movement is achieved through the process of node-mapping, which is detailed in Chapter 4.

The suction, discharge, and oil injection ports are stationary fluid domains. The suction port includes both radial and axial sections. The oil injection port was located only on the female rotor side of the casing. Numerical meshes for the stationary domains are tetrahedral cells generated from Ansys Mesher. Numerical meshes of subdomains are integrated by the use of General Grid Interfaces (GGI) [48]. GGI method is available in Ansys Fluent to couple multiple domains into a continuous single domain. For this this case, the coupling between the stationary and rotating domain is non-conformal interface. At the interface, the values are transferred using weighted interpolation.

The three-dimensional grid structure for the full domain with rotors represented by the first layer of numerical cells on the rotor surface is shown in Figure 38c.

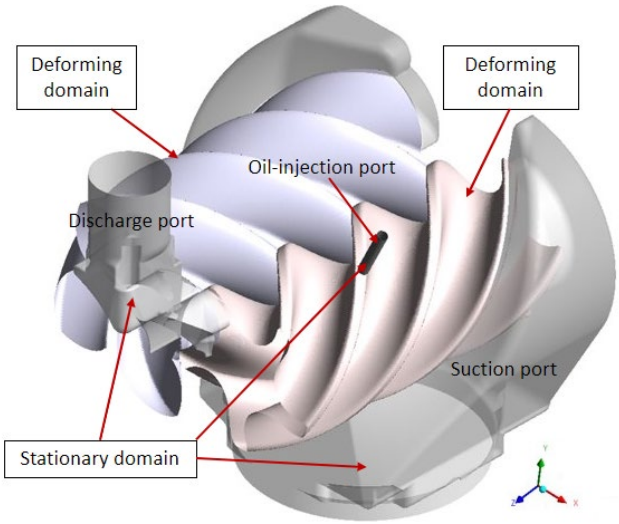

(a)

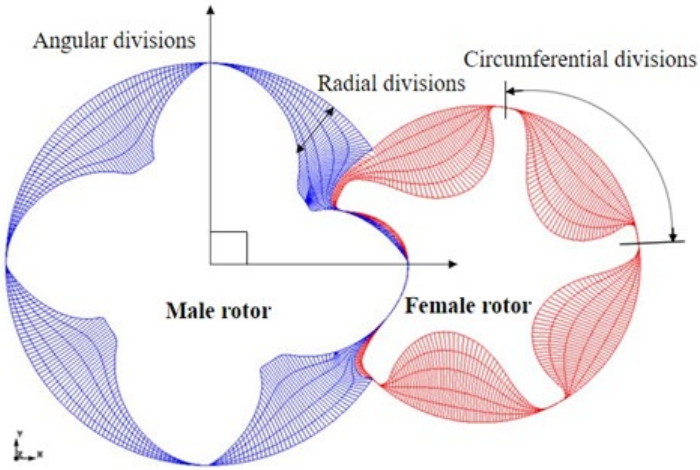

(b)

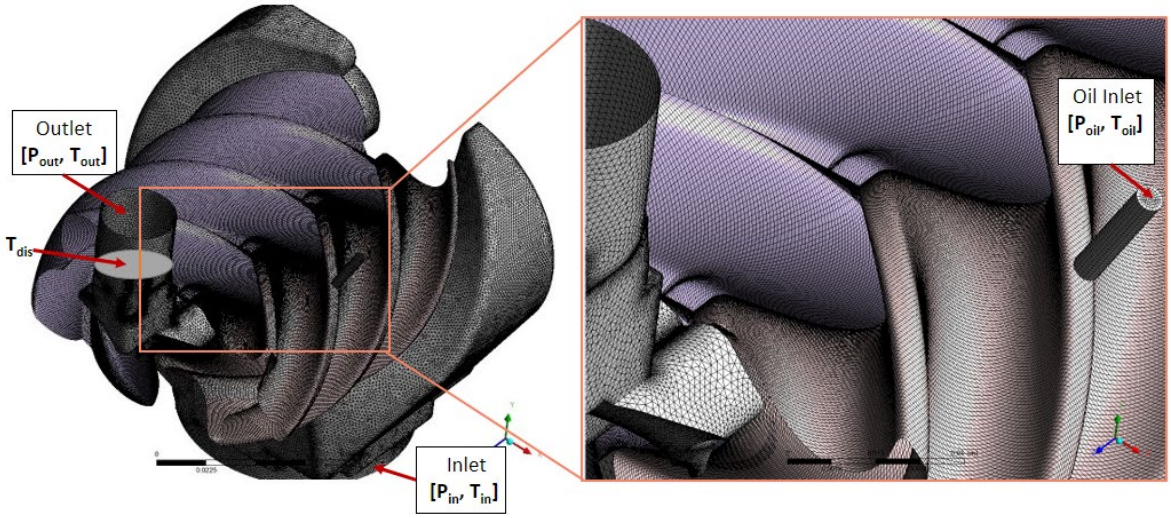

(c)

Figure 38. (a) Computational domain of the compressor, (b) rotor mesh in the transverse plane at 0° male rotor rotation and (c) grid structure of the screw compressor.

The rotor grids for this test case were generated with 60 circumferential division, 5 radial divisions, 90 angular divisions and 77 interlobe divisions that resulted in 924120 elements. The quality parameters of the rotor grids are shown in Table 11. The best quality of rotor grids possible for this particular rotor geometric configuration and clearances was obtained through these divisions. However, the quality of the obtained grids is still lower than the best practice of mesh guidelines suggested by the Ansys Fluent manual [111].

Table 11. Grid quality parameters for the rotor domain.

Parameters	**Value**	**Best practice** [111]
Maximum aspect ratio	326.0	<100.0
Maximum expansion factor	96.0	<20.0
Minimum orthogonal angle	6.9	>20.0

5.4 Case setup and solver issues

The air in the compressor follows ideal gas law, and injected oil is an incompressible fluid. The physical properties of air and oil are shown in Table 12. The inlet boundary condition is imposed with the fixed static pressure and specific temperature. For the outlet boundary, the static pressure and temperature are adopted. The boundary conditions for this case are shown in Table 13. The numerical settings used for the Eulerian-Eulerian, VOF and mixture model are shown in Table 14. The residuals of continuity were observed to decrease below 0.005, but there were limited to 0.07 in order to reduce the case calculation time.

Table 12. Fluid physical properties.

Property	**Air**	**Oil**
Fluid type	Ideal gas	Constant ρ 950 kg/m^3
c_p [J/kg/K]	1004.4	1800
μ [kg/ms]	1.831×10^{-5}	0.08
δ [W/mK]	2.61×10^{-2}	0.18

Table 13. Boundary conditions used.

Parameters	Value
Air inlet pressure, P_{in} [bar]	0
Air inlet temperature, T_{in} [°C]	27.0
Oil inlet pressure, P_{oil} [bar]	7.0
Oil inlet temperature, T_{oil} [°C]	50.0
Outlet pressure, P_{outlet} [bar]	7.0
Heat flux for rotor, casing and port walls [W/m^2]	0

Table 14. Numerical simulation settings with Ansys Fluent.

Parameters	Setting-Ansys Fluent
Turbulence Model	SST k-omega
Pressure-Velocity Coupling	Coupled
Gradient	Green-Gauss Node Based
Volume Fraction	Implicit- Compressive
Turbulence Scheme	Second-order upwind
Energy	First-order upwind
Transient Scheme	Second order implicit
Iterations per time step	200
Convergence Criteria	Continuity 0.07, Velocity 0.001, Energy 1e-06, Turbulence 0.001, Volume Fraction 0.001
Relaxation parameters	0.01

In the mixture model, the drag coefficient accounts for the slip velocity between phases (Appendix 3.1- equation (73)). This drag coefficient is taken as a constant value of 0.44 [106]. The drag coefficient introduces an empirical drift velocity between the air and oil phases with strong coupling. For the Eulerian-Eulerian model, the drag coefficient is the same as the mixture model and Nusselts number for heat transfer between the air and oil phase is assumed as 50. VOF model does not require approximations on slip velocity or heat transfer coefficient as the velocity and temperature parameters are volume/mass fraction averaged. Also, the

mixture model does not consider heat transfer coefficient or Nusselt's number, similar to the VOF model.

Solution stability with Ansys Fluent using VOF and mixture model was achieved using a coupled approach; the solution was unstable with the segregated approach. However, when using the Eulerian-Eulerian model with Ansys Fluent for the same setup as VOF and mixture, the solution was unstable. The instability persisted even when the under-relaxation factors were lowered to 0.01. Hence, 0.01 is reported as a worst-case scenario. Therefore, another solver, Ansys CFX, was tried to check if the stability could be achieved. Similar numerical settings to Ansys Fluent are used with Ansys CFX, as shown in Table 15.

Table 15. Numerical simulation settings with Ansys CFX.

Parameters	**Setting - CFX**
Turbulence Model	SST k-omega
Pressure-Velocity Coupling	Coupled
Gradient	Gauss divergence
Turbulence Scheme	First-order upwind
Energy	First-order upwind
Transient Scheme	Second order backward Euler
Coefficient loops per time step	15
Convergence Criteria	Continuity 0.005, Velocity 0.005, Energy 1e-06, Turbulence 0.005, Volume Fraction 0.005
Relaxation parameters	0.05

A stable solution was achieved with Ansys CFX using the Eulerian-Eulerian two-phase model. The reason for stability lies in the difference between the Ansys CFX and Ansys Fluent solver with cell volume representation. Ansys CFX is the vertex-centred solver, and Ansys Fluent is the cell-centred solver. In the cell-centred approach, mesh generated from SCORG is served as a control volume in the same form. On the other hand, for the vertex-centred method, the mesh generated from SCORG is used as a base to discretise the mesh further and form a control volume [108], [112]. This discretisation can sometimes improve the mesh quality resulting in a stable simulation.

5.5 Experimental investigation

The screw compressor used in this study is measured in the test rig installed at City, University of London to determine the air flow rate, compressor power, specific power, adiabatic and volumetric efficiency. The photograph of the test rig and the instrumentation diagram is shown in Figure 39. Measurements are performed according to ISO 1217:2009 [113]. The air flow rate was measured by means of an orifice plate, according to BS 1042 [114]. The compressor inlet and outlet temperatures were measured by Platinum Resistance Thermometers with errors within ±0.50 °C. Oil temperatures were measured by K-type thermocouples with errors within ± 1.0 °C. All pressures were measured with transducers with errors within ± 0.6%. The compressor speed was measured by a shaft encoder with ±2.7% error. The compressor torque was measured by the torque meter with a strain gauge transducer with an accuracy of ±0.25%. All tests were carried out at the rotational speed of 6000 rpm. The indicated power is 85% of the total power as it was assumed that mechanical losses are 15%.

P, T, T_{ql}, and S are respectively the pressure, temperature, torque and speed measurement points in the compressor test rig. CompactRIO (CRIO-9022) system and Labview software were used for data acquisition and calculation of the performance. Up to 20 readings of dynamic data were collected every 10s and averaged to eliminate any measurement noise. Measurement points in the test rig are denoted with 'I' in Figure 39. Measured pressures, temperatures, shaft torque, rotational speed are substituted in equations (9),(10),(11),(12) and (14) to obtain compressor performance parameters of air flow rate, power, adiabatic efficiency, volumetric efficiency and specific power.

$$PW_{ad} = \frac{\gamma}{\gamma - 1} P_1 . 60 . Q_v . \left[\left(\frac{P_2}{P_1} \right)^{\frac{\gamma - 1}{\gamma}} - 1 \right] \tag{8}$$

In equation (8), PW_{ad} is the adiabatic power, γ is the specific heat ratio of air, P_1 is the inlet pressure, P_2 is the discharge pressure and Q_v is the volume flow rate of air.

$$PW_{comp} = \frac{\tau N}{60} \tag{9}$$

In equation (9), PW_{comp} is the compressor power. It is calculated through the measured torque τ at point T_{ql} (I-11) and compressor speed N (I-12) at point S in the test rig.

$$Q_v = \frac{C_d e \pi D_i^2 \sqrt{\frac{2dp}{\rho_0}}}{4\sqrt{1 - \beta^4}} \tag{10}$$

In equation (10), Q_v is the volume flow rate of air that is calculated using correlations and measured values. Correlation C_d is the discharge coefficient, and e is the expansion factor taken from section 7.3.2.1 in the reference [114]. These correlations are elaborated in the equation (16) and (19). D_i is the orifice, and β is the ratio of orifice diameter (D_i) to pipe diameter (D), as shown in equation (15).

dp is the differential pressure measured across the orifice plate at point I-6. ρ_0 is the upstream density calculated using measured pressure and temperature at points I-5 and I-6 in the test rig.

$$\eta_{ad} = PW_{ad}/PW_{comp} \tag{11}$$

$$\eta_v = Q_v/Q_{th} \tag{12}$$

η_{ad} is the adiabatic efficiency and η_v is the volumetric efficiency. The value of the theoretical air flow rate (Q_{th}) for the compressor in this study is 4.35 m^3/min.

$$PW_i = 0.85PW_{comp} \tag{13}$$

The indicated power (PW_i) is assumed to be 85% of the compressor power considering 15% as mechanical losses.

$$w_{comp} = PW_{comp}/Q_v \tag{14}$$

w_{comp} is the compressor specific power which is calculated through compressor power (PW_{comp}) and volume flow rate of air (Q_v) .

$$\beta = \frac{D_i}{D} \tag{15}$$

$$C_d = 0.5959 + 0.0312\beta^{2.1} - 0.1840\beta^8 + 0.0029\beta^{2.5}\left(\frac{10^6}{Re}\right)^{0.75} + \frac{0.09L_1\beta^4}{(1-\beta^4)} - 0.033L_1(\frac{1}{2})\beta^3 \tag{16}$$

Reynolds number (Re) in the equation (17) can be written as,

$$Re = \frac{4Q_v}{\pi D_i \mu} \tag{17}$$

The viscosity of the fluid μ in kg/ms is obtained through Sutherland viscosity law, equation (18), dependent upon the orifice inlet temperature (T_{op}) in K at the measurement point I-7 [115].

$$\mu = 1.458 \times 10^{-6}\frac{T_{op}^{1.5}}{T_{op} + 110.4} \tag{18}$$

$$e = 1 - 0.41 + 0.35\beta^4\left(\frac{dp}{1.4P_{op}}\right) \quad (19)$$

dp and P_{op} in equation (19) are the differential pressure across the orifice and upstream pressure, measured at the points I-6 and I-5, respectively.

Instruments used for the experiments are of the laboratory grade with relatively low error. However, this error affects the macro properties like flow rate of air, power and specific power. The error propagation for air flow rate measured through an orifice plate, power and specific power [116] considering their dependent variables are shown in equations (20), (21) and (22).

Error percentage for β value of 0.198 is 4% and C_d is 0.2% [116]. It resulted in the following accuracy: air flow rate 3.7%, power input, 2.7%, specific power 4.5%, and oil flow 12.8%. The error percentage with oil flow is higher as it is a calculated value using the equation (23) rather than being measured.

$$\delta PW_{comp} = \sqrt{(\delta\tau)^2 + (\delta N)^2} \quad (20)$$

$$\delta Q_v = \sqrt{2(\delta dp)^2 + 2\left(\left(\delta P_{op}\right)^2 + \left(\delta T_{op}\right)^2\right) + (\delta\beta)^2 + (\delta C_d)^2} \quad (21)$$

$$\delta w_{comp} = \sqrt{(\delta Q_v)^2 + (\delta PW_{comp})^2} \quad (22)$$

$$\dot{m}_{oil} = \frac{PW_{comp} - \dot{m}_{air} cp_{air}(T_2 - T_1)}{cp_{oil}(T_2 - T_{oil})} \quad (23)$$

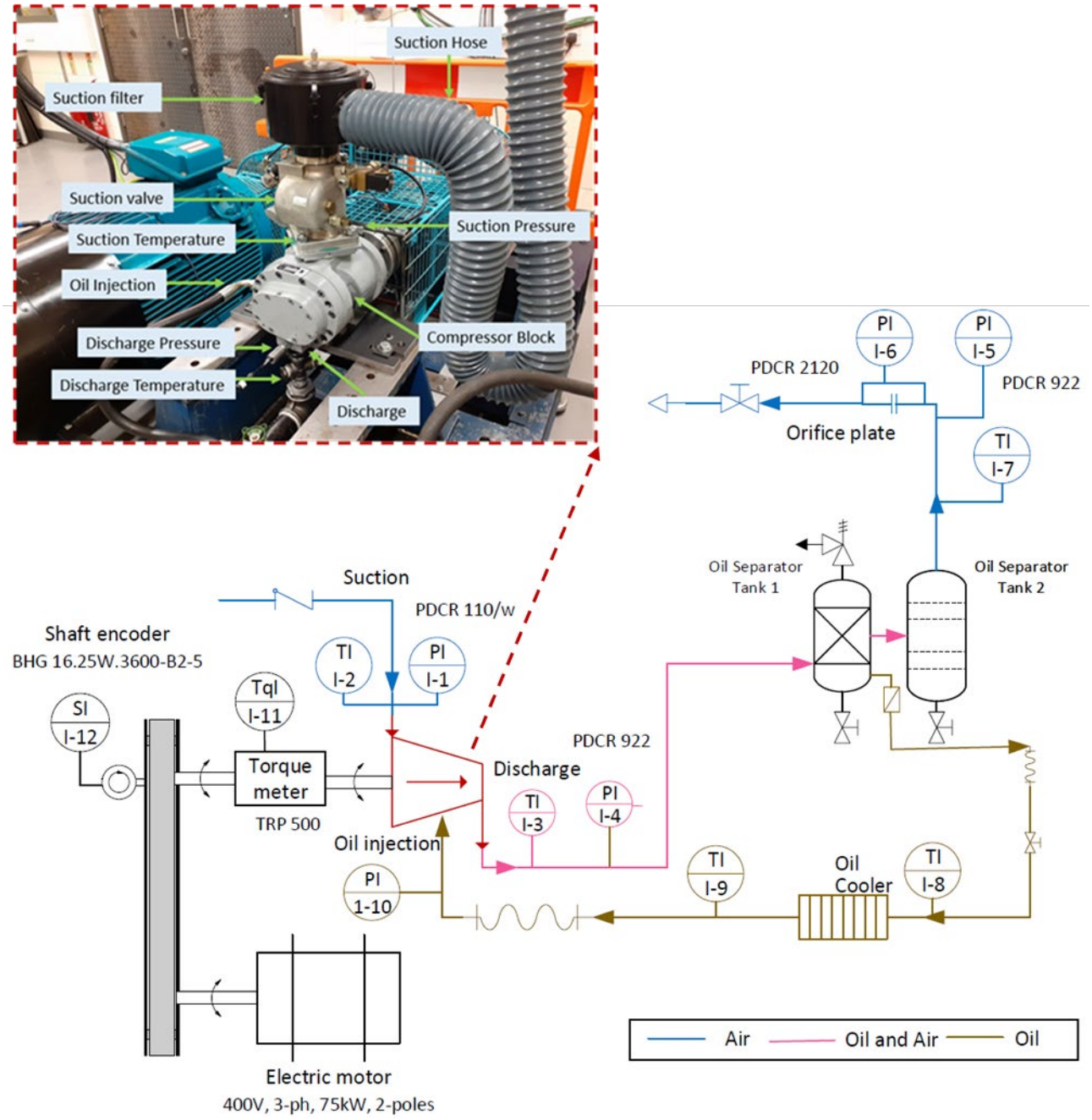

Figure 39. Layout and instrumentation of the compressor test rig.

Table 16 shows the measured results for pressure ratio 7 and the rotational speed of 6000 rpm.

Table 16. Test result obtained for the case study.

Pressure ratio P_2/P_1	**Indicated Power PW_i [kW]**	**Volume flow rate Q_v [m³/min]**	**Specific Power w_{comp} [kW/m³/min]**
7.0	18.4	3.6	6.5

5.6 CFD results and discussion

Using the generated mesh with user-defined displacement and numerical settings, the case is run for mixture and VOF models in Ansys Fluent and Eulerian-Eulerian model in Ansys CFX. The internal chamber characteristics of pressure and oil volume fraction are compared between the two-phase models. Additionally, the integral performance parameters of air flow rate, power and indicated power are recorded and compared between the models and the experimental data. Lastly, solution times are recorded for each model, and recommendation is made for a suitable two-phase model based on solution time and accuracy.

5.6.1 Pressure and oil distribution

Figure 40 shows a variation of pressure in the compression chamber with the change in the male rotor angle. Oil is injected at 68.7° after the closing of the suction port. At 7.0 bar discharge pressure and 6000 rpm, the peak pressure reaches around 9.0bar. After this, the discharge port opens at 260°. Once the port is open, pressure drops in the discharge port leading to the outlet pressure of 7.0bar. The same level of pressure pulsations is noticed in both models. Both models follow a similar pressure profile, with a mixture model achieving a slightly higher peak pressure of 0.08bar than the VOF model. This difference is very small compared to the order of magnitude of the peak pressure.

The distribution of pressure in the first layer of the fluid cell close to rotors and ports surfaces with an oil iso-volume fraction of 0.035 is shown in Figure 41. Again, pressure distribution on the surfaces is alike for both models. From the same figure, the difference in oil content or distribution can be observed with the VOF and mixture models, which is discussed in the next section.

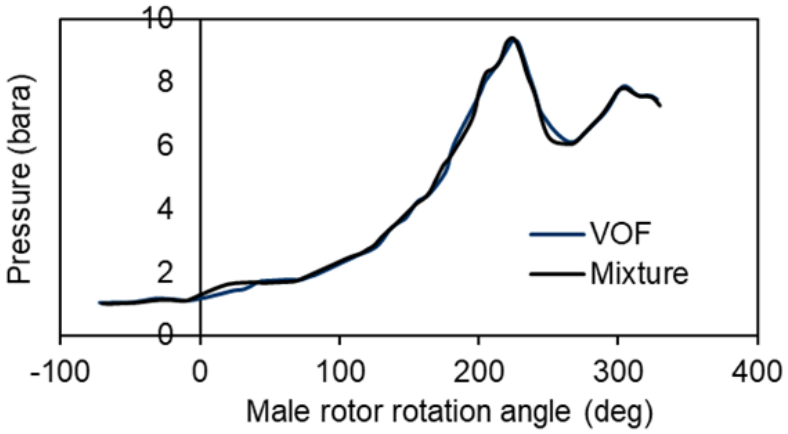

Figure 40. Pressure-male rotor angle plot for VOF and mixture model.

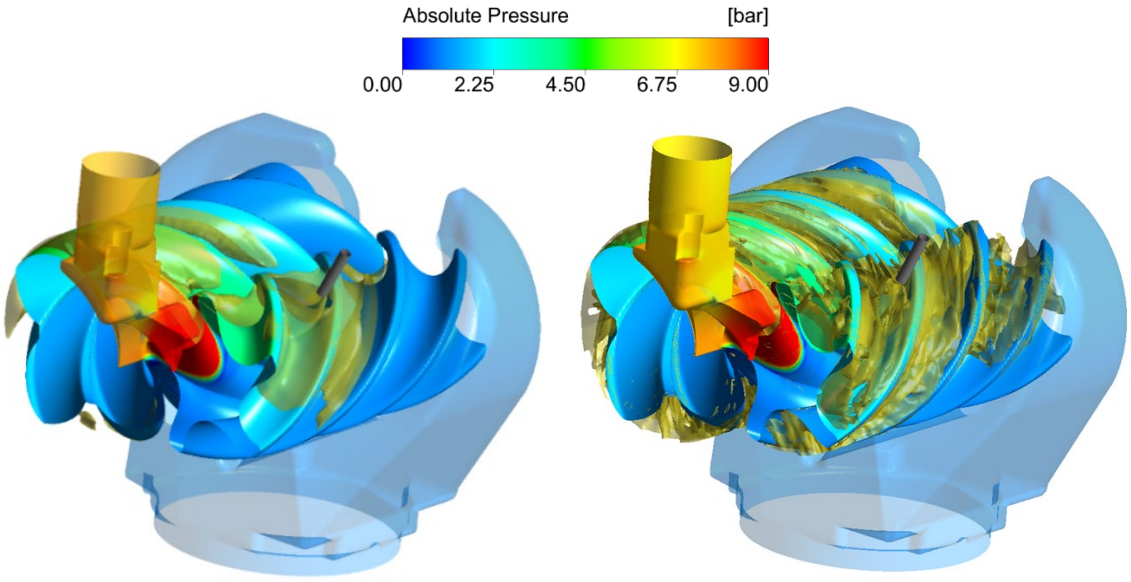

VOF (a) Mixture (b)

Figure 41. Domains coloured by pressure at the layer of fluid cells close to the surface with oil volume fraction iso-surface of 0.035 for (a)VOF model and (b) Mixture model.

To clearly distinguish between oil distributions with VOF and the mixture models, the rotor surface is made to be un-contoured, and oil is shown as an iso-surface of oil volume fraction 0.035 (Figure 42). Adding to this, Figure 43 indicates the mass flow rate of oil injected in the compression chamber with respect to the male rotor angle. The oil injection to the compression chamber is discontinuous, being controlled by the female rotor lobe. The oil port is closed when the female rotor tip comes in contact with the oil injection port opening during rotor rotation. Though the amount of oil injected remains the same in both models, the difference in oil content within the compression chamber is noticed. With the

VOF model, the distribution of oil volume fraction is more like a constant value in specific regions, and oil distribution on the suction side is less than the volume fraction of 0.035.

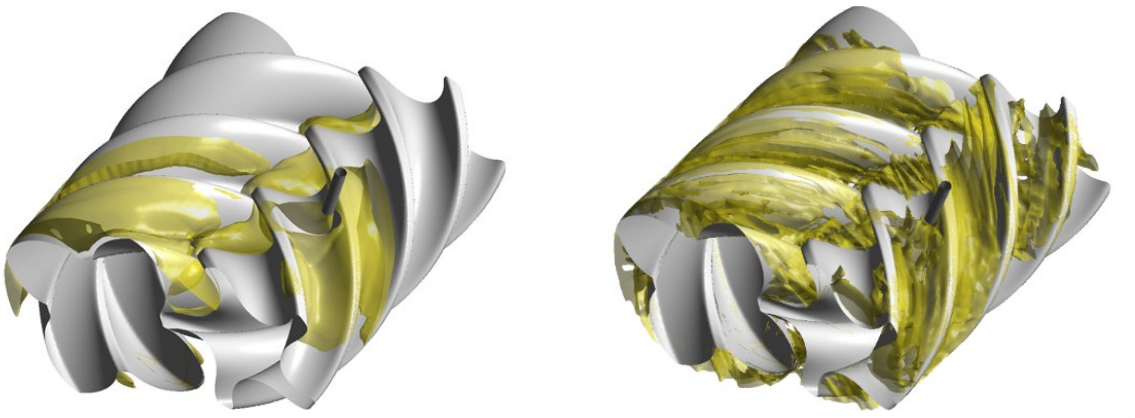

VOF (a)

Mixture (b)

Figure 42. Oil volume fraction iso-surface of 0.035 for (a) VOF model and (b) Mixture model.

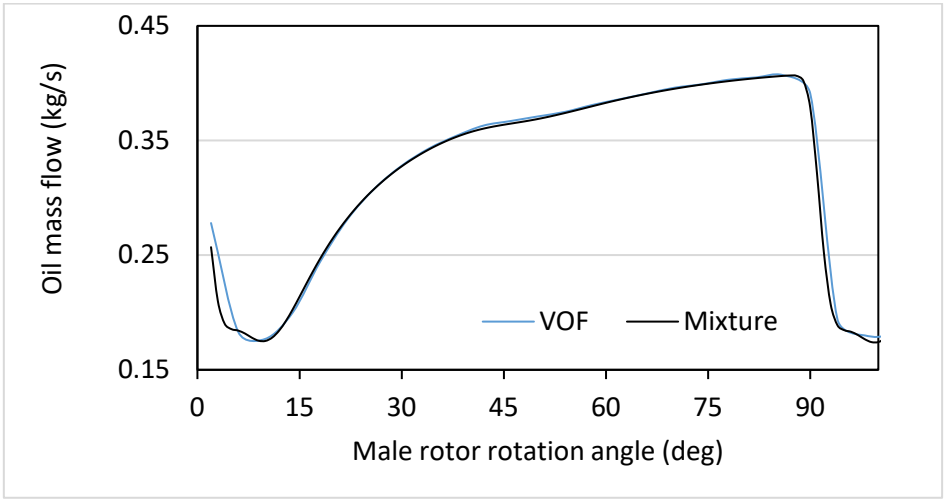

Figure 43. Oil injection mass flow according to the male rotor rotation angle.

The oil distribution study is further focused on the oil volume fraction distribution on the male rotor surface. Figure 44 shows the distribution of oil on the surface obtained from the mixture and VOF models as well as the Eulerian–Eulerian model. The Eulerian–Eulerian model has not been used for the comparison of integral values because this model was previously solved with Ansys CFX with the same geometry and similar boundary conditions. The difference was in the male rotor shaft speed of 6572 rpm. The Eulerian-Eulerian model could not be solved with Ansys Fluent due to stability reasons. The slight variation in the male rotor speed between

Ansys CFX and Ansys Fluent will quantitively affect the amount of oil. Still, it will not affect oil distribution characteristics significantly with various multiphase flow model pattern. Therefore, it is reasonable to assume that this approach will still give a good qualitative comparison of different multiphase models.

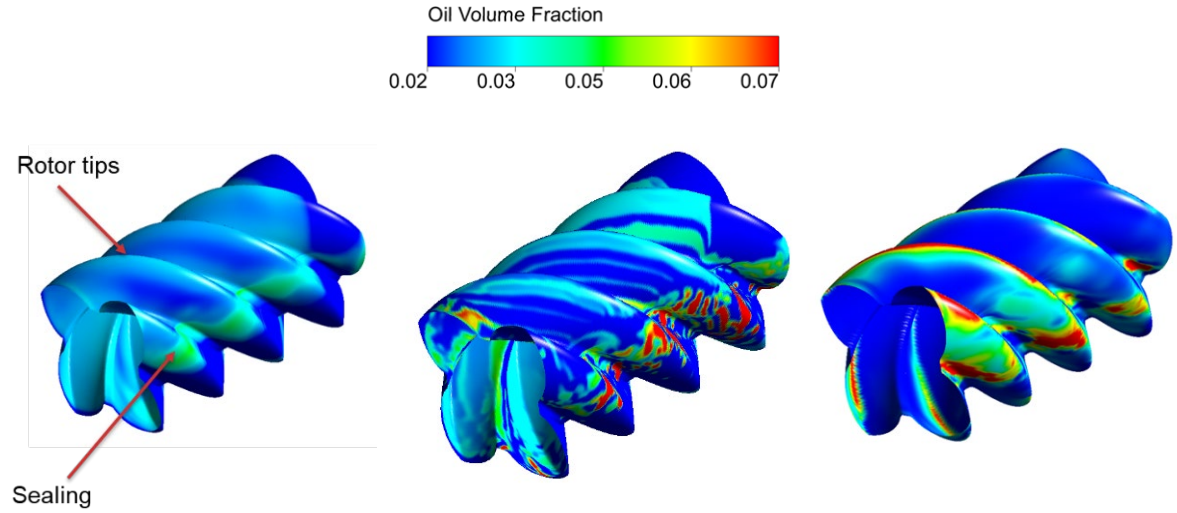

VOF Mixture Eulerian-Eulerian

(a)

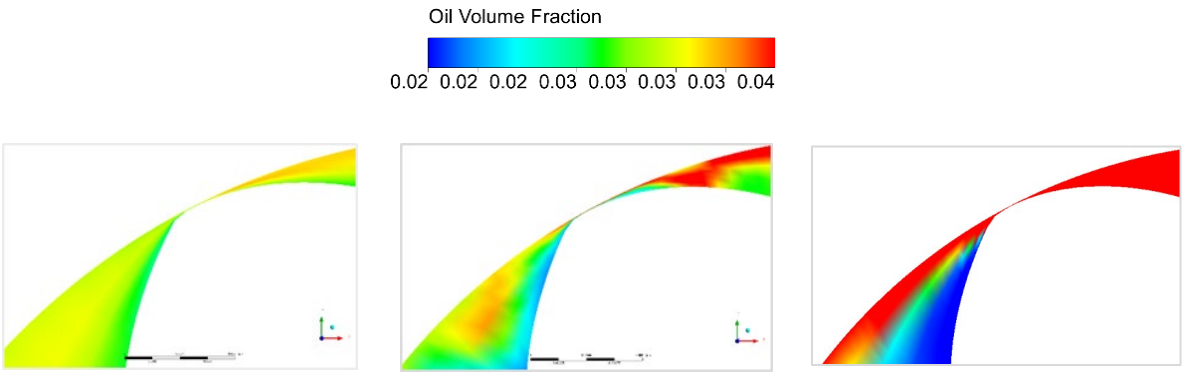

VOF Mixture Eulerian-Eulerian

(b)

Figure 44(a) Male rotor surface coloured by oil volume fraction and (b) rotor tips coloured by oil volume fraction.

Figure 44 shows the comparison of oil distribution with three different multiphase models. The VOF model shows a smooth transition in oil concentration on the rotor surface. A relatively higher oil volume fraction is observed at rotor tips and along the sealing line. With the mixture model, strips of oil volume fraction are observed on the rotor tips, and a higher oil volume fraction of pitted oil appear along the sealing line. Clearly, with the mixture model, a higher volume fraction of oil is observed at the sealing line than in the VOF model, but the distribution is not smooth and continuous. This is due to the averaged fluid velocities in a cell for the air and oil phase with the modelled relative motion between the air and the oil phase using a mixture model. In contrast, the VOF model tracks the oil phase resulting in smooth reconstruction of the interface between air and oil.

However, with the Eulerian-Eulerian model, a substantially higher content of the oil is observed on the rotor tips with the clear gradient surrounding the tip region. The Eulerian–Eulerian solves velocities of each phase individually and couples them through the interphase momentum transfer term. In this way, it is expected that the Eulerian–Eulerian model represents the oil distribution better than the mixture model, where slip is more of an empirical term or VOF with no consideration of slip or drag at all.

5.6.2 Integral performance

Table 17 shows the comparison of calculated air flow rate, indicated power and mass imbalance error with experimentally measured values. The resulting torque on each of the rotors can be calculated from the surface pressure. The power due to the torque on the rotors in the CFD model can be considered as indicated power. This indicated power can be calculated according to the equation (24). For this compressor design , number of lobes on male rotor (z_m) is 4 and of female rotor (z_n) is 5.

$$PW_i = \frac{2\pi N(\tau_m + \frac{z_m}{z_n}\tau_g)}{60} \tag{24}$$

Both models can predict overall values of air flow rate and indicated power close to measured data with a good mass balance. Flow predictions with the mixture model are as close as 0.88%, and with the VOF model, the difference is 3.46% compared to the experimental value.

This can be due to relatively higher radial leakage velocities seen with VOF compared to the Mixture model (Figure 45). More importantly, reducing the convergence criteria in Table 15

to 0.001 for the continuity equation and extending the solution time so the male rotor can complete at least 20 rotations can improve the performance predictions as well as mass imbalance error. Nevertheless, the obtained predicted performance is still close to experimental data, giving a strong indication of solution times.

Overall, indicated power is slightly better predicted at a 4.55% error percentage with the Mixture model than VOF at 5.68%. Also, it can be noticed that the mass imbalance percentage is higher with the VOF model at 1.54%, leading to a higher error in flow prediction at 3.46%.

Table 17. Comparison of performance parameters for various multiphase models and experimental data.

Serial No.		**Air Mass Flow Rate (kg/s)**	**Indicated Power (kW)**	**Air Mass Flow Error (%)**	**Power Error (%)**	**Mass Imbalance Error (%)**
1	Experimental measurement	0.070	18.4			
2	VOF	0.068	17.3	-3.4	5.6	1.5
3	Mixture	0.071	17.5	0.8	4.5	0.1

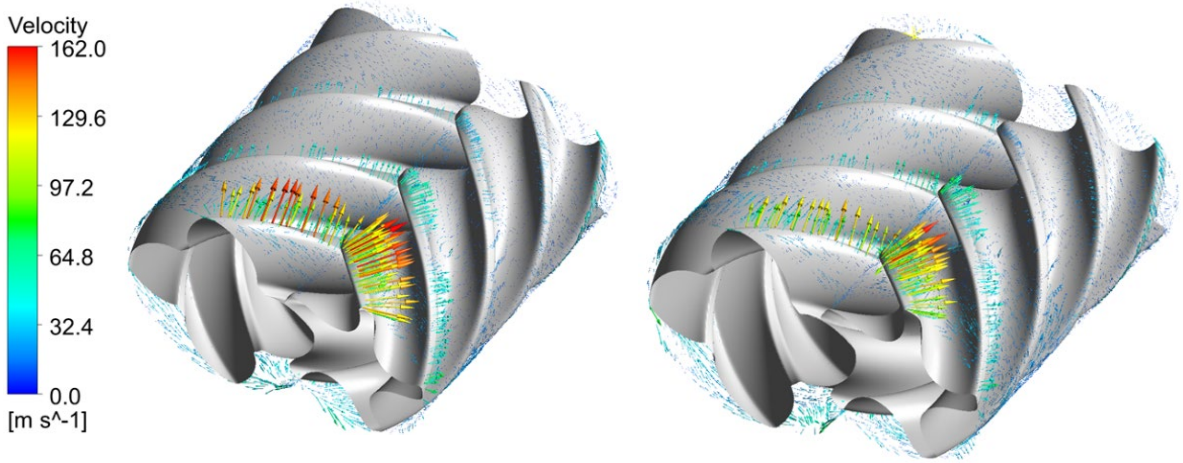

VOF Mixture

Figure 45. Velocity vectors at radial leakages with VOF and Mixture model

Lastly, it is witnessed that VOF and mixture models require lower solution time per timestep when compared with the Eulerian-Eulerian model solved in Ansys CFX (Table 18). The mixture model takes a slightly longer time than VOF as it solves additional terms related to slip and drag forces. The concluding remark is that both VOF and mixture models are computationally economical, but the VOF model is computationally cheaper.

Table 18. Comparison of solution times for VOF, mixture and Eulerian-Eulerian model.

Parameter	**VOF (Ansys Fluent)**	**Mixture (Ansys Fluent)**	**Eulerian-Eulerian (Anys CFX)**
Iterations per time step	2.00×10^2	2.00×10^2	5.00×10^0
Calculation time per time step per core (mins)	40.5	42.0	50.5
Time improvement (%) (compared to Eulerian-Eulerian)	24.7	20.2	

5.7 Summary

The two-phase models such as VOF, mixture and Eulerian-Eulerian are used for solving a test case of an oil-injected twin screw compressor. The compressor operates at a rotor shaft speed of 6000 rpm and 7.0 bar pressure. A comparison is made between the different models in terms of instantaneous values within the chamber and integral parameters. The key conclusions from the study are:

- Oil distribution within the compression chamber differs between the mixture and VOF models. With the VOF model, smooth distribution of oil volume fraction was observed due to the air and oil being treated as non-interpenetrating phases. With the mixture model, the oil distribution is discontinuous since the phases are penetrating, and the empirical slip term between phases is included.
- The key nature of oil, such as a high concentration of oil volume fraction near the radial and interlobe leakages, remains apparent with all tested two-phase models.
- Both mixture and VOF models are capable of predicting the overall performance of the flow and power close to the measured values. The mixture model predicts flow at 0.9% and power with a 4.5% difference from the measured values. The VOF model predicts flow with 3.4% and power with 5.7% error.
- Mixture and VOF models are computationally efficient, and on average, a 22% time reduction was observed using these models in comparison with the Eulerian-Eulerian model, albeit being calculated in different solvers.

The VOF model requires the shortest solution time for the tested case with nearly 24.7% improvement in computational time compared to the Eulerian-Eulerian model. Based on the stability, solution time and comparable accuracy to experimental data, the VOF model is recommended for performing multiple case studies of an oil-injected compressor. This model will be used to run simulation test cases to optimise the mode and amount of oil injection in Chapter 6.

Chapter 6 Improving Oil Distribution in an Oil-Injected Screw Compressor

6.1 Introduction

This chapter presents a study on the oil distribution within a screw compressor chamber using Computational Fluid Dynamics (CFD) with Volume of Fluid (VOF) multiphase model.

A body fitted structured numerical mesh was produced by the in-house software package SCORG and deformed in time with rotor rotation using user-defined nodal displacement for Ansys Fluent. The analysis was carried out on a newly designed screw compressor for Kirloskar Pneumatics Company Limited, which has a 4-5 lobe combination and a male rotor diameter of 98 mm. This compressor operates at discharge pressures of 8.5 bar and 10.5 bar and a rotor rotational speed of 6000 rpm.

Two test cases are analysed in this Chapter, i) the single-point injection with variation in oil injection nozzle diameter from 3 mm to 8mm and ii) the case with two injection ports positioned on each rotor at the appropriate oil injection angle. The analysis is focused on oil distribution and gas temperatures within the compression chamber close to rotor surfaces. The compressor performance parameters such as air flow rate, power, specific power, adiabatic efficiency, and volumetric efficiency are studied and compared for all test cases in order to understand the effect of different injection conditions.

6.2 Computational domain

The oil-injected compressor used for this study is specified in detail in Table 10 in section 5.2, Chapter 5. The original oil port position is on the female rotor at the male rotor angle rotation of 68.7°. The second oil injection port is located at the male rotor and at the same oil injection angle as the original injection port. The port positions are shown in Figure 46.

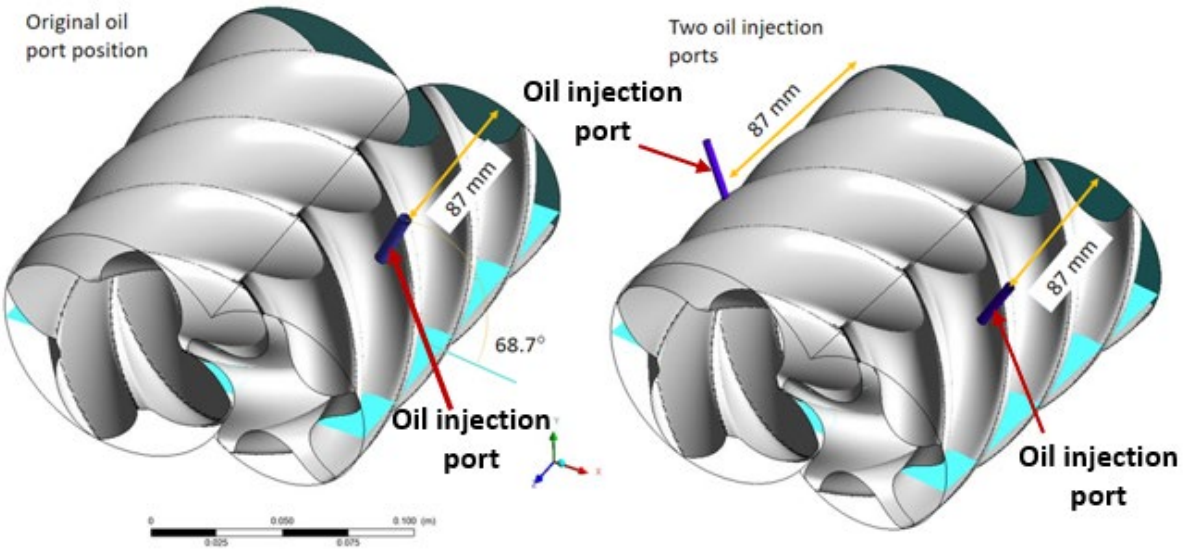

Figure 46. Positions of single and two oil injection ports.

For details for computational domain and numerical grids used for calculations in this chapter, please refer to section 5.3 of Chapter 5.

6.3 Case setup and preliminary results

The physical properties of air and oil are shown in Table 19. The inlet boundary condition is the fixed static pressure and temperature. For the outlet boundary, the static pressure and temperature are adopted. More details about the boundary conditions used and numerical setup are shown in Table 20 and Table 21. The under-relaxation factors for individual governing equations are shown in Table 22.

y+ in the domain was in the range of 0.5-62.0, and for this wide range of y+, a hybrid turbulence model like SST k- ω was suitable. The transient analysis was carried out with the constant time step of 2.778 x10^{-05} s. The simulation was run for 0.051-0.083s, which reflected in 20-33 full rotations of the male rotor depending upon the oil injection flow rate.

Table 19. Physical and thermal properties of air and oil phase.

Property	Air	Oil
Fluid type	Ideal gas	Constant ρ 950 kg/m^3
c_p [J/kg/K]	1004.4	1800
μ [kg/ms]	1.831×10^{-5}	0.08
δ [W/mK]	2.61×10^{-2}	0.18

Table 20. Boundary conditions used.

Parameters	Value
Air inlet pressure, P_{inlet} [bar]	0
Air inlet temperature, T_{in} [°C]	27
Oil inlet pressure, P_{oil} [bar]	8.5/10.5
Oil inlet temperature, T_{oil} [°C]	50
Outlet pressure, P_{outlet} [bar]	8.5/10.5
Heat flux for rotor, casing and port walls [W/m^2]	0

Table 21. Numerical simulation settings with Ansys Fluent.

Parameters	Settings
Gradient	Green-Gauss Node Based
Volume Fraction	Compressive
Turbulence Scheme	First-order upwind
Energy	First-order upwind
Transient Scheme	First-order implicit
Iterations per time step	100
Convergence Criteria	Continuity 0.001, Velocity 0.001, Energy 1e-06, Turbulence 0.001, Volume Fraction 0.001

Table 22. List of under-relaxation factors.

Variable	Value
Momentum	0.75
Pressure	0.75
Density	1.00
Body forces	1.00
Volume fraction	0.50
Turbulent kinetic energy	0.80
Specific dissipation rate	0.80
Turbulent viscosity	1.00
Energy	0.90

The mesh independence test was conducted, for the case study with the single oil injection port of 5mm diameter. The study included simulations on three different mesh sizes with a grid refinement ratio of 1.2. The summary of the results of this study is given in Table 23. The mass flow rate of air is regarded as an evaluation criterion calculated as an average of the mass flow rate of air at the inlet and outlet. The relative difference in the mass flow rate between grids 2 and 3 is 0.15%. Therefore, grid number 2, which consists of 924,120 elements, was used for further simulations of various case studies.

Table 23. Mesh independence study results.

Grid number	Number of elements-rotors	Total elements (rotor+ports)	$\dot{m}_{air}$ (kg/s)	Relative deviation (%)
1	761940	1,500,214	0.0722	1.8%
2	924120	1,662,394	0.0736	-
3	1074060	1,812,334	0.0735	-0.15%

The overview of case studies for the given injection port diameters is given in Table 24. Similar to the calculation for the mass flow rate of air, the mass flow rate of oil is calculated as an average of the inlet and outlet mass flow rate of oil. Also, indicated power is calculated based on the torque acting on both the male and female rotors. All case studies were carried out at a rotational speed of 6000 rpm.

Table 24. Simulated case studies.

	Single oil injection port		
d_{oil} [mm]	**$\dot{m}_{oil}/\dot{m}_{air}$**	**P_{out} [bar]**	**P_{oil} [bar]**
3	1.6	8.5	8.5
	1.8	10.5	10.5
4	3.2	8.5	8.5
	3.8	10.5	10.5
5	5.3	8.5	8.5
	6.3	10.5	10.5
8	15.3	8.5	8.5
	17.4	10.5	10.5
	Two oil injection ports		
d_{oil1}= 3.5 and d_{oil2}=	5.3	8.5	8.5
3.6, equivalent d_{oil}= 5	5.7	10.5	10.5

The cell-averaged discharge temperature (T_{dis}) obtained at a cross-section closer to the outlet with the progressing simulation time was used to check when the steady-state condition was achieved. The discharge temperature as a function of accumulated solution time is shown in Figure 47 for 8.5bar. For the 3mm oil injection port, nearly 0.0824 s of solution time was taken, whereas only 0.0518s were needed for the 8mm oil injection port. A similar check was made for the discharge pressure of 10.5bar.

Figure 48 shows that the oil flow rate increases linearly with the oil port diameter for both cases. The final mass imbalance for the air phase had an average value of 0.57% at 8.5bar and 0.30% at 10.5bar, while for the oil phase, it was 4% at 8.5bar and 2.3% at 10.5bar.

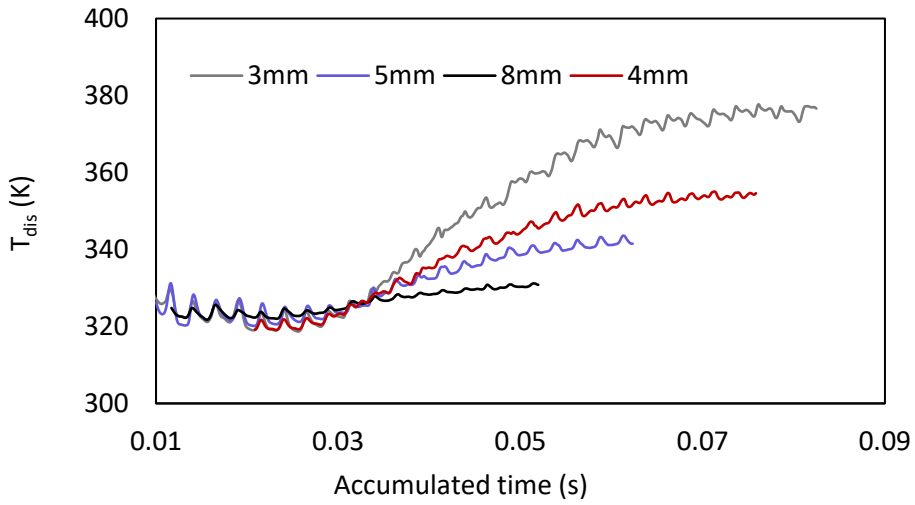

Figure 47. Discharge temperature at 8.5bar.

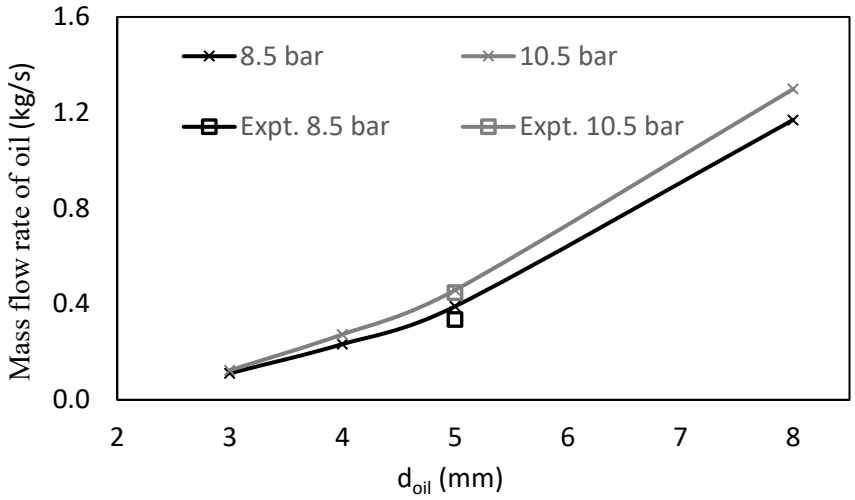

Figure 48. Averaged oil flow rate for different oil injection port diameter at 8.5 and 10.5bar.

6.4 Experimental results

The instrumentation, measurement points, measurement procedure, along with a layout of the test rig is described in section 5.5 in Chapter 5. In the same section, equations to obtain the compressor performance parameters of indicated power, air volume flow rate, volumetric efficiency, adiabatic efficiency and specific power from measurements are detailed.

The performance obtained for the tested oil-injected compressor at a pressure ratio of 8.5 bar and 10.5 bar at 6000 rpm is shown in Table 25. These results are obtained for the oil injection port diameter of 5mm.

Table 25. Test results obtained for a single oil injection port diameter of 5mm.

Pressure ratio P_2/P_1	**Indicated Power PW_i [kW]**	**Volume flow rate Q_v [m^3/min]**	**Volumetric efficiency η_v [%]**	**Adiabatic efficiency η_{ad} [%]**	**Specific Power w_{comp} [kW/m^3/min]**
8.5	20.7	3.73	85.6	75.3	6.53
10.5	22.9	3.67	84.2	76.6	7.35

6.5 Results and discussions

A total of ten cases at different oil injection conditions and two different pressure ratios are calculated. The distribution of oil and the temperature field in the cells near the rotor surface are illustrated and quantified in this section. Moreover, the performance parameters of the indicated power, air flow rate, volumetric efficiency, adiabatic efficiency, and specific power are recorded and compared between the calculated case studies and experimental data.

6.5.1 Oil injection through the single injection port

6.5.1.1 Oil and temperature distribution

Figure 49 shows the visualisation of the oil distribution in the compression domain using the VOF model at P_{out}=8.5 bar and the male rotor speed of 6000 rpm. These figures are presented at the same male rotor angle of 20º.

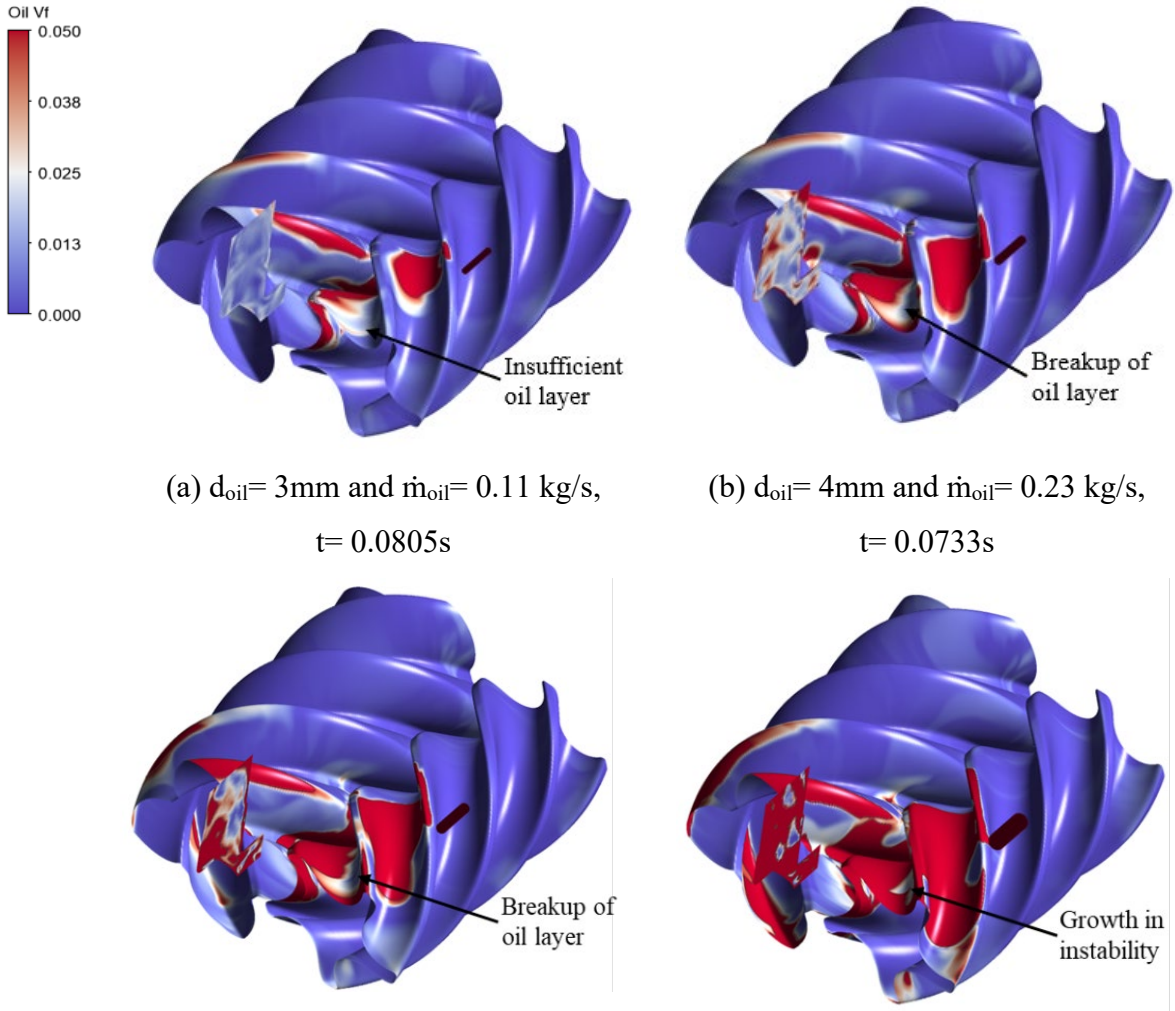

(a) d_{oil}= 3mm and $\dot{m}_{oil}$= 0.11 kg/s, t= 0.0805s

(b) d_{oil}= 4mm and $\dot{m}_{oil}$= 0.23 kg/s, t= 0.0733s

(c) d_{oil}= 5mm and $\dot{m}_{oil}$= 0.39 kg/s, t= 0.0733s

(d) d_{oil}= 8mm and $\dot{m}_{oil}$= 1.17 kg/s, t=0.0505s

Figure 49. Oil volume fraction in the first layer of cells adjacent to rotors at 6000 rpm and 8.5bar discharge pressure.

The oil distribution shown by the oil volume fraction and the gas temperature in the first layer of numerical fluid cells adjacent to the rotor surface is shown in Figure 49 a-d and Figure 51 a-d, respectively. As shown in Figure 49a and Figure 51a, the 3mm nozzle does not supply sufficient oil and the gas temperature locally reaches up to 220°C. At the same time, as shown in Figure 50, the discharge temperature exceeds 110°C. Figure 49b and Figure 49c show the spreading of the oil layer further on the female rotor surface with the oil nozzles of 4mm and 5mm. With the rotation of rotors, this layer shears and breaks, and it will reach the axial discharge clearance on the female rotor side. However, it could be observed that it does not spread on the male rotor as widely as on the female rotor. The discharge temperature is below 90°C for both cases, as shown in Figure 50. For the 4mm oil injection hole, the local gas

temperature on the female rotor leading tip exceeds 100°C, while for the 5mm oil injection, the female rotor side is well cooled. However, in both cases, the male rotor side experiences hot zones above 100°C with temperatures in some regions as high as 189°C for 4mm nozzle and around 157°C for 5mm nozzle.

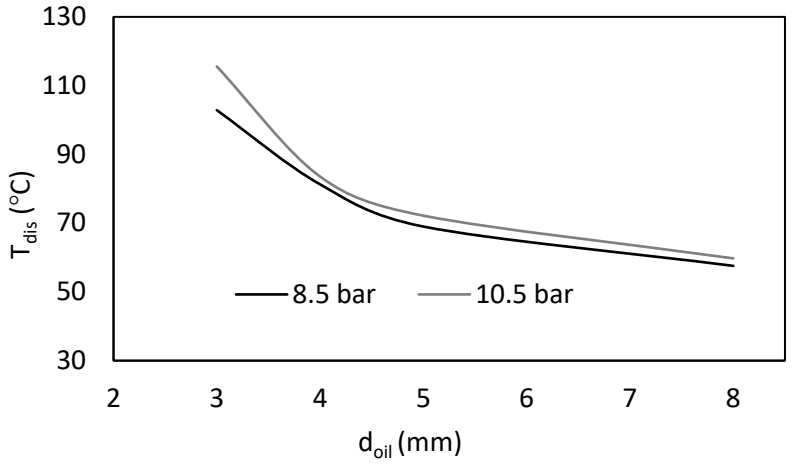

Figure 50. Discharge temperature as a function of the oil port diameter at 6000 rpm, 8.5 and 10.5bar discharge pressure

Further increase in the diameter of this single injection port will increase the oil flow in the compressor. Thus, changing the orifice from 5mm to 8mm increases the oil flow by a factor of 2.8 but results in a gas temperature reduction of only 11°C. The excess of oil does not contribute sufficiently to the cooling of the gas. The large oil content results in a very stable oil layer, as shown in Figure 49d. An important point to note is that, even with this highest oil mass flow rate of 1.17kg/s, the distribution of oil on the male rotor side remains sparse, and the temperature still exceeds 100°C in certain regions. This observation of high temperatures in the compression chamber is also with a 10.5 bar, as shown in Figure 52.

It can be concluded that, with the single oil injection port on the female rotor side, the oil layer sufficiently spreads on the female rotor side, but the oil does not spread effectively on the male rotor. Hence, the increase in the oil flow rate helps to reduce the gas discharge temperature, which drops down to 50°C, but the local temperature inside the domain on the male rotor side remains above 100°C. Moreover, the excessive amount of oil requires larger equipment in the compressor system and adversely affects the total efficiency of the compressor, and therefore it is not recommended as a method for optimisation of compressors.

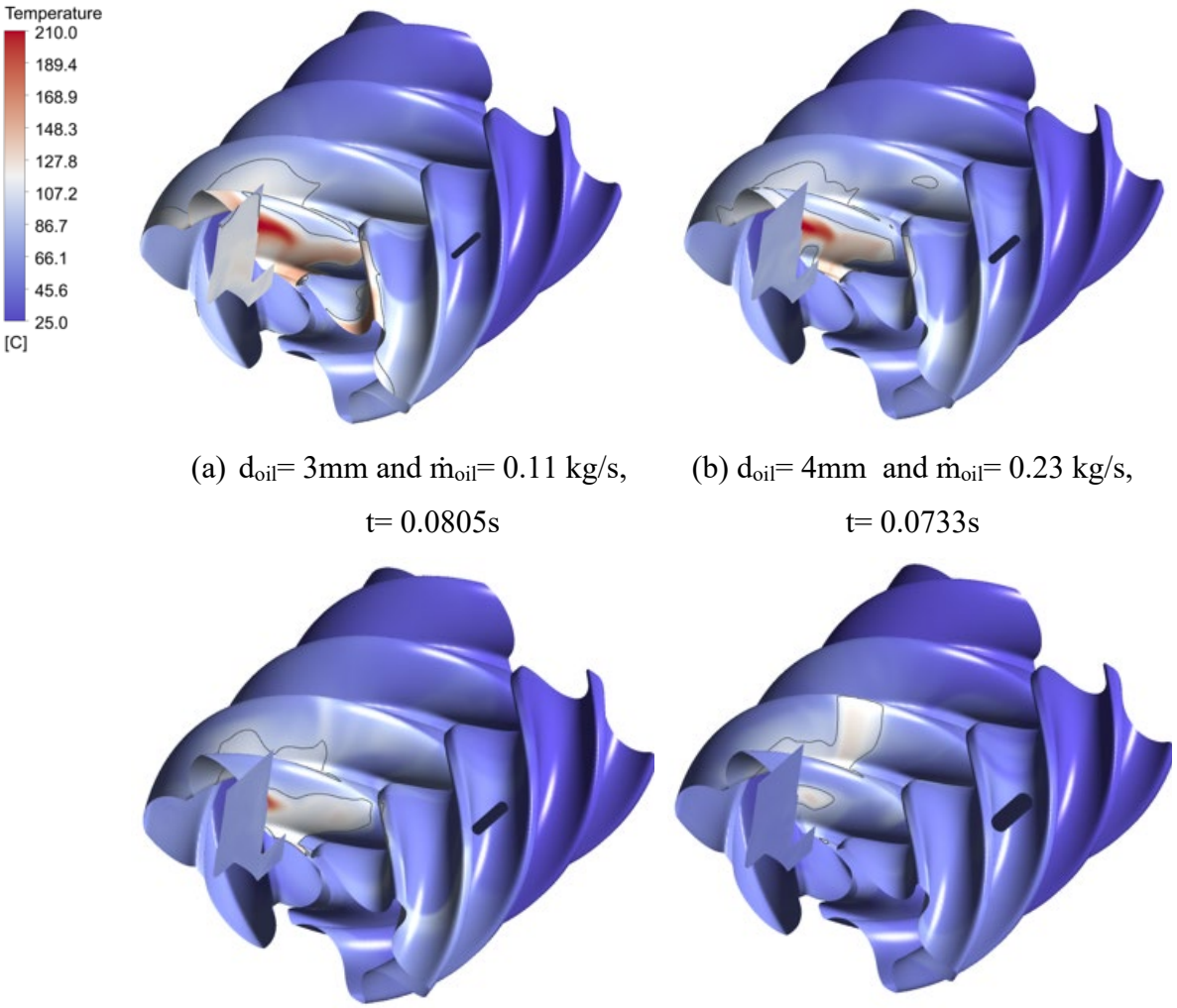

(a) d_{oil}= 3mm and $\dot{m}_{oil}$= 0.11 kg/s, t= 0.0805s

(b) d_{oil}= 4mm and $\dot{m}_{oil}$= 0.23 kg/s, t= 0.0733s

(b) d_{oil}= 5mm and $\dot{m}_{oil}$= 0.39 kg/s, t= 0.0733s

(d) d_{oil}= 8mm and $\dot{m}_{oil}$= 1.17 kg/s, t=0.0505s

Figure 51. Local gas temperature in the first layer of cells adjacent to rotors at 6000 rpm and 8.5bar discharge pressure. The regions bounded by the isolines represent areas where temperatures exceed 100°C.

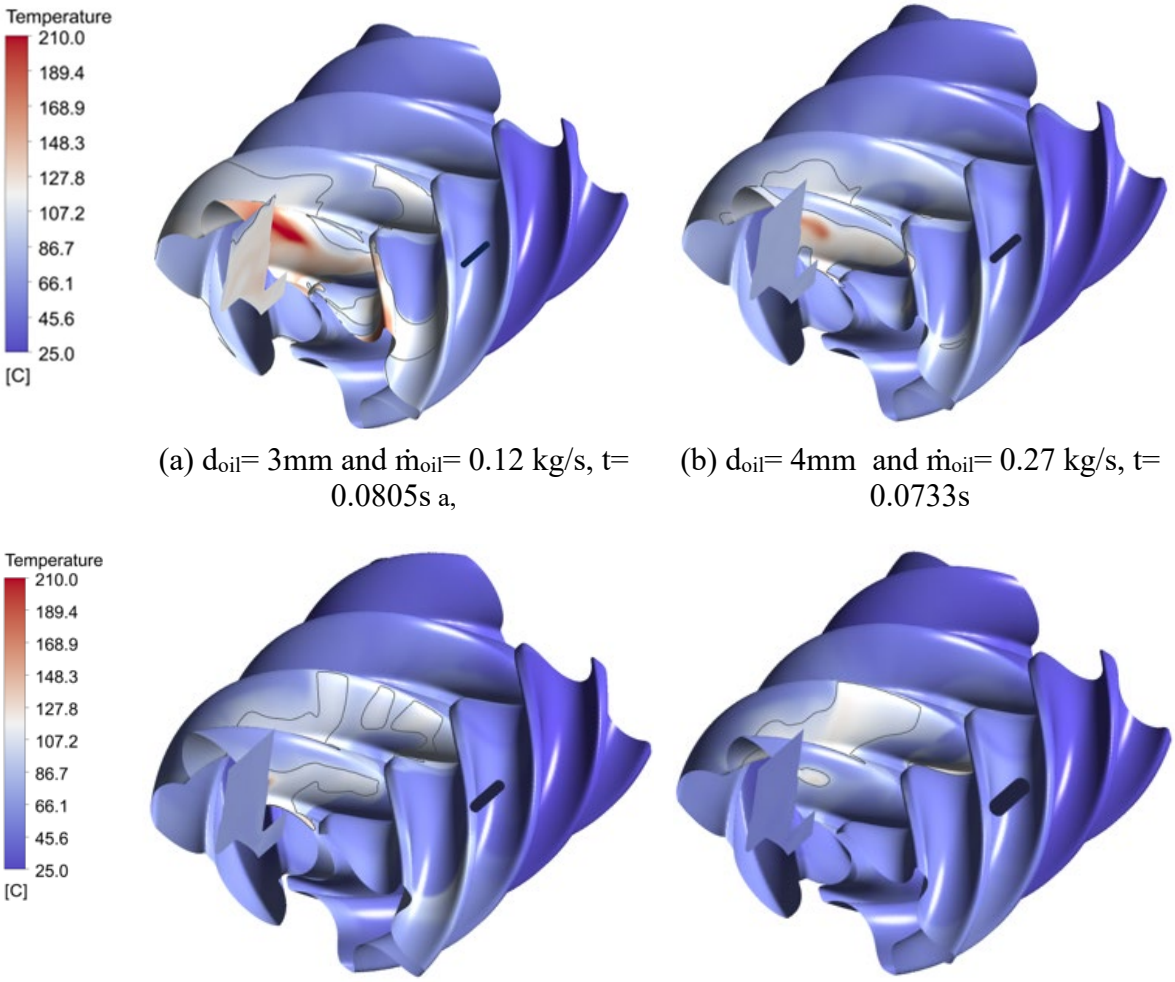

(a) d_{oil}= 3mm and $\dot{m}_{oil}$= 0.12 kg/s, t= 0.0805s a,

(b) d_{oil}= 4mm and $\dot{m}_{oil}$= 0.27 kg/s, t= 0.0733s

(c) d_{oil}= 5mm and $\dot{m}_{oil}$= 0.45 kg/s, t= 0.0733s

(d) d_{oil}= 8mm and $\dot{m}_{oil}$= 1.30 kg/s, t=0.0505s

Figure 52. Local gas temperature in the first layer of cells adjacent to rotors at 6000 rpm and 10.5bar discharge pressure. The regions bounded by the isolines represent areas where temperatures exceed 100°C.

Bar plots shown in Figure 53 represent the oil volume fraction and temperature versus the percentage of rotor surface areas where these values apply. The majority of the rotor surface area is covered with a very low oil volume fraction between 0.0-0.1 and therefore not included in the figure. The same applies to surfaces areas with low temperatures. The value of the oil volume fraction and temperature is from the cells near the rotor surface.

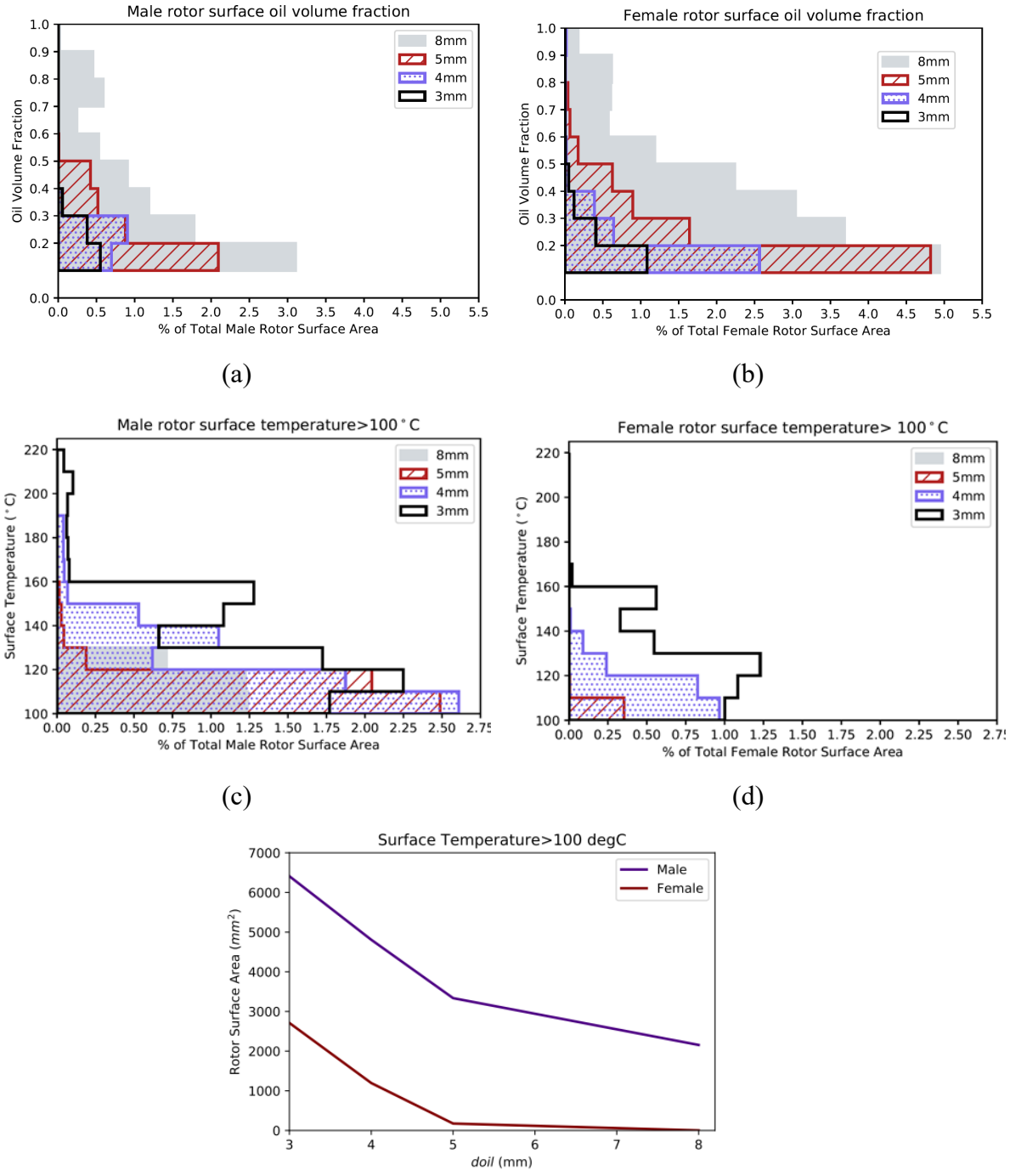

Figure 53. Distribution of oil and temperatures of air on the male and female rotors shown as the percentage of the rotor surface.

The total surface area of the male rotor is 70,947mm^{2,} and for the female rotor, it is 58,263mm^2.

Changing the oil injection port diameter from 3mm to 8mm increases the mass flow rate of oil 9.5 times, but the total surface area wetted by oil increases only 5.5 times. Moreover, by injecting oil through a single injection point on the female rotor side, the oil flooded female rotor surface is 1.7 times higher than the oil flooded male rotor surface. This disparity between the male and female rotor sides is shown in Figure 53a and Figure 53b. This results in fluid temperatures beyond 100°C to cover much larger rotor surface areas on the male rotor than on the female, as shown in Figure 53c and Figure 53d. It is important to notice here that the percentage of the rotor surface area in contact with oil is relatively small compared to the total rotor surface, which is also visible in previous figures.

To appreciate the significance of the surface temperatures close to rotors, the total surface areas with temperatures higher than 100°C, are summed up for various oil injection diameters in Figure 53e, where a large difference between the surface areas with high temperatures on the male and female rotors can be observed, thus emphasising the need for better distribution of the oil to transfer the heat more evenly.

6.5.1.2 Effect on the compressor performance

The comparison between the performance predicted from CFD calculations and the performance measured in the test rig is shown in Figure 54. The difference for the air flow rate is 0.5% at 8.5bar and 0.7% at 10.5bar, while the difference for power is around 3.0% at 8.5bar and 2.3% at 10.5bar. This upholds the confidence in the reliability of CFD predictions.

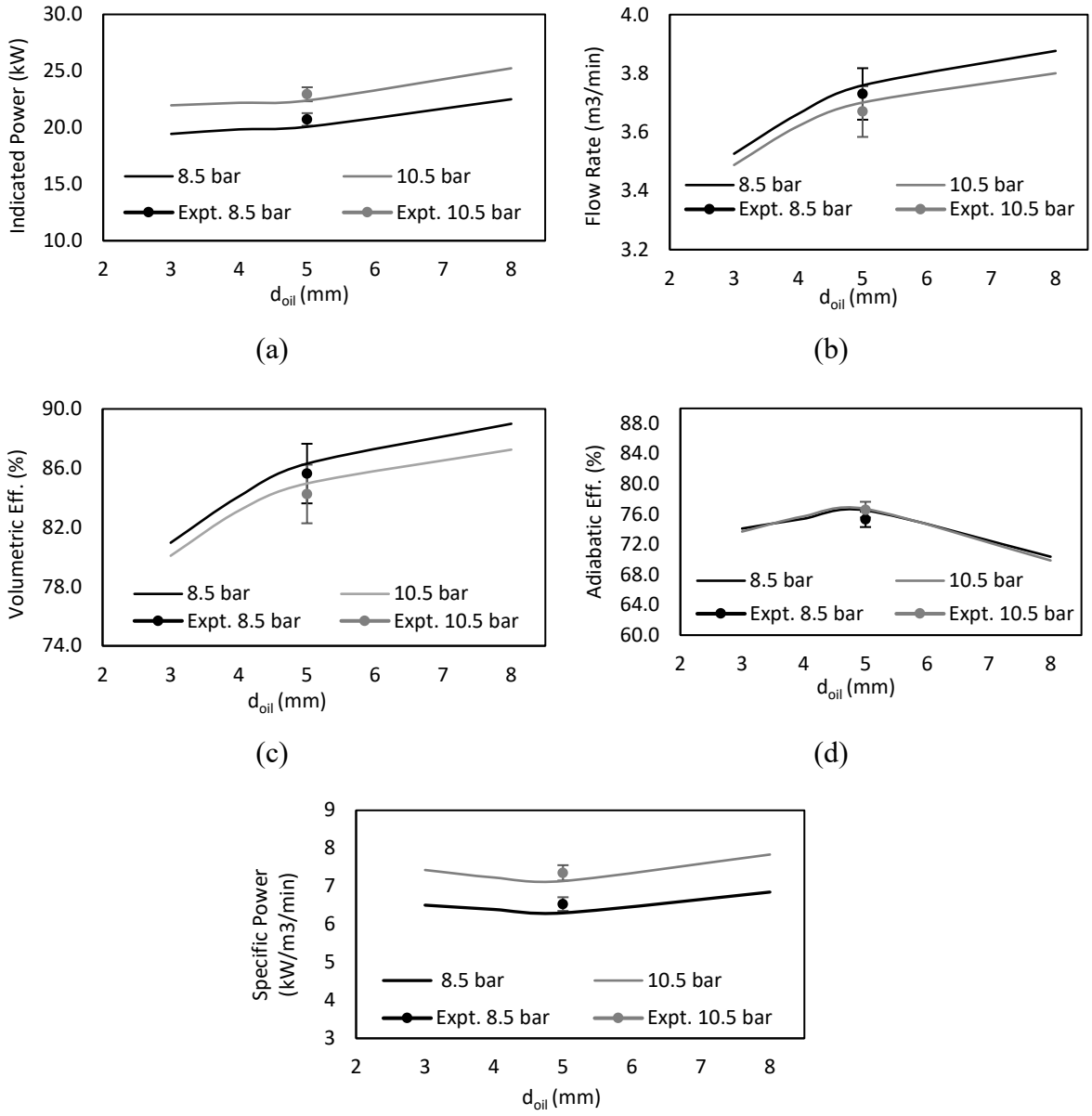

Figure 54. (a) indicated power, (b) air flow rate, (c) volumetric efficiency, (d) adiabatic efficiency and (e) specific power and with oil port diameter for discharge pressure of 8.5bar and 10.5bar

Based on these predictions and measurements, the next section presents the investigation on improvements in rotor cooling and specific power using a separate injection port on each rotor side.

6.5.2 Oil injection through two injection ports

The CFD analysis of this oil-injected screw compressor with oil injection through the single port showed the uneven distribution of oil on the female and male rotors that caused the excessive gas temperature in the male rotor domain. It was suggested that design alterations are required to reduce the internal gas temperature. An additional oil injection port was added in the casing on the male rotor side to resolve this. The cumulative oil flow rate from the two injection ports is made equal to the optimum oil flow rate calculated for the single injection port, and the port is positioned to match the injection angle similar to the female rotor.

The single-port oil injection selected for this comparative study had a diameter of 5mm with an oil flow rate of 0.39kg/s and 0.46kg/s at 8.5bar and 10.5bar compressor discharge pressures, respectively. The diameters of both injection ports were 3.6mm for the female rotor and 3.5mm for the male rotor, as shown in Figure 55. This resulted in a total oil flow rate from both ports being 0.35kg/s, and 0.41kg/s at 8.5bar and 10.5bar, respectively. This, on average, resulted in a 9.7% lower total flow rate. The calculated oil flow rates are shown in Table 24. Better matching could not be achieved because the second decimal accuracy would be required in the sizing of orifices, and this would be impractical to manufacture. Also, each nozzle's pressure difference would not be the same due to the difference in their positioning.

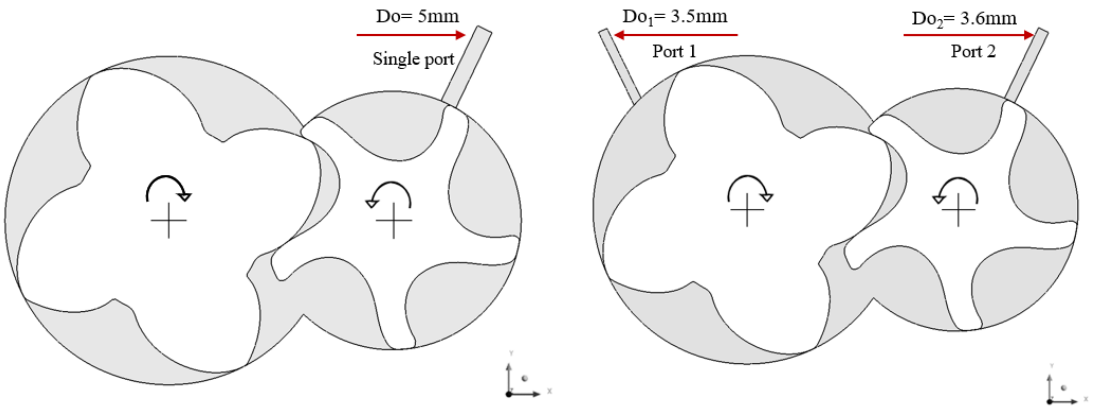

Figure 55. Oil-injection port on the rotor (cross-section at z= 0.1m) Left: single port on the female rotor side and Right: dual port on the male and female rotor side.

6.5.2.1 Oil distribution and temperatures for two-point oil injection

The CFD calculation results for the single injection port and two injection ports are presented in Figure 56, showing the oil distribution, and in Figure 57, the temperature of the fluid next to the compressor rotors. Both are at the discharge pressure of 8.5bar and the male rotor rotational angle of 30°.

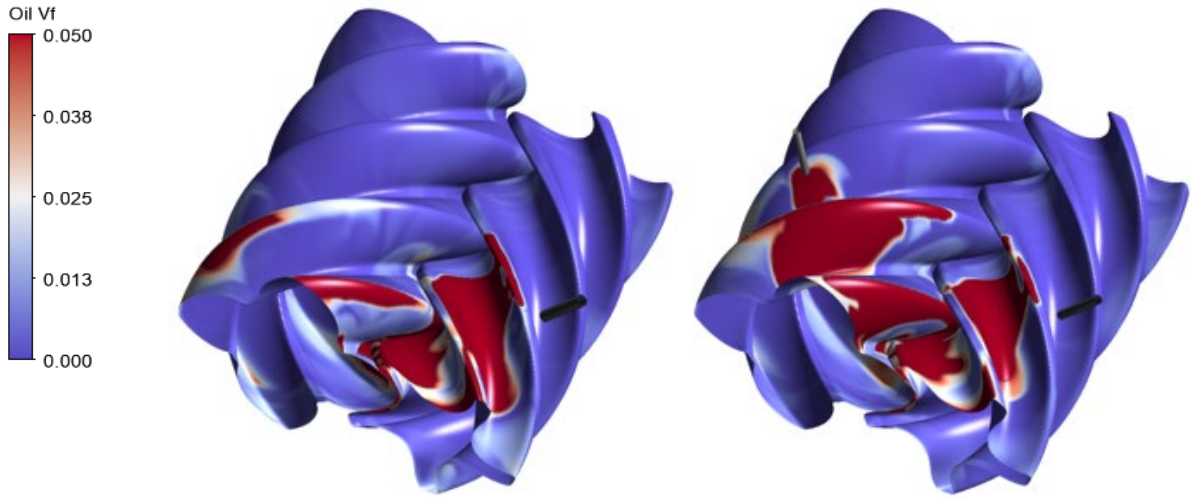

Single Injection Port Two injection Ports

P_{out}= 8.5bar at t= 0.0733s

Figure 56. Comparison of oil distribution for the single injection port and the two-injection port.

Looking at the left Figure 56, where oil is injected through the single port, most oil flow is directed towards the outlet through the working domain associated with the female rotor. Some oil is directed towards the male rotor tips due to inertial forces. This is beneficial for sealing the radial clearance gaps, but the amount of oil in the working chamber is very low. This poor oil distribution results in high temperatures of air between the male rotor lobes. Figure 57 shows that the temperature in this region well exceeds 100°C reaching up to 157ºC.

By injecting oil through two injection ports, one on the male and another on the female rotor, the distribution of oil in the working chamber on the male rotor side improved significantly. As shown in Figure 57, the area in which the temperature exceeds 100°C is significantly reduced, and the maximum temperature is reduced to 127°C.

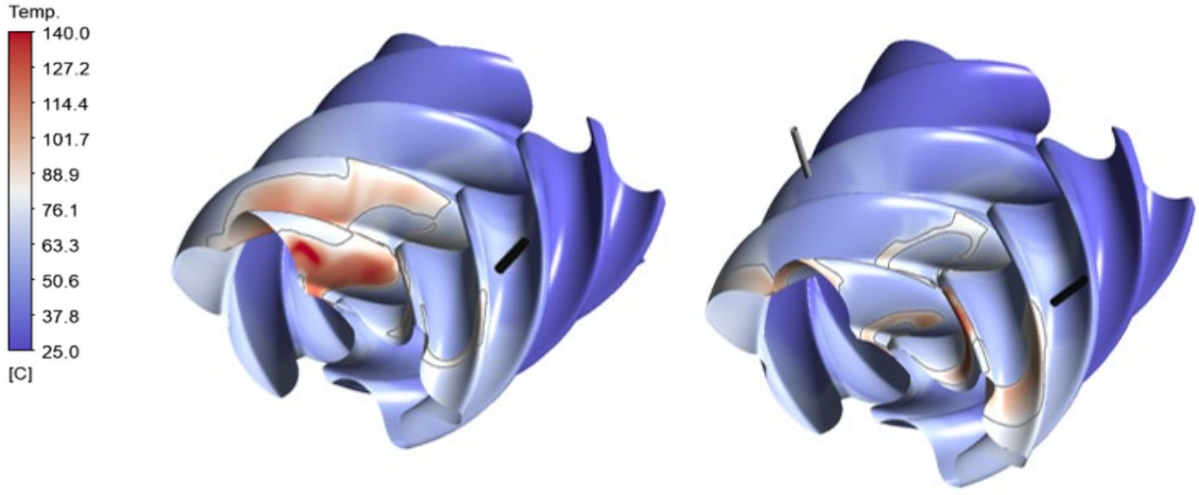

Single Injection Port Two injection Ports

P_{out}= 8.5bar at t= 0.0733s

Figure 57. Comparison of the gas temperatures for the single injection port and the two-injection port.

To further appreciate the differences in oil distribution between the single oil injection port and two injection ports, plots for the oil volume distribution on rotor surfaces are shown in Figure 58 and Figure 59. Here the rotor surface area is the surface area of the cells containing certain values of oil volume fraction and temperatures. These bar plots show that separate injection to each rotor clearly reduces the wetted female rotor region area and supplements an increase in the wetted area near the male rotor region. It can be seen from Figure 60 and Figure 61 that the use of two injection ports drastically alters the local temperatures. Both are at the discharge pressure of 8.5bar.

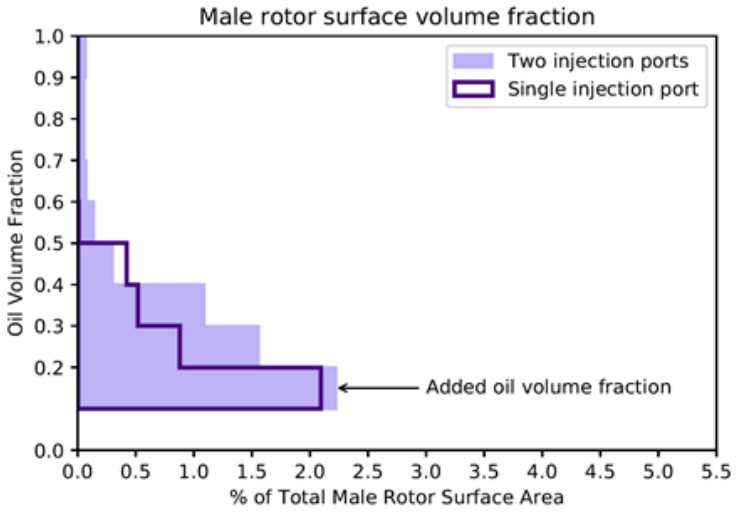

Figure 58. Rotor surface area with oil volume fraction on the male rotor for 8.5 discharge pressure.

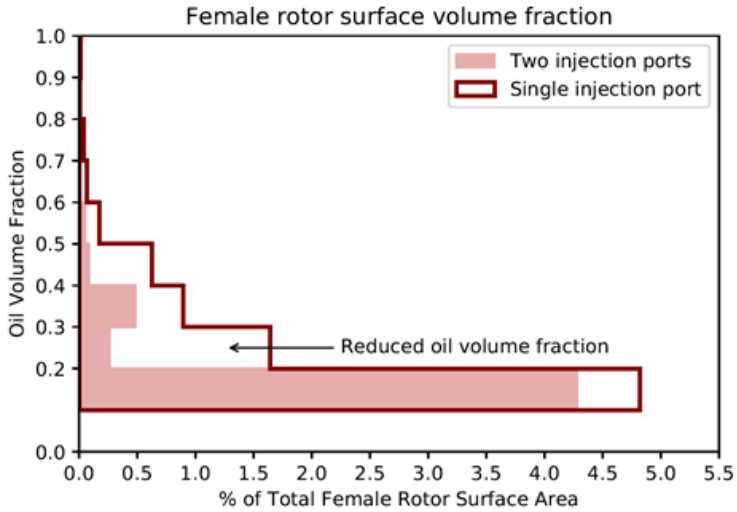

Figure 59. Rotor surface area with oil volume fraction on the female rotor for 8.5 discharge pressure.

To improve visualisation, rotor surface areas are shown for face temperatures beyond 90°C at 8.5bar and 10.5bar in Figure 60 and Figure 61. The percentage of rotor surface areas with high temperatures on the male rotor is significantly reduced with the two injection ports.

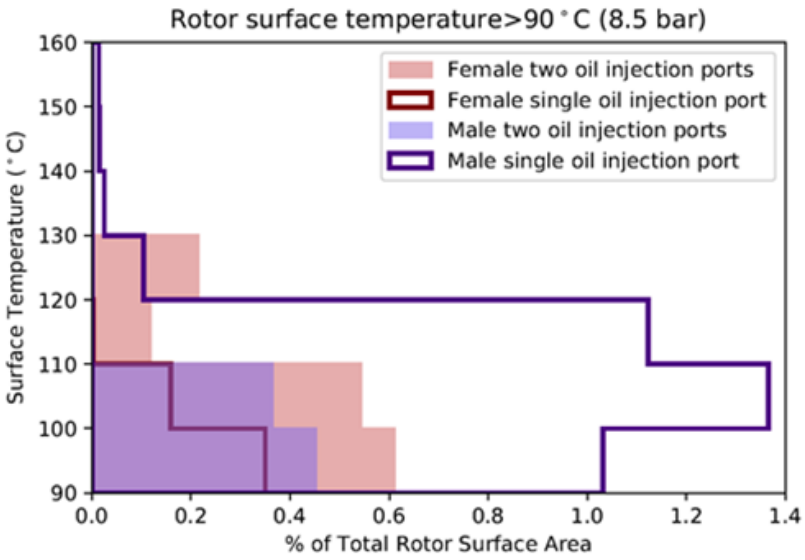

Figure 60. Rotor surface area with surface temperatures over 90°C on both rotors at 8.5bar.

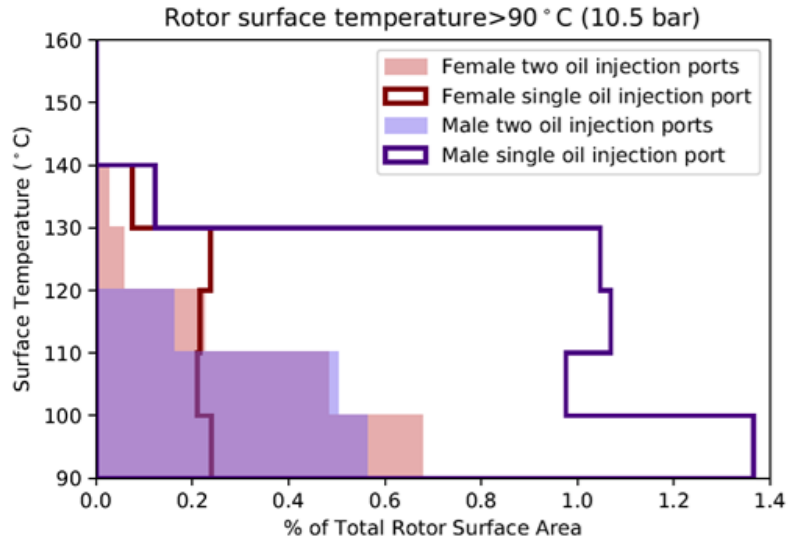

Figure 61. Rotor surface area with surface temperatures over 90°C on both rotors at 10.5bar.

As shown in Table 26, the oil injection through two ports led to the reduction in maximum temperatures of 30 °C at 8.5bar and 35 °C at 10.5bar.

Table 26. Maximum temperature reduction by introducing two injection ports

Injection Type	T_{max} [°C]	
	P_{out}: 8.5bar	**P_{out}: 10.5bar**
Single injection port	157	150
Two injection ports	127	115
ΔT	30	35

6.5.2.2 Effect on the compressor performance

Performance improvements due to the use of two oil injection ports are shown in Figure 62. The addition of the second port did not influence the air flow rate. At the same time, the oil flow rate was reduced by 9%. The main effect on the performance was a reduction in power consumption for the two injection ports. Indicated power reduced by 2.1% and 1.8% for 8.5bar and 10.5bar discharge pressure, respectively. This combined effect of flow and power reduced specific power by around 1.8% for both 8.5and 10.5bar discharge pressures.

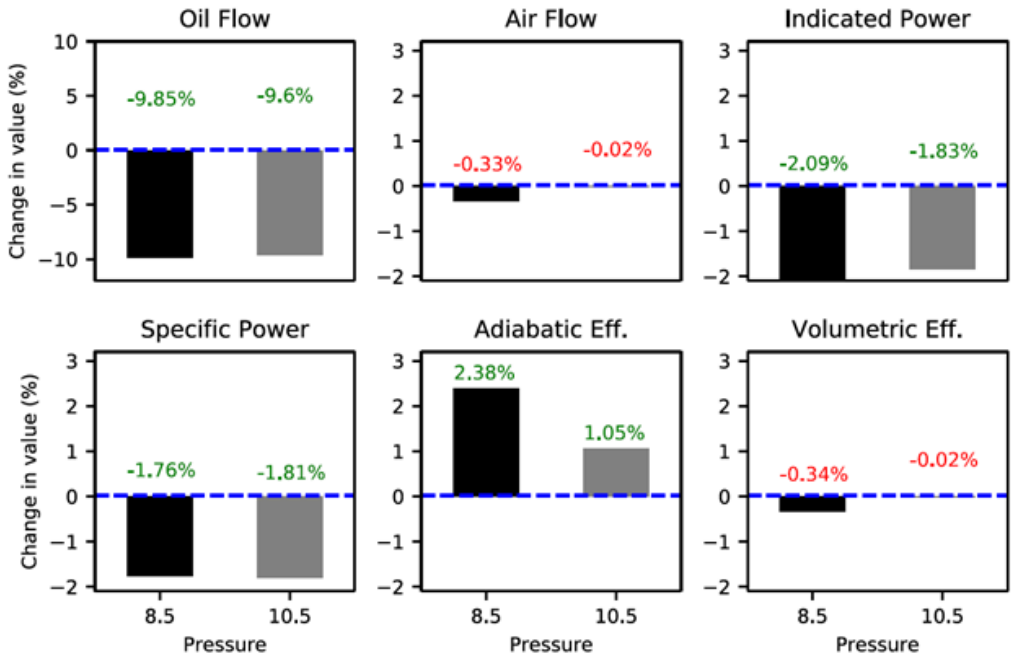

Figure 62. Comparison of the two injection ports and the single oil-injection port configurations at discharge pressures of 8.5 and 10.5bar. The green coloured text indicates improvement levels with the two-port configuration.

6.6 Summary

CFD analysis of the fluid flow and temperature distribution within the oil-injected twin screw air compressor with the VOF multiphase model was used to evaluate improvements by introducing a two-point oil injection. This was carried out for the compressor with the 4/5 lobe combination, operating at the male rotor shaft speed of 6000 rpm at discharge pressures of 8.5 and 10.5bar. The predicted results of the single injection port were compared with the results obtained by measuring this compressor. Both power and flow predictions were close to experimental results with differences of 0.5% for flow and 3% for power, respectively, at 8.5bar and 0.7% for flow and 2.3% for power at 10.5bar.

The model was used to evaluate both oil and temperature distribution and performance of the compressor with the single oil injection port located in the casing close to the female rotor and with the two injection ports injecting to both male and female rotors. The total injection flow was retained in both cases by adjusting the size of the oil injection ports. The key conclusions from this study are:

- This computational procedure produced results in good agreement with measurements.
- This analysis method enabled both the oil and temperature distribution to be evaluated within the compression chamber and to visualise how the oil layer was formed and broke up close to the rotor surfaces.
- It was concluded that the temperature of the gas at rotor surfaces was determined by the oil distribution and that hot spots were found to coincide with regions where oil concentration was low.
- By increasing the orifice diameter of the single injection port, it was possible to reduce the air discharge temperature, but, despite this, it was found out that there was an optimum value for the oil injection rate, beyond which there was no significant gain in the internal cooling of the gas.
- With the single oil injection hole on the female side, the temperature in the compression chamber on the male rotor reached 157°C, although temperatures on the female rotor side were far lower. It was therefore decided to determine whether the maximum surface temperatures could be reduced by oil injection into both the male and female rotor sides of the casing.

The study showed that with two injection ports and the same total oil injection flow rate, the predicted indicated power was reduced by 2.1% and 1.8% at 8.5bar and 10.5bar, respectively.

The specific power was reduced by 1.8% in both cases, while the maximum internal temperature with the oil injection holes on both rotor sides was reduced to 127°C, which was an improvement of 30-35°C.

Chapter 7 Numerical Analysis of the Oil Breakup and Droplets Size in the Simplified Compressor Domain

7.1 Introduction

Chapter 6 revealed that by decreasing compression chamber temperatures, the oil-injected compressor's efficiency could be improved by a small percentage. The reduced temperatures were achieved using two injection ports on each rotor side, promoting better oil distribution than with a single oil injection port with the same amount of oil. Another way of limiting compression chamber temperature is by reducing the oil droplet size. It was observed through the literature review that the small oil droplet sizes enhance the heat exchange area between gas and oil, which reduces the gas temperature. The size of oil droplets depends on the breakup of oil. Determining the breakup mechanism and size of droplets is the focus of this chapter.

Firstly, the dominant atomising mechanism, which leads to a small oil droplet size in a twin-screw compressor, is discussed in this chapter. Based on this, a simplified compression domain is constructed for analysis. The main part of the chapter is studying the oil transition into various breakup structures that finally result in droplets. This was performed through the VOF model with adaptive mesh refinement in Ansys Fluent solver that follows an equidistributional adaptation technique where the cells are divided in equal distances.

The analysis focuses on the radial gap region filled with oil. Oil from this region accelerates towards the compression pockets. The simplified domain consists of a rectangular rotor profile with a differential pressure of 1.5 bar across the leakage gap. The rotor has a rotational speed of 6000 rpm, which corresponds to the tip velocity of 22 m/s. The simulation is performed on the stationary mesh with the velocity applied to the wall.

The simulation is firstly run without any adaptive mesh refinement and then with the adaptive mesh refinement based on the oil volume fraction gradient. This is done to show the effect of the dynamic adapting of the mesh so that the oil breakup features can be captured.

Overall, the formation and disintegration of the oil film into primary and secondary breakup structures in a transient case is studied here.

7.2 Problem formulation

The cross-sectional planes for an oil-injected compressor from Chapter 6 are shown in Figure 63. This figure shows the contour of oil volume fraction obtained through VOF modelling at the position of oil injection and oil entrainment through the leakage gap. Due to the high inertia of oil near the injection and leakage regions, it is expected that the oil will undergo disintegration resulting in droplets.

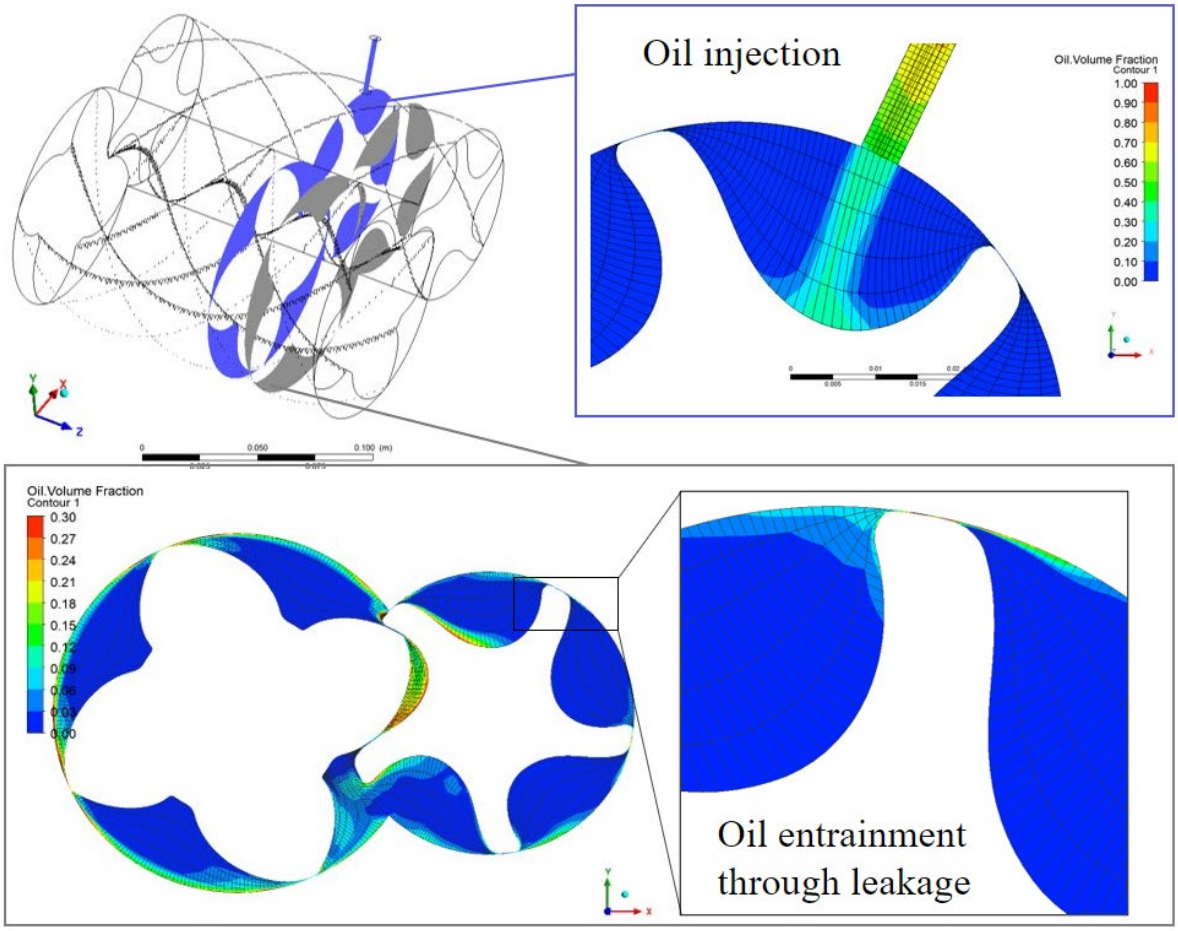

Figure 63. Oil volume fraction on a cross-sectional plane in the twin-screw compressor at injection and leakage regions.

The literature shows that the Sauter mean diameter (SMD) of oil can be estimated at the injection points using semi-empirical models. Out of the various semi-empirical models, the Harmon model showed predictions closer to experimental data in the literature [87] (more details in section 2.2.3).

Hence, Harmon's model is used to estimate the oil Sauter mean diameter for oil injection conditions in an industrial oil-injected compressor described in Chapter 6 (Table 21). The physical properties of oil, injection conditions and the injection port diameter are used to calculate Weber number and Sauter mean diameter (details on calculation in Section 2.2.1 and Section 2.2.3). These injection conditions with the injection port diameters and the resulting Weber number and SMD are shown in Table 27.

Table 27. Oil Sauter mean diameter estimation for oil injection conditions in an oil-injected compressor based on Harmon's semi-empirical model.

Injection pressure [bar]	**Injection port diameter [mm]**	**Mass flow rate of oil [kg/s]**	**Weber number**	**Estimated Sauter mean diameter [mm]**
8.5	5	0.39	87	3.9
10.5	5	0.46	113	3.5

The calculated SMD with Harmon's model for injection pressure of 8.5 bar and 10.5 bar is 3.9 mm and 3.5 mm, respectively. These calculated values at the oil injection opening are at least 10 times higher than the SMD of 300-400 μm, which was measured at the discharge of the oil-injected twin-screw compressor in the literature [36]. Though the semi-empirical models might not capture the actual droplet sizes at the injection of the screw compressor, it also expected that the clearances in the compression chamber might be the mechanisms behind the resulting micron level sizes. Therefore, the disintegration of oil when it passes through the leakage gaps is investigated through CFD to check if the oil breaks up to form micron level droplet sizes. The semi-empirical models will not be used further for comparison with the CFD predictions, nor any form of fitting will be done to improve these models as it is beyond the scope of this thesis.

In order to computationally capture the transient oil breakup across various scales, the computational cell sizes in the domain should be comparable to the oil droplet size. This is always not possible without massively increasing the computational load. Therefore, additional formulations such as adaptive mesh refinement can be used with the VOF model to suitably capture the oil breakup. Having said that, there are challenges to applying adaptive mesh refinement directly to a mesh generated from the SCORG software package for a complete twin-screw compressor. For a twin-screw compressor in Ansys Fluent, mesh node positions

are updated with time step according to the rotor rotations (more details in Chapter 4). Different mesh and adaptive mesh refinement techniques need to function in a synchronised manner to work with this dynamically deforming mesh for each time step. Some special developments will be needed for this purpose which is not the focus of this thesis. Rather, the focus is on oil disintegration through leakage gaps and the resulting oil droplet size.

Therefore, a simple domain is constructed where mesh refinement during the pre-processing and the calculation stage can be easily achieved. This will help in effectively studying the breakup and formation of oil droplets in the compression domain.

7.3 Computational domain and mesh

A simplified domain is constructed with a rectangular rotor profile in a simple circular rotating frame. The radial clearance is set to 100µm. The real female rotor profile shown in Figure 64 is simplified, as shown in Figure 65. Here, the study concerning oil film formation and disintegration when oil enters through the leakage gaps will mainly depend on the clearance height, forces acting on the oil and air in the domain, and the fluid's physical properties. A simplified computational domain shown in Figure 65 captures the major geometrical features of a rotor in a casing. Thus, it is a reasonable estimation of a female rotor tooth in this case, provided the applied boundary conditions are similar to the twin-screw machines.

The geometrical characteristics of the three-dimensional computational domain are presented in Table 28.

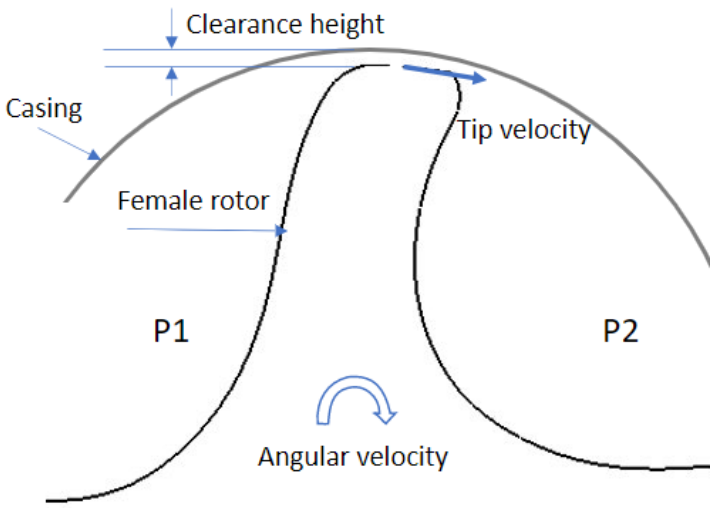

Figure 64. Computational domain with a female rotor in a casing.

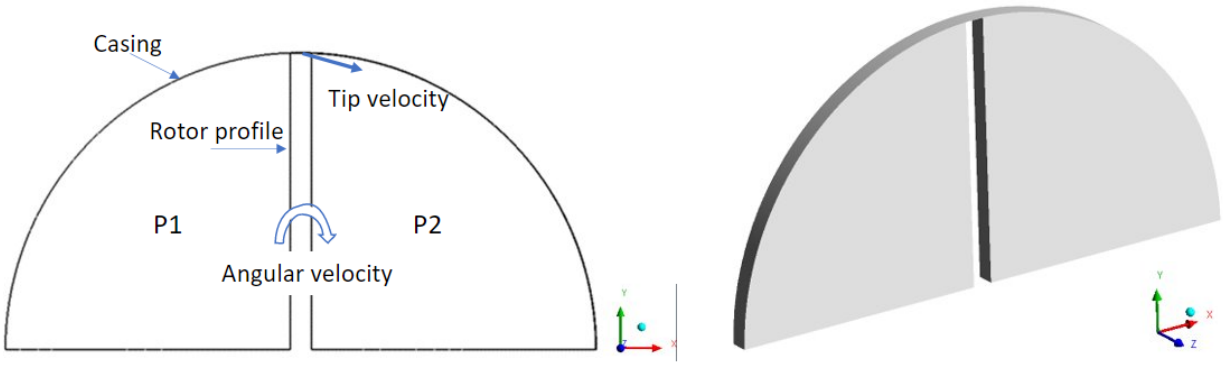

Figure 65. Simplified computational domain.

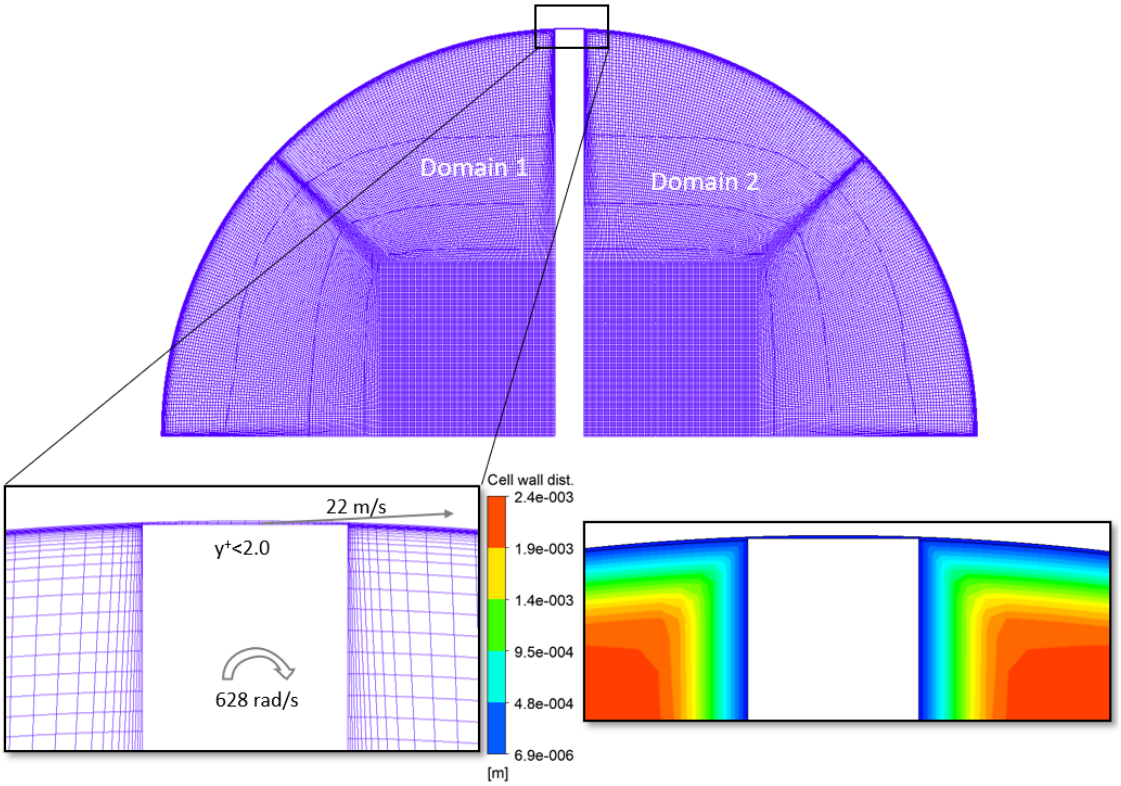

Figure 66. Refined cell layers in the base mesh of the simplified fluid domain.

Table 28. Geometric characteristics of the computational domain.

Parameter	Value
Casing radius [mm]	70.0
Rectangular profile height [mm]	69.9
Rectangular profile length [mm]	5.0
Rectangular profile thickness [mm]	15.0

A mesh with hexahedral cells for the simplified domain was generated through the Ansys Mesher software package. The meshed domain with wall refinement is shown in Figure 66. The first layer cell height is kept 0.0069 mm throughout the casing wall, so the thin oil film near the casing walls can be captured. The total number of cells in the mesh, which can be referred to as 'base mesh', is 1.1 million and the cells are expected to increase in number with adaptive mesh refinement.

7.4 Case setup

Air and oil are the working fluid. Air follows the ideal gas law, and oil has a constant density of 950 kg/m^3. The dynamic viscosity of air is 1.831x10^{-5} kg/ms, and oil is 0.08 kg/ms, respectively.

The following simplifications with the boundary conditions are followed to keep the flow properties similar to the screw compressor whilst reducing the computational load. These are, (i) the angular velocity and the tip velocity are imposed on the rectangular profile walls to replicate the effect of rotor rotation as in this case the domain remains stationary (momentum is imparted to the oil phase through rotational velocity acting in the domain and rotor tip velocity) (ii) the pressure in the domain is initialised rather than developed with the change in fluid volume (iii) oil is initialised in the leakage gaps and (iv) the domain operates under adiabatic conditions.

The initial and boundary conditions with values are presented in Table 29.

Table 29. Initial and boundary conditions used.

Parameter	Regions	Value
Angular velocity [rpm]	Rotor profile walls	6000
Tip velocity [m/s]	Rotor profile tip	22 m/s
Pressure, P_1 [bar]	Domain 1	7.5
Pressure, P_2 [bar]	Domain 2	6.0

The oil (phase 2) is initialised in the leakage gap with oil volume fraction as 1, shown in Figure 67. The differential pressure (P1 and P2), the angular and tip velocity help in oil entrainment towards the domain 2 region.

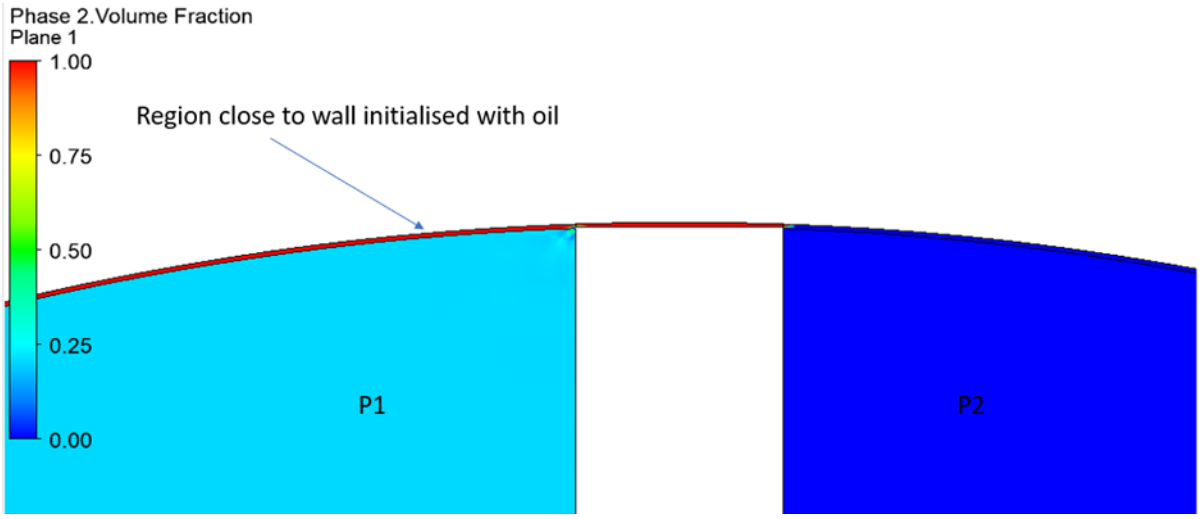

Figure 67. Initialisation of oil volume fraction in the clearance.

Table 30 shows the main solver settings applied in this study. The settings related to the adaptive mesh refinement will be explained in section 7.4.1. The pressure-velocity coupling scheme chosen here is SIMPLE as the published literature for the modelling of sprays had applied SIMPLE scheme for a faster solution [104]. The under-relaxation factors for the individual governing equation are shown in Table 31.

The Geo-Reconstruct scheme, along with explicit advection of the interface, is used for transient modelling of the air-oil interface. This scheme is shown to represent well the air-liquid interface in the literature [63]. More details on interface reconstruction schemes are explained in Appendix 3.2.

Also, nearly 97% of the computational domain cells show $y^{+}<5.0$, for which the SST k-omega model is suitable. Finally, the time step size is set as $1x10^{-06}$ to maintain a Courant number value of 2.

Table 30. Numerical simulation settings with Ansys Fluent.

Parameters	Settings
Volume fraction formulation	Explicit
Turbulence Model	SST k-omega (Mixture)
Pressure-Velocity Coupling	SIMPLE
Gradient	Green-Gauss Node Based
Pressure	PRESTO
Volume Fraction	Geo-Reconstruct
Turbulence Scheme	First order upwind
Energy	First order upwind
Transient Scheme	First order implicit
Iterations per time step	50
Time step size	$1x10^{-06}$
Convergence Criteria	Continuity 0.001, Velocity 0.001, Energy 1e-06, Turbulence 0.001, Volume Fraction 0.001

Table 31. List of under-relaxation factors.

Variable	Value
Momentum	0.5
Pressure	0.4
Density	0.5
Body forces	0.5
Volume fraction	0.5
Turbulent kinetic energy	0.5
Specific dissipation rate	0.5
Turbulent viscosity	0.5
Energy	0.8

7.4.1 With adaptive mesh refinement

Adaptive Mesh Refinement (AMR) is explored to resolve oil break-up better and minimise the air-oil interface's numerical diffusion. Adaption can be performed in Ansys Fluent during the transient calculations [108]. The mesh shown in Figure 66 is the initial mesh, and the adaption is performed on this mesh based on the numerical solution of oil volume fraction in the cells.

The adaptation process is separated into two distinct tasks: first, the individual cells are marked, then the selected cells are refined or coarsened based on the adaptation criteria. The cell adaption criteria are shown in Table 32. For this case, a second derivative of the oil volume fraction in a cell chosen for cell adaption [108]. If the second derivative of oil volume fraction in a cell is greater than $1x10^{-10}$ (equivalent oil droplet diameter for this volume is 568 μm), then these cells are marked for refinement and isotropically sub-divided into a number of cells depending on the refinement level. Also, if the second derivative of oil volume fraction in the refined cells is lower than $1x10^{-14}$, then these cells are coarsened or unrefined. However, the cells cannot be coarsened beyond the size of cells in the initial mesh.

Additionally, the refined cells cannot go smaller beyond the set limit of $1x10^{-14}$ m^3 (equivalent oil droplet diameter for this volume is 9 μm, and droplet size below 9 μm is not expected). The values for refinement and coarsen thresholds are a realistic expectation range of oil droplets diameters or volumes. The adaptation procedure is conducted for every 10 time steps as in the simulation of sprays in the literature using Ansys Fluent due to the balance between solution time and observed breakup features [104]. The same is considered here for the sake of ease.

Table 32. Adaptation criteria.

Parameter	Settings
Adaptation time step interval	10
Second derivative oil volume fraction: Coarsen threshold	$1x10^{-14}$
Second derivate oil volume fraction: Refinement threshold	$1x10^{-10}$
Minimum cell volume [m^3]	$1x10^{-14}$

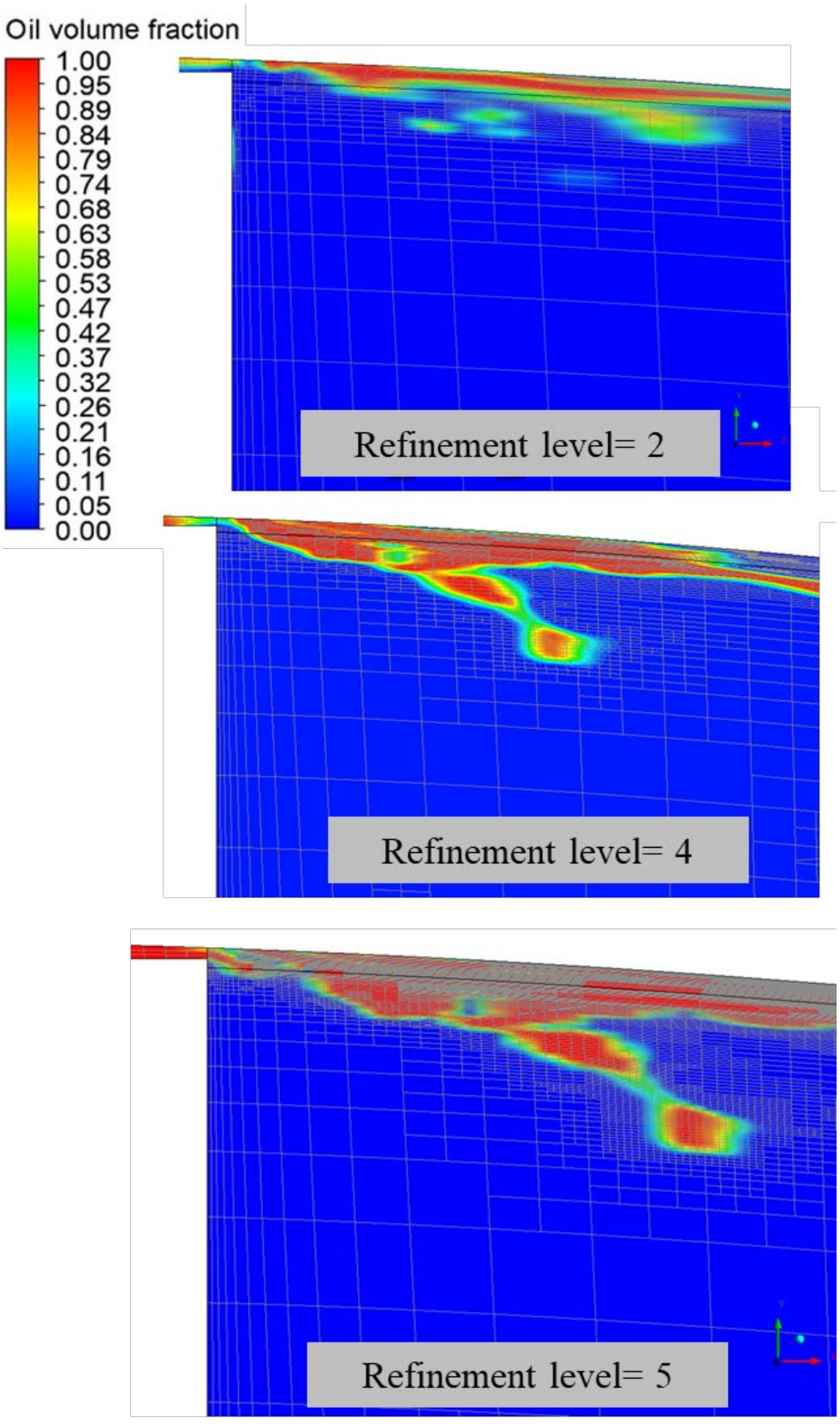

Figure 68. Oil volume fraction contour for x-y plane with refinement levels= 2,4 and 5 at time= 0.005 s.

First, the refinement level was set as 2, and the contour of oil volume fraction obtained with this setting at the 5000th time step (0.005 s) is shown in Figure 68. It can be seen from the figure for refinement level 2 that the oil volume fraction is under-resolved. From this point, the refinement level is doubled to 4, and it can be seen in the figure that the oil volume fraction is well-resolved at this setting. Increasing the refinement level from 4 to 5 shows no significant improvement as seen when the refinement level increased from 2 to 4 (Figure 68). Also, at a time instance of 0.005s, additional 200,000 cells are present with refinement level 5 compared to the refinement level 4. Therefore, in the interest of achieving good resolution along with the reduced computational cells, refinement level 4 will be used for analysis in this study—refinement level 4 results in 2.2 million cells during adaption.

Furthermore, to account for oil droplet sizes in the computational domain, some approaches are needed to identify the isolated lumps as droplets. The identification of the isolated droplets is conducted based on input diameter range, asphericity, maximum oil volume fraction and surrounding air volume fraction. The elaborate details of these identification parameters, as well as asphericity, are explained in Section 2.2.4. The values of the identification parameters are shown in Table 33. The asphericity value used in this case is 0.5. Simulation of liquid jet flow atomisation in literature has shown close predictions with experimental data when the asphericity value is 0.5 [104].

Table 33. Parameters from oil droplet identification.

Parameter	**Value**
Diameter range [μm]	25-1000
Asphericity	0.5
Maximum oil volume fraction	>0.9
Surrounding air volume fraction	0

7.5 Results and discussions

This study considers the evolution of oil after it is accelerated through the clearance. This is firstly studied without the adaptive mesh refinement and then with the adaptive mesh refinement. The objective is to identify the flow features than be captured with the adaptive mesh refinement techniques. Also, forces responsible for the formation of the oil film and its disintegration into droplets are evaluated. The distribution of oil droplets is recorded at 0.02 s, in order to estimate the Sauter mean diameter size of the oil droplet in this simplified compression domain.

7.5.1 Results obtained without the adaptive mesh refinement

The contour of oil volume fraction in a cross-sectional plane is shown in Figure 69 as a function of time. Oil flows from domain 1 to domain 2 due to the pressure difference between them. The combination of inertia, surface tension and interfacial shear stress between air and oil is responsible for forming an oil film on the casing, as shown in Figure 69a.

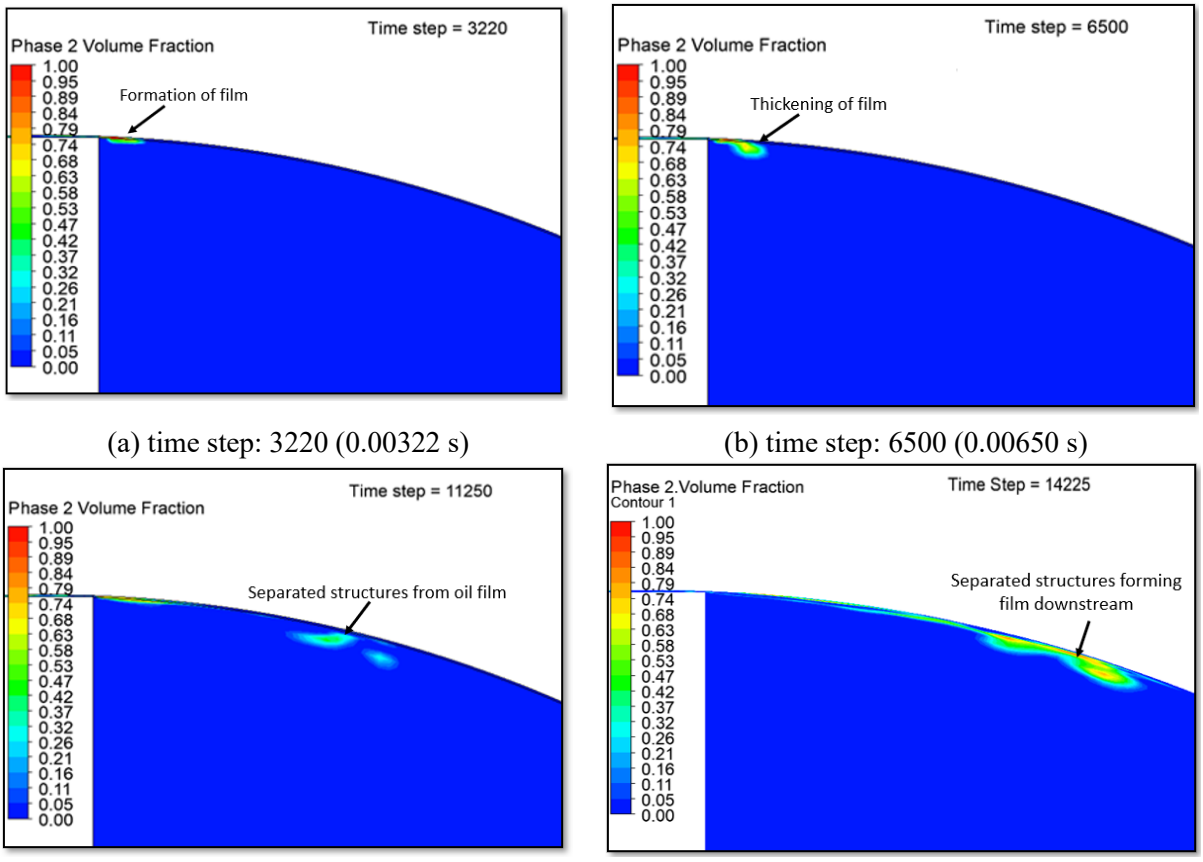

(a) time step: 3220 (0.00322 s)

(b) time step: 6500 (0.00650 s)

(c) time step: 11250 (0.01125 s)

(d) time step: 14225 (0.014225 s)

Figure 69. Oil volume fraction contour on plane z= 0.0025m for various time steps.

Figure 69b shows an increasing thickness of the oil film leading to a breakup. The breakup leaves behind a thin oil layer attached to the casing wall, as shown in Figure 69c. The thin layer that is left behind is driven through shear and spreads further across the casing walls. The separated oil structures navigate towards the casing at a point away from the initial separation due to the centrifugal forces acting on them. Once the separated structures are closer to the casing wall, surface tension forces reattach oil to the wall/casing surface (Figure 69d). This dynamics of the detachment of oil phase structures at a certain point and reattachment at a farther point due to centrifugal forces continues until a thin, stable film is formed throughout the casing curvature. These features of film thickening and breakup for the complete casing curvature are shown in Figure 70 for the last time 41800, which is 0.0418 s. A stable film thickness of around 55 µm on the casing walls is obtained for this computational domain.

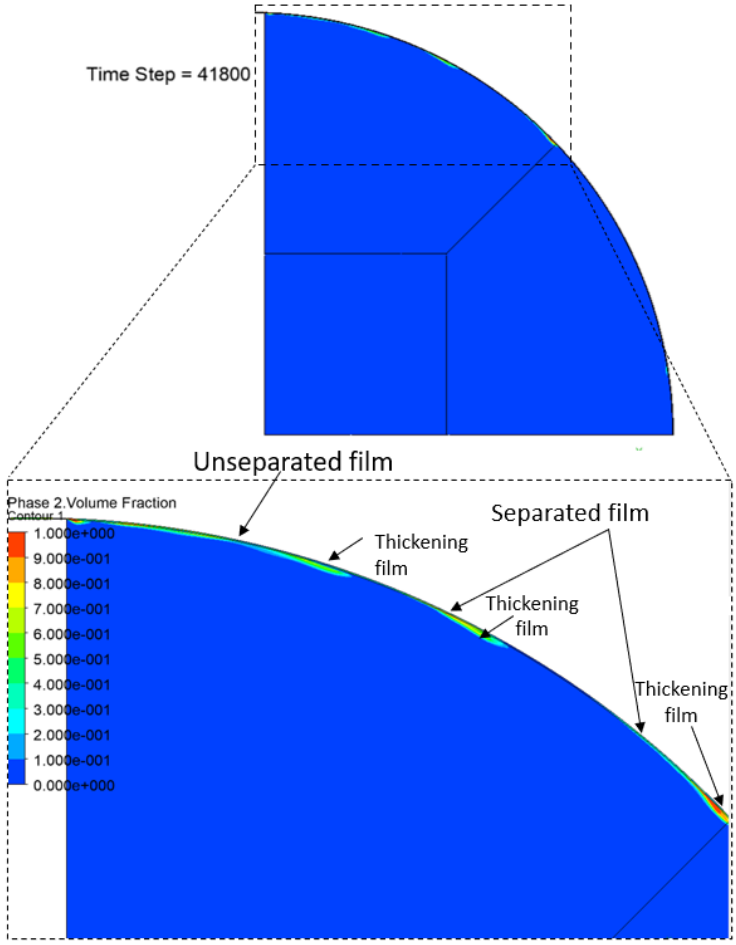

Figure 70. Oil volume fraction contour for plane z=0.0025m at time= 0.0418 s.

However, the detailed breakup structures could not be observed due to the large size computational cell in the initial mesh (Figure 66). Micron level computational cell sizes are needed to capture the air-oil interface adequately, and achieving this without any region-

specific refinement will be a massive computational task. Therefore, the next section will explore the oil volume fraction with adaptive mesh refinement in the same domain.

7.5.2 Results obtained with the adaptive mesh refinement

7.5.2.1 Oil phase breakup with time

Adaptive mesh refinement is applied to increase the accuracy of the oil break-up predictions and minimise numerical diffusion of the air-oil interface. This will help understand the flow features resulting in oil droplets in the compression chamber. The simulation is run for 20,000-time steps, which is 0.02 s. The oil film is formed throughout the casing walls within 0.02 s.

Figure 71 a and b shows the oil distribution and vorticity magnitude on the oil iso-surface behind the rectangular profile for time steps 510 and 3220. Similarly, Figure 72 shows oil distribution and vorticity magnitude for time steps 6500 and 6950. The interaction between oil and the surrounding field can be investigated through vorticity acting on the interface. Vorticity can be defined as $|vorticity| = \sqrt{(\frac{\partial u_z}{\partial u_y} - \frac{\partial u_y}{\partial u_z})^2 + (\frac{\partial u_x}{\partial u_z} - \frac{\partial u_z}{\partial u_x})^2 + (\frac{\partial u_y}{\partial u_x} - \frac{\partial u_x}{\partial u_y})^2}$.

At time step 510 (Figure 71a), oil enters domain 2 due to the differential pressure between domain 1 and domain 2. With added momentum from rotor tip velocity and surface tension acting between air-oil, oil starts to form a film on the casing in the direction of the velocity. High vorticity values are evident in the vicinity due to the presence of the boundary layer. A combination of high and low vorticity acting across the edge of the oil film shows high interfacial shear forces acting in this region that stretches the oil film with time. Stretching leads to thinning of oil film resulting in a hole connected by ligaments in Figure 71b. High values of vorticity are found on the downside of the ligament connected with the hole, as shown in Figure 71b. The strong vorticity and surface tension forces acting on this region stretch the holes further until a breakup is achieved to form ligaments, as shown in Figure 72a. These ligaments stretch axially until breakup is achieved to form irregular droplets, lobe-like or bag-like structures, as shown in Figure 72b. This initiated a secondary breakup. The structures created by the secondary breakup resemble lobe-like structures in 2D, which are bag or rim like structures in three-dimensions.

Here, primary breakup refers to the first level of detachment from the liquid film in the form of lobes, ligaments and droplets. And secondary breakup refers to subsequent breakup from the first level of detached structures into further atomisation.

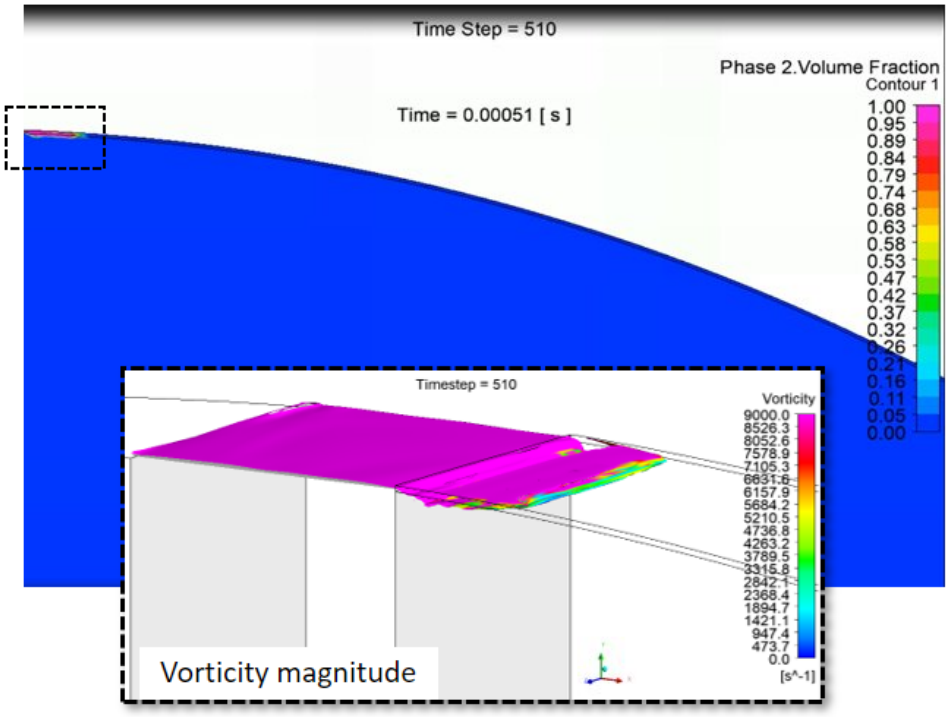

(a) time step: 510 (0.00051 s)

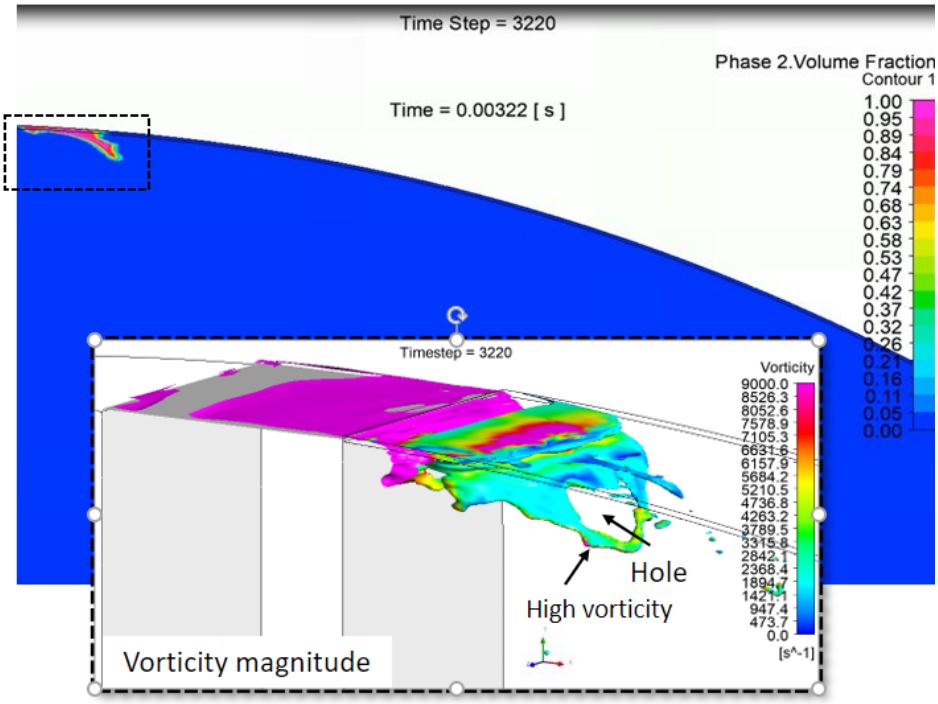

(b) time step: 3220 (0.00322 s)

Figure 71. Contour of oil volume fraction at plane z= 0.0025m and oil volume fraction isosurface of 0.6 coloured by vorticity magnitude at various time steps.

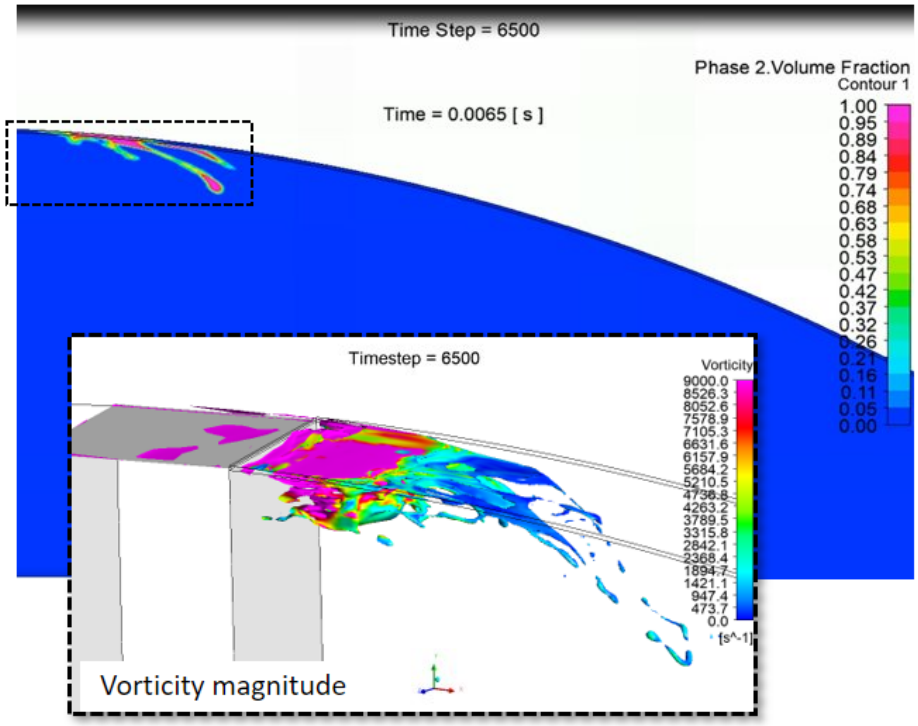

(a) time step: 6500 (0.065 s)

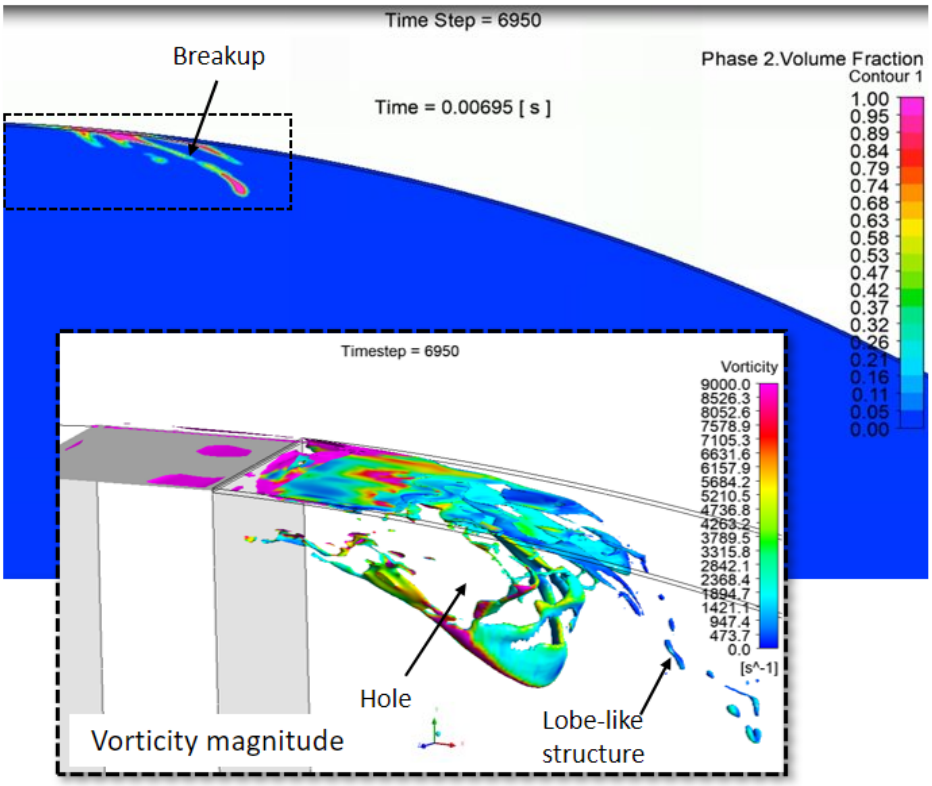

(b) time step: 6950 (0.0695 s)

Figure 72. Contour of oil volume fraction at plane z= 0.0025m and oil volume fraction isosurface of 0.6 coloured by vorticity magnitude at various time steps.

The secondary breakup of lobe-like structures is shown in Figure 73. These features are part of the breakup from the oil film. The tangential velocity vectors are overlapped on the contour of vorticity magnitude in s^{-1}, and curvy black lines indicate the oil interface. Figure 73 a-f indicate frames at the increasing time to observe the transition in oil interfaces.

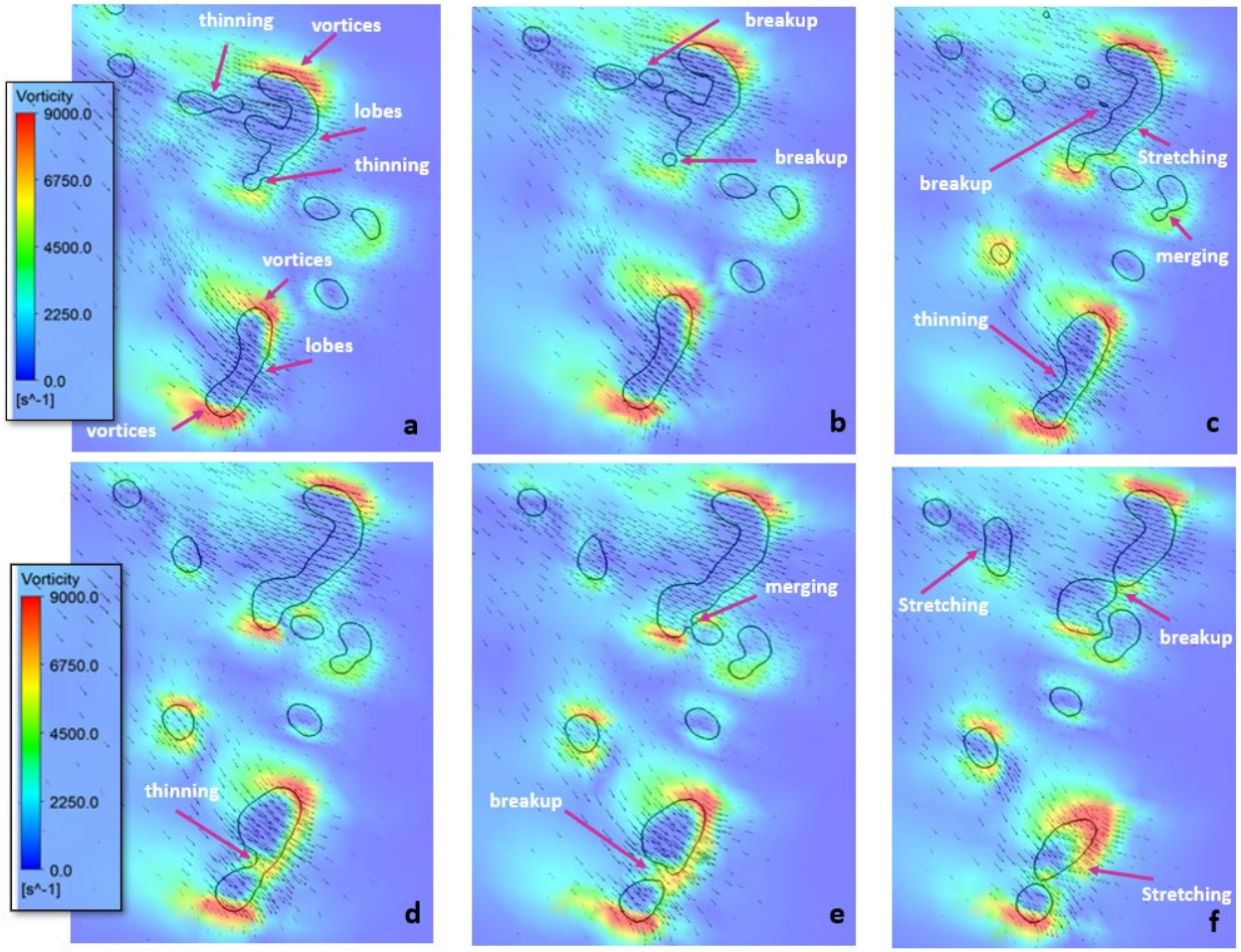

Figure 73. Breakup of secondary oil structures with vorticity contour and overlapping velocity vector.

High vortex intensity close to 9000 s^{-1} is seen at the head and the bottom of the lobe-like structures as well the on the rounded interfaces. The counter-rotating vortices acting on the top and bottom of the lobe-like structure along with the directional velocity at the lobe's centre tend to stretch the lobes Figure 73a. Uneven lobe-like structures are quickly becoming thinner and break to form another lobe-like structure, as shown in Figure 73b and Figure 73c. The process repeats, forming new droplets of the elliptical shapes, as shown in Figure 73e and Figure 73f. These ellipse shapes will be pulled to form smaller lobes and will continue to stretch until smaller droplets are formed with advancing in time. Hence, this stretching and thinning evolution is observed until the droplets are formed in the compression domain. The limit of droplet size in this calculation is around 25 μm as the computational cell size refinement is limited to $1x10^{-14}$ m^3. The minimum droplet size achieved in a realistic situation is not known.

With time, the amount of oil that enters through the clearance is increasing. This oil adds to the oil film layer due to surface tension, which increases the film thickness. Strong shear forces act on this thick oil film, leading to sheet thinning, ligaments and break up into bigger structures than just the lobe-like structures observed at the initial time steps (Figure 74a-d). Again, these larger structures are stretched to strip further into many lobe-like structures.

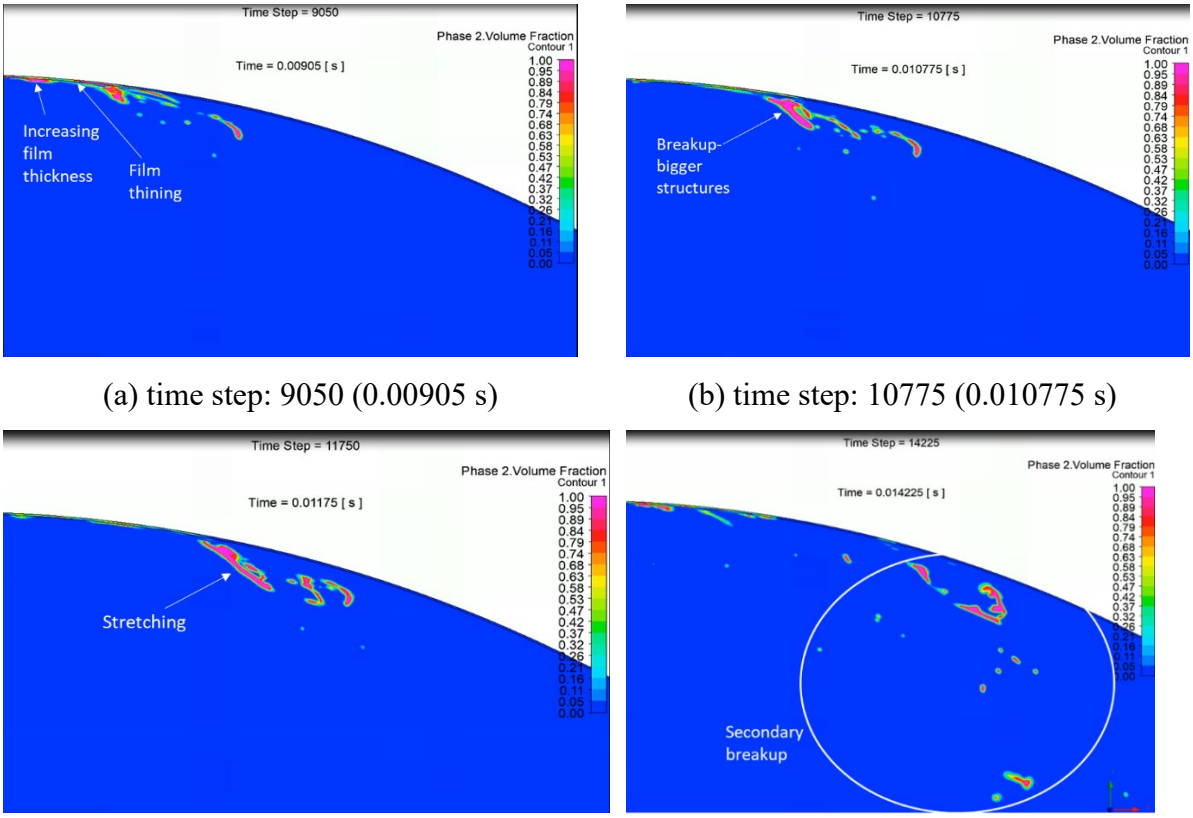

(a) time step: 9050 (0.00905 s) (b) time step: 10775 (0.010775 s)

(c) time step: 11750 (0.01175 s) (d) time step: 14225 (0.14225 s)

Figure 74. Contour of oil volume fraction at plane z= 0.0025m for various timesteps (9050-14225).

The aerodynamic and inertial forces act further on these lobe-like structures resulting in the further break up into droplets, as shown in Figure 73. The droplets are produced due to the primary as well as a secondary breakup. Only a thin oil film of around 55µm remains stable on the casing walls.

Finally, at the last calculated time step of 20,000 (0.02s), more oil phase deformation features are observed (Figure 75). Frame 1 shows the stable oil film with the increasing concentration, which can lead to the formation of ligaments. In Frame 2, an oil film still exists on the casing, but the instability and separation of oil are noticed due to the interfacial shear forces. In Frame 3, the large structures are separated from the oil film and start to break up to form droplets. Oil film on the casing surface is now discontinuous. The reason might be that the shear and inertial forces are overpowering the surface tension forces. Therefore, in Frame 4, the unstable film becomes discontinuous towards the end of the computational domain.

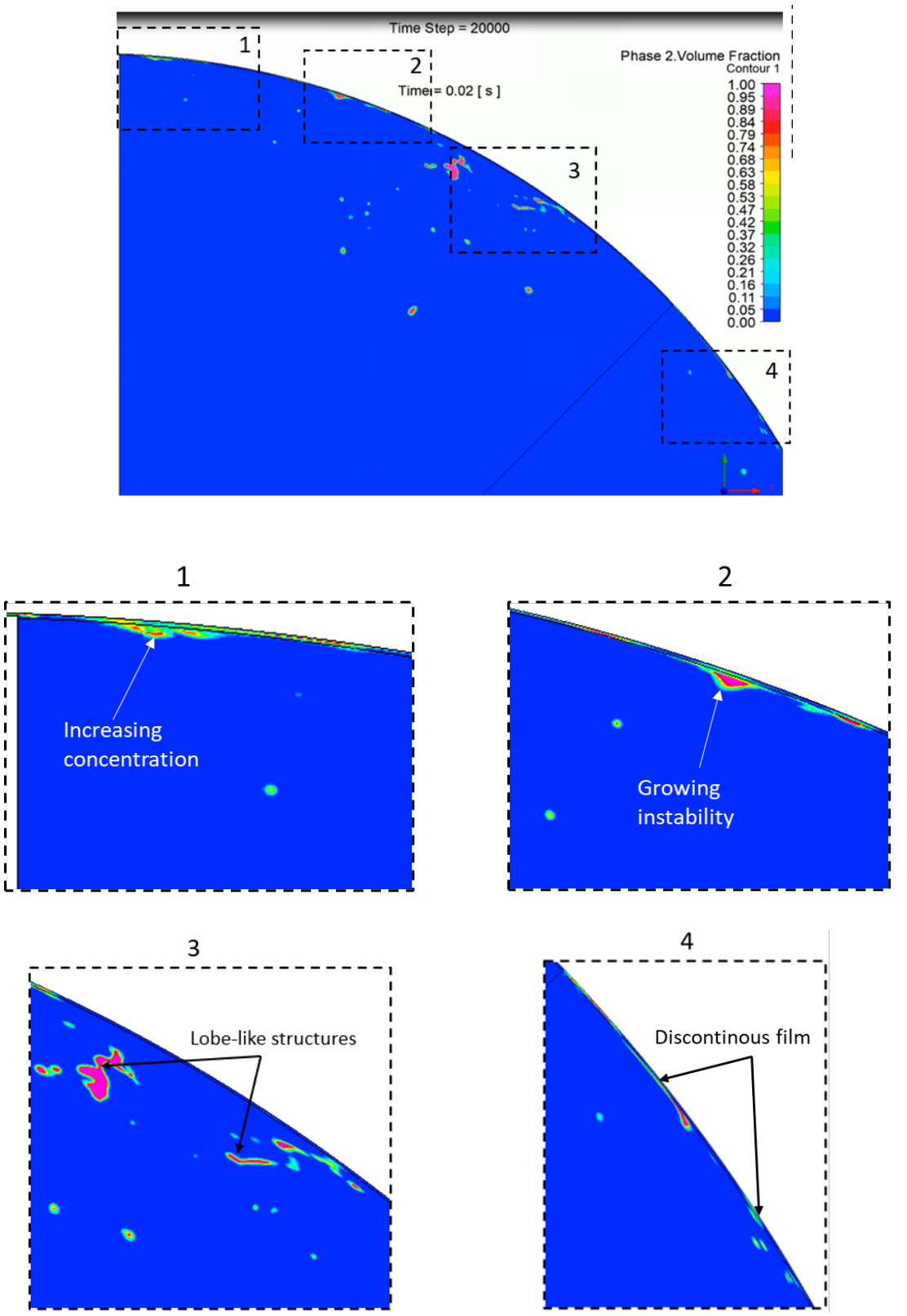

Figure 75. Contour of oil volume fraction at plane z= 0.0025m and timestep= 20,000 (time= 0.02s).

The same features are also shown in Figure 76 and Figure 77 through the oil volume fraction iso-surface of 0.1 coloured by the velocity magnitude at different time steps.

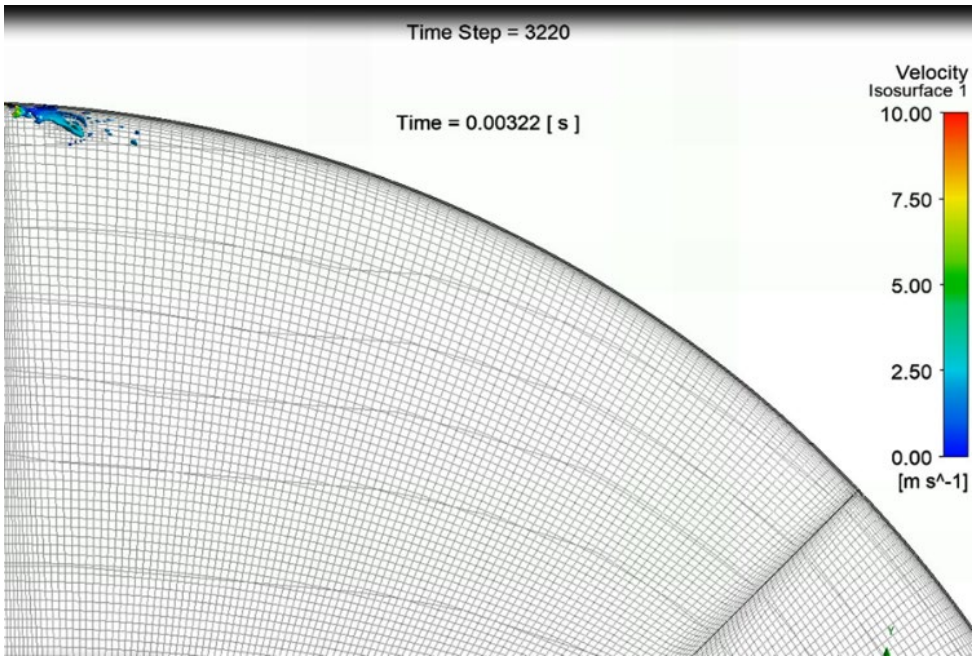

(a) time step: 3220 (0.00322 s)

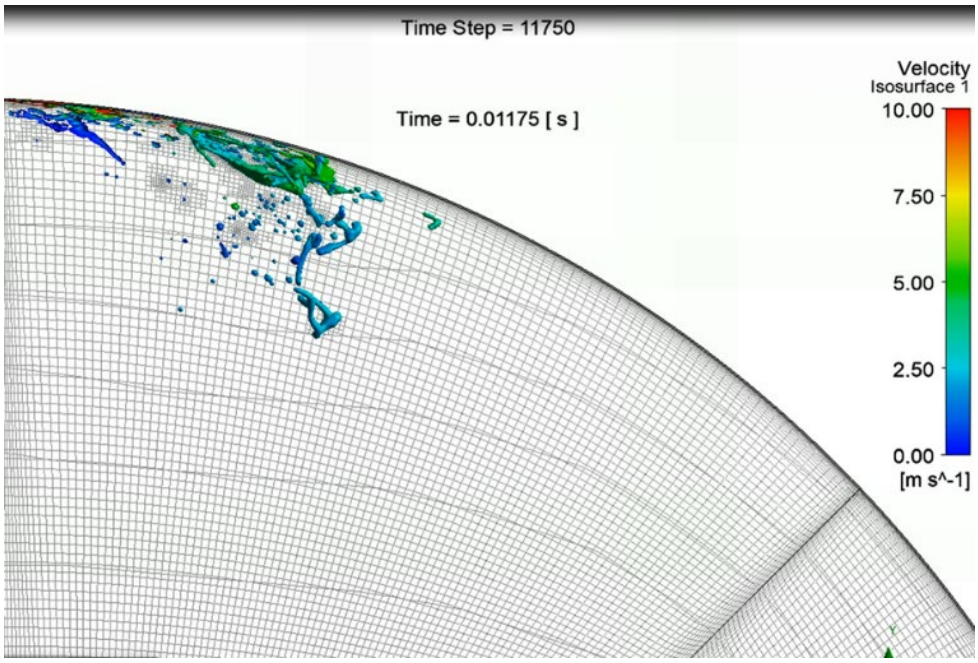

(b) time step: 11750 (0.01175 s)

Figure 76. Oil volume fraction iso-surface of 0.5 coloured with velocity for time steps 3220 and 11750.

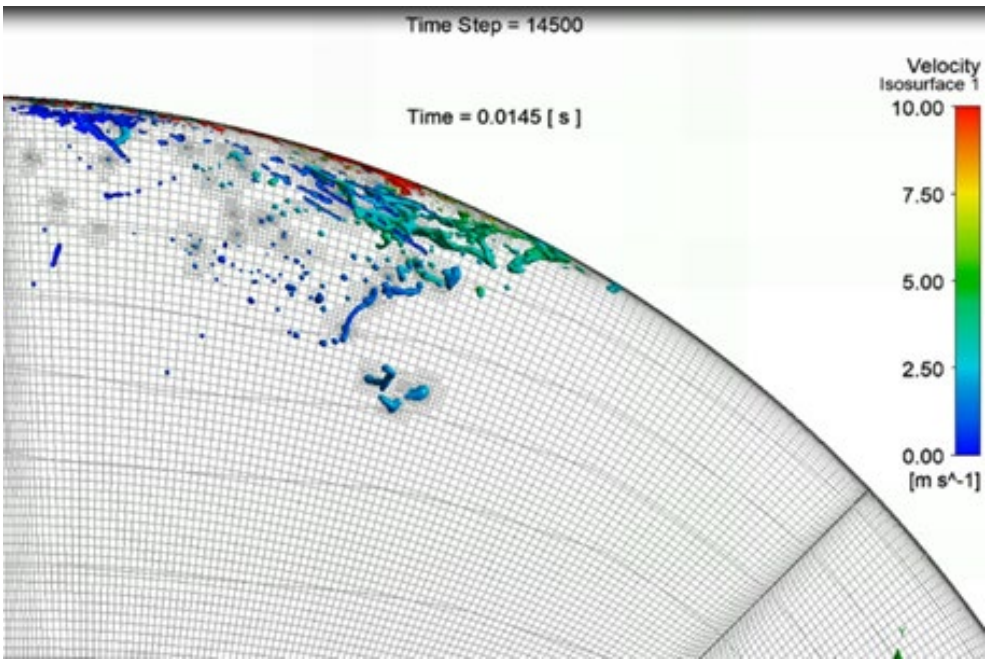

(a) time step: 14500 (0.0145 s)

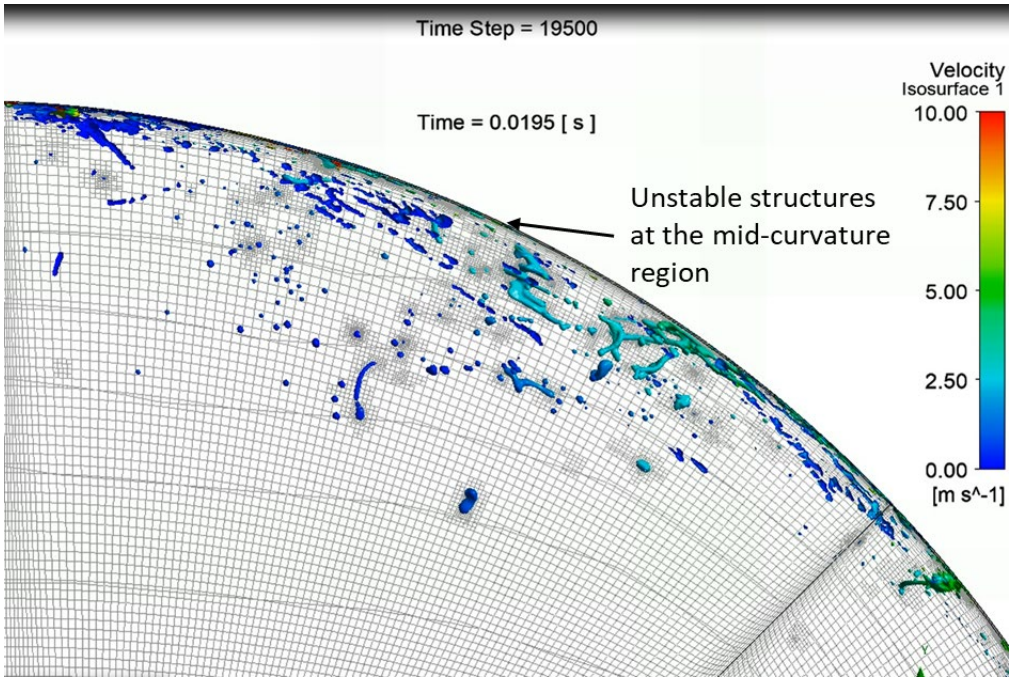

(b) time step: 19500 (0.0195 s)

Figure 77. Oil volume fraction iso-surface of 0.5 coloured with velocity for time steps 14500 and 19500.

With time, high velocity and unstable oil film are shifted towards the end of the computational domain while a more stable film exists closer to the rotor profile, as shown in Figure 76a, Figure 76b and Figure 77a. It can be observed that unstable structures with ligaments, lobes and droplets are observed throughout the domain, especially when the flow is more developed at the later time steps of 19500, at the mid curvature region in Figure 77, similar to frame 3 in Figure 75.

Higher velocities are observed at the primary breakup closer to the casing wall, and lower velocities are found during the secondary breakup of ligaments and lobe-like structures (Figure 77b). Overall, the primary and secondary breakup observed within the simplified compressor domain results in smaller droplets, increasing the contact area for heat exchange between oil and gas.

Due to the lack of experiments, the simulated iso-surface predictions are qualitatively compared with the published experimental literature for a particular time of 0.0136 s, as shown in Figure 78. The experimentally captured images with a high-speed camera for a transparent chamber. The transparent chamber's geometry is the same as the computational domain in this study, but the injected phase is water [101]. Although the experiments show the disintegration of water film, the droplet sizes are not measured, limiting to qualitative comparison with this literature.

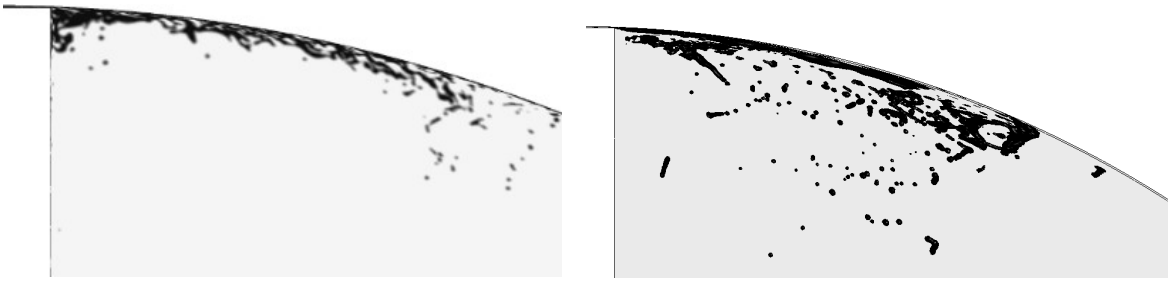

(a) experiment- water (b) prediction- oil

Figure 78. Comparison between the visualisation of injected second phase with (a) high-speed imaging in the published literature [101] and (b) predictions from the current model for oil iso-surface of 0.09.

This study focuses on oil droplet sizes; therefore, oil had to be used as an injected fluid. It is expected that the qualitative comparison with oil or water should be similar. The numerical results qualitatively agree reasonably well with this experimental result even though there is a difference in the injected fluid. Both results show a formation of liquid film that is unstable along with ligaments and droplets, but more satellite droplets are evident when oil is the working media than the water. This is due to the low surface tension of oil at 32 mN/m than water at 72 mN/m, resulting in higher disintegration of the oil phase.

7.5.2.2 Oil droplet distribution

The results for oil volume fraction in the computational domain at 0.02s is used to identify and quantify the droplet sizes. At the time instance 0.02s, most of the oil film is already spread across the casing wall, and the dynamics oil atomisation features do not vary significantly beyond this time. Identification for droplets is conducted by checking the oil diameter ranges, asphericity, maximum oil volume fraction and the surrounding oil volume fraction. These parameters and their values are presented and explained in Table 33 of Section 7.4.1.

The oil droplet distribution is presented for the timestep= 20,000 and time =0.02 s in Figure 79. The diagram shows the percentage of droplets within each of the defined diameter sizes.

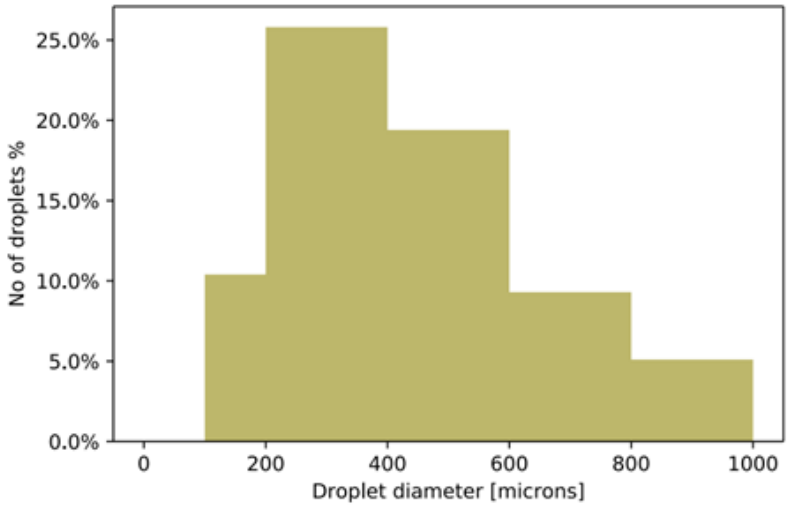

Figure 79. Droplet size distribution at time= 0.02 s.

The volume mean droplet size is 279 µm, and Sauter mean diameter is 386 µm. These are calculated through equations (5) and (6) in section 2.2.3. The predicted Sauter mean diameter through Harmon's semi-empirical model is almost ten times higher than the currently predicted Sauter mean diameter. Thus, the currently available semi-empirical models are not suited for oil droplet size in a compression domain.

There are not many validations that exist to show the oil droplet sizes inside a screw compressor domain. Only one published study has shown that the volume mean diameter at the discharge of the screw compressor before the separator is between 290-390 μm depending on the operating conditions [36]. The calculated volume mean droplet size in the computational domain falls within this range. This gives confidence that the predicted values of Sauter mean diameter is in a reasonable order of magnitude as confirmed by measurements. This study does not consider the effect of coalescence, which can result in slightly bigger droplets that can better fit the measured range.

The oil droplets sizes will have a major effect on the heat transfer between gas and oil in the compression domain, but the effect is not quantified here as it is beyond the scope of this thesis.

7.6 Summary

Reducing the oil droplet diameters will improve the heat transfer and consequently reduce gas temperature and improve compressor efficiency. However, the literature review revealed that using various atomisers for oil injection made only negligible improvements in the compressor performance. Therefore, the mechanism for atomisation of oil by acceleration through the radial clearance gaps is explored in this study as a mechanism for atomisation. The study is conducted by constructing the simple computational domain with a rectangular rotor profile, applying differential pressure of 1.5 bar between the working chambers, a rotational speed of 6000 rpm and a rotor tip speed of 22 m/s. VOF fluid model is applied to study the transition of oil in the domain.

The key conclusions from this study are:

- The interplay of surface tension, shear stresses and inertial forces are responsible for the formation and breakup of the oil film on the casing curvature. The surface tension forces tend to result in a stable film on the casing walls, while inertial forces and shear stresses tend to break the film. Centrifugal forces act on oil to drive it into the oil film on the casing.
- Film formation and breakup can be captured without adaptive mesh refinement, but the disintegration of the continuous oil phase into droplets is captured only by dynamically refining the mesh based on the second derivative of oil volume fraction gradient.
- The oil phase in the compression chamber undergoes various levels of breakup to form droplets, and these can be classified as:
  i. Primary breakup: Oil film stretches to form ligaments, and these ligaments stretch to form droplets. Additionally, strong shear forces cause the oil film to break up, resulting in random lobe-like or bag-like structures.
  ii. Secondary breakup: Disintegrated lobe-like structures become thinner due to interfacial shear and surface tension forces acting on them to form droplets.
- Oil droplet sizes, when quantified for the last calculated time step at 0.02 s, give an oil Sauter mean diameter of 386 µm and volume mean diameter of 279 µm.
- The disintegration of oil film looks qualitatively similar to the image captured by a high-speed camera for the same geometry as published in the literature. The volume mean diameter is close to the range of measured oil droplet sizes at the discharge of the screw compressor in a separate literature resource.

This study touches upon the physics of oil atomisation in screw compressors. It has the potential to be used for further analysis, which can help to reduce gas temperatures in a compression chamber and improve compressor efficiency further.

Chapter 8 Conclusions and Recommendations for Future Work

8.1 Summary

The increase in energy consumption is a growing worldwide concern. Improving the efficiency of oil-injected screw compressors will lead to energy savings and a reduced carbon footprint. In this thesis, investigations are carried out to study oil distribution at a variety of oil injection conditions in an industrial oil-injected twin-screw compressor. The methodology used in this study is Computational Fluid Dynamics (CFD) with Volume of Fluids (VOF) model. It is extended by adaptive mesh refinement to reveal the oil film formation and disintegration of the oil into droplets in a simplified compression domain.

Chapter 1 introduces the problem of energy consumption by compressors as they are deployed in various systems and processes in industry sectors like energy, manufacturing, construction etc. where oil-injected twin-screw compressors are commonly used. Hence, improving the efficiency of oil-injected screw compressors even by a small percentage can result in gains for energy consumption and the environment. Oil in these machines plays a key role in cooling the compression chamber. The key injection parameters such as oil flow rate, position and number of injection ports and Sauter mean diameter of an oil droplet in the compression chamber will affect the compressor cooling temperatures and thereby performance. Hence, to understand the temperatures in the compression chamber, oil distribution needs to be explored.

Chapter 2 explores literature resource for mathematical and experimental methods used for optimising oil injection. It was noticed that most of these methods assume a uniform distribution of oil in a compression chamber which in many cases could not be verified. Therefore, the existing computational fluid dynamics methods with the state-of-the-art mesh generation techniques for twin screw compressors are explored. Focus is paid to finding a suitable solver for computational modelling of an oil-injected twin-screw compressor. Ansys Fluent was selected as it has a variety of multiphase modelling approaches, offers customisation through user-defined functions, and evidence exists of a successful application to air-oil cooling flows in bearings, scroll compressors and gears. In addition to this, a liquid

phase breakup in a gas medium was studied before but requires further investigation, including the adaptive mesh refinement technique.

Chapter 3 states the objectives of the thesis, the methodology adopted to fulfil these objectives and the expected contributions.

Chapter 4 describes the development of user-defined functions required for analysis of oil injection in screw compressors using Computational Fluid Dynamics solver Ansys Fluent. The user-defined function utilises user-defined nodal displacement to import meshes generated from SCORG required to capture rotor rotation in each time step. These user-defined functions are also extended to work on parallel computer cores as the calculation of multiphase flows in a compressor is computationally intensive. Then the developed interface is tested for an oil-free compressor operating at a discharge pressure of 3 bar, and a male rotor speed of 6000 and 8000 rpm.

Chapter 5 describes the assessment of multiphase flow models suitable for the analysis of screw compressors. The two-phase models analysed in Ansys Fluent are the Eulerian-Eulerian, VOF and mixture model, while the results for the Eulerian-Eulerian model were used for Ansys CFX due to the instability of this scheme in Ansys Fluent. Compressor operating at a discharge pressure ratio of 7 bar, and a male rotor speed of 6000 rpm was analysed using these models. It was found out that the VOF model is suitable for the analysis of screw compressors due to its stability, relatively low computational time, and reasonable accuracy checked against the measured performance data.

Chapter 6 compares the numerically calculated performance of the oil-injected air screw compressor operated at discharge pressures of 8.5 bar and 10.5 bar, and the male rotor speed of 6000 rpm for different size and numbers of oil injection holes. Analysis of Oil distribution and temperature for a compressor with a single injection port on the female rotor revealed that high temperatures exist in the compression domain even if the oil flow rate is increased by a factor of ten. Therefore, an additional oil injection port was introduced on the male rotor. The sizes of the ports are adjusted to maintain the same amount of oil as in the compressor with the single injection point. The additional injection port helped uniformly distribute oil and reduce temperatures in the compression chamber, which improved the compressor efficiency.

Chapter 7 presents the analysis with the adaptive mesh refinement and VOF modelling in a simplified compression domain to evaluate the formation of oil droplets and to estimate their size. This study revealed some features of the oil film formation and disintegration through two breakup stages named primary and secondary. In the primary breakup phase, the oil film stretched to form ligaments, droplets and lobe-like structures. The lobe-like structures stretch to form droplets in the secondary breakup eventually. The estimated Sauter mean diameter of oil droplets in this computational domain is 386 μm.

8.2 Conclusions

The main achievements of the research presented in this thesis are as follows :

- The user-defined nodal displacement code was developed to integrate the deforming grids from SCORG with the Ansys Fluent for a solution on parallel computer nodes.
- The developed UDF interface has been successfully checked for an oil-free test compressor and later on applied for the analysis of the oil-injected compressor.
- Amongst various two-phase flow models evaluated for the analysis of oil-injected twin-screw compressors, the VOF model in Ansys Fluent is the preferred model as the computation time is 24.7% shorter than the Eulerian-Eulerian model, and the integral performance of flow rate and power is close to the experimental data.
- The CFD analysis of an oil-injected compressor with the VOF model has produced performance values close to experimental results with differences of 0.5% for airflow and 3% for power, respectively, at 8.5bar and 0.7% for airflow and 2.3% for power at 10.5bar. The rotational speed is 6000 rpm.
- Using CFD analysis with single point oil injection, it was found out that the compressor efficiency improved as the port diameter was increased from 3mm to 5mm. Further increase in the oil diameter and the oil flow rate did not make any significant performance improvements. With this approach, the high-temperature spots of 157°C are detected in the compression chamber, although the discharge temperature was much lower at 67°C, indicating that oil distribution within the chamber should be improved. The proposed method was injection on both the male and female rotor side.
- Introducing the second oil injection point on the male rotor while maintaining diameters to retain the same oil flow rate as with the single-point injection helped reduce the peak temperature by 30ºC and specific power by 1.8%.
- This analysis gave an insight into oil distribution and its effects on local temperatures. Such detailed analysis will form the basis for designing and optimising oil injection ports in twin screw compressors in future.
- VOF modelling with adaptive mesh refinement based on oil volume fraction gradient has revealed the mechanism of oil film formation and breakup in a simple compression domain.

- Surface tension holds the oil phase close to the walls forming a thin film, and centrifugal forces act on the film to spread it across the casing.
- Shear stresses between air and oil and inertial forces cause the oil film to break up into droplets and lobe-like structures. Vorticity acts on lobe like structures for a further break up into droplets.
- The disintegration pattern of oil film qualitatively matches with the experimentally captured image from the literature.
- The droplets in the compression chamber are estimated to have the Sauter mean diameter of 386 μm, and volume mean diameter of 279 μm.

8.3 Recommendations for future work

To fully utilise the capability of multiphase flow modelling for an oil-injected compressor and improve its efficiency, some future actions are suggested:

- If the currently available grids for twin-screw compressor could be adapted to include adaptive refinement near casing and rotor walls based on the oil volume fraction, such models will be capable of capturing oil film that effects lubrication and sealing. It could also lead to more information on oil droplet sizes in complex geometrical domains.
- Experimental validation of oil distribution and temperatures within the working chamber of the oil-injected twin-screw compressor would contribute to a better understanding of oil – gas interaction in the compression chamber. Techniques such as high-speed imaging in a compressor with a transparent casing could be considered. This will further solidify oil flow characteristics in a twin-screw machine and help improve the model.
- Multiple CFD simulations with experimental validations can be conducted for various design changes in oil-injection parameters such as the number of oil-injection ports, port positions, and port diameters. Also, variations in operating conditions such as pressure ratio and male rotor shaft speed can be considered. The results obtained from these simulations can be used to train cheap Surrogate based Machine Learning optimisation models. The objective function of this model could be to achieve averaged minimal temperature in the compression chamber for respective operating conditions indicating improved cooling. Then these models can be used to find the most optimal injection port diameter, position, and the number of ports for minimal compression chamber temperatures. Provided there will be huge computational power needed to run multiple CFD simulations to train these models.
- The possibilities of exploration and developments to understand the effects of the oil on the performance of oil-injected screw compressors are virtually limitless. The author hopes that developments and investigations in this thesis will contribute to defining future research directions.

References

[1] D. Vittorini and R. Cipollone, "Energy saving potential in existing industrial compressors," *Energy*, vol. 102, pp. 502–515, 2016, doi: 10.1016/j.energy.2016.02.115.

[2] "Internation Energy Outlook- US Energy Information Adminstration," 2020. https://www.eia.gov/outlooks/ieo/ (accessed Oct. 31, 2020).

[3] "Innovation is an essential part of dealing with climate change," *The Economist*, Oct. 2020.

[4] "Carbon capture, utilisation and storage (CCUS) in clean energy transitions," *iea.org*, 2020. https://www.iea.org/reports/ccus-in-clean-energy-transitions/a-new-era-for-ccus?utm_content=buffer93f50&utm_medium=social&utm_source=facebook.com&utm_campaign=buffer&fbclid=IwAR2eyYTIryR8ZR4OVFYoIwwqYzCcTOD4sA39F_nI3Jcs0skV1C2FotlvqMY (accessed Dec. 20, 2020).

[5] "Compressed air equipment presentation by Department for Business, Energy and Industrial Strategy," 2020. https://assets.publishing.service.gov.uk/government/uploads/system/uploads/attachment_data/file/879754/Compressed_Air_Technology_Information_Leaflet_-_April_2020.pdf (accessed Oct. 03, 2020).

[6] S. Rane, "Grid Generation and CFD Analysis of Variable Geometry Screw Machines," PhD thesis, City University London, 2015.

[7] T. Ohama, Y. Kurioka, H. Tanaka, and T. Koga, "Process Gas Applications Where API 619 Screw Compressors Replaced Reciprocating and Centrifugal Compressors," Lecture, Texas A&M University. Turbomachinery Laboratories, 2006. https://hdl.handle.net/1969.1/163186 (accessed Mar 15, 2021).

[8] "Screw Compressor- Global Compressor and Trajectory Analysis." Report, 2020. https://www.strategyr.com/market-report-screw-compressor-forecasts-global-industry-analysts-inc.asp (accessed Oct. 03, 2020).

[9] I. A. Sakun, *Vintovie kompresorii (Screw Compressors)*. Mashinostroenie Leningrad, 1960.

[10] P.O'Neill, *Industrial Compressors, Theory and Equipment*. Oxford: Butterworth-Heinemann, 1993.

[11] I. Arbon, *Twin Shaft Compressors in Gas Process Industry*. London: IMechE Publications, 1994.

[12] S. Rane, A. Kovacevic, and N. Stosic, "CFD Analysis of Oil Flooded Twin Screw Compressors," *Int. Compress. Eng. Conf.*, no 2392, 2016.

[13] N. Stosic, L. Milutinovic, K. Hanjalic, and A. Kovacevic, "Experimental Investigation of the Influence of Oil Injection Upon the Screw Compressor Working Process,"*Int. Compress. Eng. Conf* , no 687, 1990, [Online]. Available: http://docs.lib.purdue.edu/icec/687/.

[14] M. Fujiwara, "Performance analysis of an oil-injected screw compressor and its application," *Int. J. Refrig.*, vol. 18, no. 4, pp. 8–9, 1995. doi: 10.1016/0140-7007(95)00008-Y

[15] N. Stošic, L. Milutinović, K. Hanjalić, and A. Kovačević, "Investigation of the influence of oil injection upon the screw compressor working process," *Int. J. Refrig.*, vol. 15, no. 4, pp. 206–220, 1992, doi: 10.1016/0140-7007(92)90051-U.

[16] N. Stosic, A. Kovacevic, K. Hanjalic, and L. Milutinovic, "Mathematical modelling of the oil influence upon the working cycle of screw compressors," *Int. Compress. Eng. Conf,* no. 645, 1988, [Online]. Available: http://docs.lib.purdue.edu/cgi/viewcontent.cgi?article=1644&context=icec.

[17] B. Sangfors, "Computer simulation of the oil injected twin screw compressor.," *Int. Compress. Eng. Conf,* no. 502, 1984, [Online]. Available: https://docs.lib.purdue.edu/cgi/viewcontent.cgi?article=1501&context=icec

[18] W. Wu, C. Hu, J. Hu, and S. Yuan, "Jet cooling for rolling bearings: Flow visualization and temperature distribution," *Appl. Therm. Eng.*, vol. 105, pp. 217–224, 2016, doi: 10.1016/j.applthermaleng.2016.05.147.

[19] W. Wu, C. Hu, J. Hu, S. Yuan, and R. Zhang, "Jet cooling characteristics for ball bearings using the VOF multiphase model," *Int. J. Therm. Sci.*, vol. 116, pp. 150–158, 2017, doi: 10.1016/j.ijthermalsci.2017.02.014.

[20] J. Wu and G. Wang, "Numerical study on oil supply system of a rotary compressor,"

Appl. Therm. Eng., vol. 61, no. 2, pp. 425–432, 2013, doi: 10.1016/j.applthermaleng.2013.07.047.

[21] A. A. Adeniyi, "A Coupled Lagrangian-Eulerian Framework to model droplet to film interaction with Heat Transfer," *PhD Thesis*, University of Nottingham, 2014.

[22] "Lubrication problems." http://www.airends.com/lubrication_problems.htm (accessed Oct. 03, 2020).

[23] P. Singh and J. Bowman, "Heat Transfer in Oil-Flooded Screw Compressors," *Int. Compress. Eng. Conf.*, pp. 135–153, 1986, [Online]. Available: http://docs.lib.purdue.edu/cgi/viewcontent.cgi?article=1520&context=icec.

[24] X. Zenan, Y. Yongzhang, and J. F. Hamilton, "The Computer Simulation of Oil--Flooded Refrigeration Twin-Screw Compressors," *Int. Compress. Eng. Conf.*, no. 537, 1986, [Online]. Available: https://docs.lib.purdue.edu/cgi/viewcontent.cgi?article=1536&context=icec

[25] B. Zhao, M. S. Yang, X. F. Yang, L. Z. Xu, D. K. Gao, and Y. Z. Yuan, "Heat transfer analysis of single screw compressor under oil atomization based on fuzzy random wavelet finite element method," *Int. Commun. Heat Mass Transf.*, vol. 77, pp. 43–48, 2016, doi: 10.1016/j.icheatmasstransfer.2016.07.002.

[26] R. Deipenwisch and K. Kauder, "Oil as a design parameter in screw-type compressors: oil distribution and power losses caused by oil in the working chamber of a screw-type compressor," in *International Conference on Compressor and their Systems,* pp. 49–58, 1999.

[27] M. Graber and A. Brummer, "Influence of liquid in clearances on the operational behaviour of twin screw expanders," in *International Conference on Compressor and their Systems*, no. 12060*,* 2015, doi: 10.1088/1757-899X/90/1/012060.

[28] J. C. Blaise, "Influence of Oil Injection and Pressure," *Int. Compress. Eng. Conf.*, pp. 338–345, 1988, [Online]. Available: https://docs.lib.purdue.edu/cgi/viewcontent.cgi?article=1642&context=icec

[29] Z. He, T. Wang, X. Wang, X. Peng, and Z. Xing, "Experimental investigation into the effect of oil injection on the performance of a variable speed twin-screw compressor," *Energies*, vol. 11, no. 6, 2018, doi: 10.3390/en11061342.

[30] J. Sauls, “Some effects of injection oil on a screw compressor for application in refrigerant R-134a air-conditioning systems,” in *International Conference on Screw Machines*, 2002, no. 1715, pp. 307–318.

[31] M. De Paepe, W. Bogaert, and D. Mertens, “Cooling of oil injected screw compressors by oil atomisation,” vol. 25, pp. 2764–2779, 2005, doi: 10.1016/j.applthermaleng.2005.02.003.

[32] G. Valenti, S. Murgia, G. Contaldi, and A. Valenti, “Experimental evidence of the thermal effect of lubricating oil sprayed in sliding-vane air compressors,” *Case Stud. Therm. Eng.*, vol. 4, pp. 113–117, 2014, doi: 10.1016/j.csite.2014.08.001.

[33] G. Valenti *et al.*, “Thermal effect of lubricating oil in positive-displacement air compressors,” *Appl. Therm. Eng.*, vol. 51, no. 1–2, pp. 1055–1066, 2013, doi: 10.1016/j.applthermaleng.2012.10.040.

[34] G. Bianchi and R. Cipollone, “Experimental assessments on a pressure swirl oil atomizer for positive displacement vane compressors,” vol. 82, pp. 286–293, 2015, doi: 10.1016/j.egypro.2015.12.035.

[35] S. Rezaei, F. Vashahi, G. Ryu, and J. Lee, “On the correlation of the primary breakup length with fuel temperature in pressure swirl nozzle,” *Fuel*, vol. 258, no. 116094, 2019, doi: 10.1016/j.fuel.2019.116094.

[36] J. Xu, “Flow and Separation of the Oil from Compressor Discharge to External Separator,” University of Illinois at Urbana-Champaign, 2019.

[37] P. R. Eiseman, “Grid Generation for Fluid Mechanics Computations”*, Annual Review of Fluid Mechanics*, vol. 17, pp. 487-522, 1985, doi: 10.1146/annurev.fl.17.010185.002415.

[38] A. Kovacevic, “Three-Dimensional Numerical Analysis for Flow Prediction in Positive Displacement Screw Machines,” PhD thesis, City University London, 2002.

[39] D. M. Ingram, D. M. Causon, and C. G. Mingham, “Developments in Cartesian cut cell methods, *Mathematics and Computers in Simulation*, 2003, doi: 10.1016/S0378-4754(02)00107-6.

[40] J. Blazek, “Principles of Grid Generation,” in *Computational Fluid Dynamics: Principles and Applications*, Butterworth-Heinemann, 2005.

[41] V. D. Liseikin, *Grid Generation Methods*, Springer Netherlands, 2009.

[42] A. Kovacevic, "Grid Aspects of Screw Compressor Flow Calculation," ASME Congress, 2000.

[43] J. Voorde Vande and J. Vierendeels, "A Grid Manipulation Algorithm for ALE Calculations in Screw Compressors," *AIAA Computational Fluid Dynamics Conference,*no. 4701, 2005.

[44] A. Kovacevic, N. Stosic, and I. Smith, *Screw Compressors Three Dimensional Computational Fluid Dynamics and Solid Fluid Interaction*, Springer-Verlag Berlin Heidelberg, 2007.

[45] S. Rane and A. Kovacevic, "Algebraic generation of single domain computational grid for twin screw machines . Part I . Implementation," *Adv. Eng. Softw.*, vol. 107, pp. 38–50, 2017, doi: 10.1016/j.advengsoft.2017.02.003.

[46] S. Rane, A. Kovačević, and N. Stošić, "Grid Generation for CFD Analysis and Design of a Variety of Twin Screw Machines," *Designs*, vol. 3, no. 2, p. 30, 2019, doi: 10.3390/designs3020030.

[47] S. Rane, A. Kovacevic, N. Stosic, and M. Kethidi, "Grid deformation strategies for CFD analysis of screw compressors," *Int. J. Refrig.*, vol. 36, no. 7, pp. 1883–1893, 2013, doi: 10.1016/j.ijrefrig.2013.04.008.

[48] "ANSYS Fluent User's Guide-2019 R1," 2019.

[49] G. Bianchi, S. Rane, A. Kovacevic, and R. Cipollone, "Deforming grid generation for numerical simulations of fluid dynamics in sliding vane rotary machines," *Adv. Eng. Softw.*, vol. 112, pp. 180–191, 2017, doi: 10.1016/j.advengsoft.2017.05.010.

[50] S. Rane, A. Kovacevic, N. Stosic, and M. Kethidi, "Grid deformation strategies for CFD analysis of screw compressors," *Int. J. Refrig.*, vol. 36, no. 7, pp. 1883–1893, 2013, doi: 10.1016/j.ijrefrig.2013.04.008.

[51] G. Iaccarino and R. Verzicco, "Immersed boundary technique for turbulent flow simulations ," *Appl. Mech. Rev.*, vol. 56, no. 3, pp. 331–347, May 2003, doi: 10.1115/1.1563627.

[52] M. Mithun, P. Koukouvinis, and I. K. Karathanassis, "Numerical simulation of three-

phase flow in an external gear pump using immersed boundary approach," vol. 72, pp. 682–699, 2019, doi: 10.1016/j.apm.2019.03.022.

[53] H. F. Boysan, D. Choudhury, and M. S. Engelman, "Commercial CFD in the service of industry: The first 25 years," *Notes Numer. Fluid Mech. Multidiscip. Des.*, 2009, doi: 10.1007/978-3-540-70805-6_35.

[54] A. Kovacevic, S. Rane, and N. Stosic, "Modelling of Multiphase Twin Screw Machines," in *International Conference "New Technologies, Development and Applications,"* 2018, pp. 18–32.

[55] A. Kovacevic and S. Rane, "Algebraic generation of single domain computational grid for twin screw machines Part II – Validation," *Adv. Eng. Softw.*, 2017.

[56] S. Rane, "Grid Generation and CFD Analysis of Variable Geometry Screw Machines," PhD thesis, City , University of London, 2015.

[57] A. Kovacevic, S. Rane, N. Stosic, Y. Jiang, M. Furmanczyk, and S. Lowry, "Influence of approaches in CFD Solvers on Performance Prediction in Screw Compressors," *Int. Compress. Eng. Conf.*, no. 1124, 2014.

[58] S. S. Byeon, J. Y. Lee, and Y. J. Kim, "Performance characteristics of a 46 oil-free twin-screw compressor," *Energies*, vol. 10, no. 7, pp. 1–16, 2017, doi: 10.3390/en10070945.

[59] D. Rowinski, Y. Li, and K. Bansal, "Investigations of Automatic Meshing in Modeling a Dry Twin Screw Compressor," in *International Compressor Engineering Conference*, 2018, no. 2621, pp. 1–10.

[60] H. Ding and Y. Jiang, "CFD simulation of a screw compressor with oil injection," in *10th International Conference on Compressors and their Systems*, no. 012020, 2017.

[61] I. Papes, "Computational Analysis of a Twin Screw Expander for Small Scale ORC Systems," PhD thesis, University of Ghent, 2016.

[62] N. Basha, S. Rane, and A. Kovacevic, "Multiphase Flow Analysis in Oil-injected Twin Screw Compressor," in the 3rd World Congress on Momentum, Heat and Mass Transfer, no. 132, 2018, doi: 10.11159/icmfht18.132.

[63] A. A. Barral, R. B. Minussi, and M. V. C. Alves, "Comparison of interface description methods available in commercial CFD software," *J. Appl. Fluid Mech.*, vol. 12, no. 6,

pp. 1801–1812, 2019, doi: 10.29252/JAFM.12.06.29538.

[64] T. Fondelli, A. Andreini, R. Da Soghe, B. Facchini, S. Marta, and L. Cipolla, “Volume of Fluid (VOF) Analysis of Oil-Jet Lubrication for High-Speed Spur Gears Using an Adaptive Meshing Approach,” in ASME Turbo Expo 2015: Turbine Technical Conference and Exposition, no. 42461, 2015, doi: 10.1115/GT2015-42461.

[65] M. Berthhold, H. Morgan, C. Young, and R. Loveday, “Towards Investigationof External Oil Flow From a Journal Bearing in an Epicyclic Gearbox.”, *J. Eng. Gas Turbines Power*, vol. 140, no. 6, 2018, doi: 10.1115/1.4038284 .

[66] Q. Peng, L. Gui, and Z. Fan, “Mechanics Numerical and experimental investigation of splashing oil flow in a hypoid gearbox,” vol. 2060, 2018, doi: 10.1080/19942060.2018.1432506.

[67] L. Li, H. K. Versteeg, G. K. Hargrave, T. Potter, and C. Halse, “Numerical investigation on fluid flow of gear lubrication,” *SAE Int. J. Fuels Lubr.*, 2009, doi: 10.4271/2008-01-1650.

[68] R. D. Reitz and F. V. Bracco, “Mechanisms of breakup of round liquid jets,” *Encycl. Fluid Mech.*, vol. 3, pp. 233–249, 1986.

[69] L. Bravo and C. Kweon, “A Review on Liquid Spray Models for Diesel Engine Computational Analysis,” Report, Army Research Laboratory, 2014.

[70] K. A. Sallam, C. Aalburg, and G. M. Faeth, “Breakup of round nonturbulent liquid jets in gaseous crossflow,” *AIAA J.*, vol. 42, no. 12, pp. 2529–2540, 2004, doi: 10.2514/1.3749.

[71] E. Berrocal, “Multiple scattering of light in optical diagostics of dense sprays and other turbid media,” PhD thesis, Cranfield University, 2006.

[72] Y. Chen *et al.*, “Aerodynamic Breakup and Secondary Drop Formation,” 55th AIAA Aerospace Sciences Meeting, no. 1892, pp. 1–15, 2017, doi: 10.2514/6.2017-1892.

[73] C. Storm and F. Joos, “Comparison of secondary breakup models for droplet-laden compressor flows,” *Int. J. Multiph. Flow*, vol. 116, pp. 125–136, 2019, doi: 10.1016/j.ijmultiphaseflow.2019.04.005.

[74] S. S. Jain, N. Tyagi, R. S. Prakash, R. V. Ravikrishna, and G. Tomar, “Secondary

breakup of drops at moderate Weber numbers: Effect of Density ratio and Reynolds number," *Int. J. Multiph. Flow*, vol. 117, pp. 25–41, 2019, doi: 10.1016/j.ijmultiphaseflow.2019.04.026.

[75] A. Bruemmer, "Keynote presentation on 'Effects of Two-phase Fluids in Twin-screw Expanders", 9th International Conference on Compressor and Refrigeration, 2019.

[76] O. Bratland, *Multiphase Flow Assurance*, Online Available: http://www.drbratland.com/free-book-pipe-flow-1-single-phase-flow-assurance/pipe-flow-1-complete-book-preview/, (accessed Jun. 2021).

[77] M. Gargallo, T. Schulenberg, L. Meyer, and E. Laurien, "Counter-current flow limitations during hot leg injection in pressurized water reactors," *Nucl. Eng. Des.*, vol. 235, no. 7, pp. 785–804, 2005, doi: 10.1016/j.nucengdes.2004.11.002.

[78] C. Vallée, T. Höhne, H. M. Prasser, and T. Sühnel, "Experimental investigation and CFD simulation of horizontal stratified two-phase flow phenomena," *Nucl. Eng. Des.*, vol. 238, no. 3, pp. 637–646, 2008, doi: 10.1016/j.nucengdes.2007.02.051.

[79] P. O'Rourke and A. Amsden, "A Particle Numerical Model for Wall Film Dynamics in Port-Injected Engines," SAE Technical Paper, no. 961961, 1996, doi: 10.4271/961961.

[80] F. Maroteaux, D. Llory, J. F. Le Coz, and C. Habchi, "Liquid film atomization on wall edges - Separation criterion and droplets formation model," *J. Fluids Eng. Trans. ASME*, vol. 124, no. 3, pp. 565–575, 2002, doi: 10.1115/1.1493811.

[81] M. A. Friedrich, "A separation criterion and non-intrusive thickness measurement technique for shear-driven films," PhD thesis, Missouri University of Science and Technology, 2008.

[82] S. Alghoul, C. Eastwick, and D. Hann, "Experimental investigation of a Single Droplet Interaction with Shear Driven Film Division of Fuel and Power Technology , Faculty of Engineering University of Nottingham," in *ILASS, 23rd Annu. Conf. on Liquid Atomization and Spray Systems*, 2010.

[83] I. Owen and D. J. Ryley, "The flow of thin liquid films around corners," *Int. J. Multiph. Flow*, vol. 11, no. 1, pp. 51–62, 1985, doi: 10.1016/0301-9322(85)90005-9.

[84] C. E. Brennen, "Fundamentals of Multiphase Flows," *Technology*, vol. 128, no. 1, pp. 1–18, 2005, doi: 10.1007/s11214-006-9083-0.

[85] J. C. Lasheras, E. V Villermaux, and E. J. Hopfinger, “Break-up and atomization of a round water jet by a high-speed annular air jet,” *J. Fluid Mech.*, vol. 357, pp. 351–379, 1997.

[86] D. B. Harmon, “Drop sizes from low speed jets,” *J. Franklin Inst.*, vol. 259, no. 6, pp. 519–522, 1955, doi: 10.1016/0016-0032(55)90098-3.

[87] A. C. Merrington and E. G. Richardson, “The break-up of liquid jets,” *Proc. Phys. Soc.*, vol. 59, no. 1, pp. 1–13, 1947, doi: 10.1088/0959-5309/59/1/302.

[88] M. M. Elkotb, “Fuel atomization for spray modelling,” *Prog. Energy Combust. Sci.*, vol. 8, no. 1, pp. 61–91, 1982, doi: 10.1016/0360-1285(82)90009-0.

[89] Q. Lin, L. Fan, and G. Jin, “Theoretical analysis and experimental study of oil atomizing in a single screw compressor,” *Int. J. J. Xi’an Pet. Institute(Natural Sci. Ed.*, vol. 15, no. 2, pp. 41–44, 2000.

[90] A. Prosperetti and G. Tryggvason, Computational methods for multiphase flow, Cambridge University Press, 2007.

[91] B. Rapp, *Microfluidics: Modeling, Mechanics and Mathematics*. Elsevier, 2017.

[92] M. Mayank, E. Sheung-Chi Fan, and M. Bussmann, “Adaptive VOF with curvature-based refinement,” *Int. J. Numer. Methods Fluids*, vol. 65, no. April 2007, pp. 693–712, 2007, doi: 10.1002/fld.

[93] D. Zuzio, J. L. Estivalèzes, and B. DiPierro, “An improved multiscale Eulerian–Lagrangian method for simulation of atomization process,” *Comput. Fluids*, vol. 176, pp. 285–301, 2018, doi: 10.1016/j.compfluid.2016.12.018.

[94] H. Braess and P. Wriggers, “Arbitrary Lagrangian Eulerian finite element analysis of free surface flow,” *Comput. Methods Appl. Mech. Eng.*, vol. 190, no. 1–2, pp. 95–109, 2000, doi: 10.1016/S0045-7825(99)00416-8.

[95] V. V. Buwa, D. S. Deo, and V. V. Ranade, “Eulerian-Lagrangian simulations of unsteady gas-liquid flows in bubble columns,” *Int. J. Multiph. Flow*, vol. 32, no. 7, pp. 864–885, 2006, doi: 10.1016/j.ijmultiphaseflow.2006.02.017.

[96] M. Jamialahmadi, H. Müller-Steinhagen, and M. R. Izadpanah, “Pressure drop, gas hold-up and heat transfer during single and two-phase flow through porous media,”

International Journal of Heat and Fluid Flow, vol. 26. pp. 156–172, 2005, doi: 10.1016/j.ijheatfluidflow.2004.07.004.

[97] T. F. Leung, C. P. T. Groth, and J. T. C. Hu, "Evaluation of an eulerian-lagrangian spray atomization (ELSA) model for nozzle flow: Modeling of coupling between dense and disperse regions," *47th AIAA Thermophys. Conf. 2017*, no. June, pp. 1–14, 2017, doi: 10.2514/6.2017-4352.

[98] D. J. Schmidt, W. Kvasnak, and G. Ahmadi, "A model for fuel spray formation with atomizing air," *Fluids*, vol. 4, no. 1, pp. 1–18, 2019, doi: 10.3390/fluids4010020.

[99] J. K. Dukowicz, "A particle-fluid numerical model for liquid sprays," *J. Comput. Phys.*, vol. 35, no. 2, pp. 229–253, 1980, doi: 10.1016/0021-9991(80)90087-X.

[100] C. W. Hirt and B. D. Nichols, "Volume of Fluid (VOF) Method for the Dynamics of Free Boundaries," *J. Comput. Phys.*, vol. 225, pp. 201–225, 2004, doi: 10.1016/0021-9991(81)90145-5.

[101] H. Vasuthevan and A. Brummer, "Multiphase-flow simulation of a rotating rectangular profile within a cylinder in terms of hydraulic loss mechanisms," 2018, doi: 10.1088/1757-899X/425/1/012002.

[102] C. Shao, K. Luo, M. Chai, and J. Fan, "Sheet, ligament and droplet formation in swirling primary atomization," *AIP Adv.*, vol. 8, no. 4, 2018, doi: 10.1063/1.5017162.

[103] F. Evrard, F. Denner, and B. Van Wachem, "A hybrid Eulerian-Lagrangian approach for simulating liquid sprays," ILASS–Europe 2019, 29th Conference on Liquid Atomization and Spray Systems, pp. 2–4, 2019.

[104] M. Sami *et al.*, "Best Practices in the numerical modelling of liquid atomization processes," in *ILASS, 30th Annu. Conf. on Liquid Atomization and Spray Systems*, 2019

[105] X. Li and M. C. Soteriou, "High fidelity simulation and analysis of liquid jet atomization in a gaseous crossflow at intermediate weber numbers," *Phys. Fluids*, vol. 28, no. 8, 2016, doi: 10.1063/1.4959290.

[106] L. Qian, J. Lin, and F. Bao, "Numerical models for viscoelastic liquid atomization spray," *Energies*, vol. 9, no. 12, 2016, doi: 10.3390/en9121079.

[107] M. Ul Haq, R. Latif, I. Shafi, and A. Javaid, "Modelling primary atomization and its

effects on spray characteristics under heavy duty diesel engine condition," *Proc. 21st Australas. Fluid Mech. Conf. AFMC 2018*, pp. 4–7, 2018.

[108] "ANSYS FLUENT theory guide- Release 19.0," *ANSYS, Inc.* 2018, doi: 10.1016/0140-3664(87)90311-2.

[109] N. Stosic, "'N' Rotor Profile," Patent, GB9610289.2, 1996.

[110] S. Patankar, *Numerical Heat Transfer and Fluid Flow (Hemisphere Series on Computational Methods in Mechanics and Thermal Science)*, CRC Press, 1980.

[111] *ANSYS Meshing User's Guide-Release 13.0*. Canonsburg, PA 15317: Ansys Inc., 2010.

[112] "ANSYS CFX-Solver Theory Guide," 2006.

[113] "ISO 1217:2009 Displacement compressors — Acceptance tests," 2009. [Online]. Available: https://www.iso.org/obp/ui/#iso:std:iso:1217:en.

[114] "BS 1042- 1.4:1992 Measurement of fluid flow in closed conduits," BS ISO/TR 9464:1998, 2019.

[115] J. H. Arnold, "Vapor Viscosities and the Sutherland Equation," *J. Chem. Phys.*, vol. 1, no. 2, p. 170, 1933, doi: 10.1063/1.1749269.

[116] "A Summary of Error Propagation," *Harvard University*, 2013. http://ipl.physics.harvard.edu/wp-uploads/2013/03/PS3_Error_Propagation_sp13.pdf (accessed May 09, 2018).

[117] A. Kovacevic, N. Stosic, and I. Smith, *Screw Compressors: Three Dimensional Computational Fluid Dynamics and Solid Fluid Interaction*. Springer Verlag, Berlin, 2005.

[118] M. Wörner, "Numerical modeling of multiphase flows in microfluidics and micro process engineering: A review of methods and applications," *Microfluidics and Nanofluidics*. 2012, doi: 10.1007/s10404-012-0940-8.

[119] D. L. Youngs, "Time-dependent multi-material flow with large fluid distortion.," *Numerical Methods in Fluid Dynamics*, Academic Press , 1982.

[120] O. Ubbink and R. I. Issa, "A Method for Capturing Sharp Fluid Interfaces on Arbitrary Meshes," J. Comput. Phys., vol. 50, pp. 26–50, 1999.

Appendix 1 Mathematical Modelling Approach

Appendix 1.1 Thermodynamic chamber models

Stosic et. al [117] have presented screw machine as a thermodynamic system in which the mass flow rate varies with time. For this thermodynamic system, the equations of conservation of energy and mass can be written and computed in terms of rotational angle. These equations can be written as below.

The conservation of internal energy:

$$\omega\left(\frac{dU}{d\theta}\right) = \dot{m}_{in}\dot{h}_{in} - \dot{m}_{out}\dot{h}_{out} + Q - \omega p\frac{dV}{d\theta} \tag{25}$$

where U is the internal energy, ω is the compressor rotational speed, θ is the angle of rotation of the main rotor, h is specific enthalpy, $\dot{m}$ is mass flow rate, Q is the heat transfer between the fluid and the compressor surrounding, p and V are the fluid pressure and local volume of the compressor working chamber.

The subscripts in and out denote the fluid inflow and outflow.

The fluid total enthalpy inflow and outflow can be elaborated according to the equation (26) and (27).

$$\dot{m}_{in}h_{in} = \dot{m}_{suc}h_{suc} + \dot{m}_{l,g}h_{l,g} + \dot{m}_{oil}h_{oil} \tag{26}$$

where subscripts *l, g* denote leakage gain and *suc* is the suction condition.

$$\dot{m}_{out}h_{out} = \dot{m}_{dis}h_{dis} + \dot{m}_{l,l}h_{l,l} \tag{27}$$

where subscripts *l, l* denote leakage loss and *dis* is the discharge condition.

The conservation of mass:

$$\omega\frac{d\dot{m}}{d\theta} = \dot{m}_{in}h_{in} - \dot{m}_{out}h_{out} \tag{28}$$

The fluid total enthalpy inflow and outflow can be elaborated according to the equation (29) and (30)

$$\dot{m}_{in}h_{in} = \dot{m}_{suc}h_{suc} + \dot{m}_{l,g}h_{l,g} + \dot{m}_{oil}h_{oil} \tag{29}$$

$$\dot{m}_{out}h_{out} = \dot{m}_{dis}h_{dis} + \dot{m}_{l,l}h_{l,l} \tag{30}$$

Each of the mass flow rate should satisfy the continuity equation (32). (31)

$$\dot{m} = \rho\omega A \tag{32}$$

where ω denotes fluid velocity, ρ is fluid density and A is the flow cross-sectional area.

A is obtained from the compressor geometry and it is considered as a periodic function of the angle of rotation θ. The suction port area can be defined by the equation (33).

$$A_{suc} = A_{suc,0}\sin(\pi\frac{\theta}{\theta_{suc}}) \tag{33}$$

where suc means the starting value of θ at the moment of the suction port opening, and $A_{suc,0}$ denotes the maximum value of the suction port cross-section area. The suction ends at $\theta = 0$.

Likewise, the discharge port area can be defined according to the equation (34).

$$A_{dis} = A_{dis,0}\sin(\pi\frac{\theta - \theta_c}{\theta_e - \theta_s}) \tag{34}$$

where subscript e denotes the end of discharge, c denotes the end of compression and $A_{dis,0}$ stands for the maximum value of the discharge port cross-sectional area.

Equations of suction and discharge port area can be substituted in the equation (29) and (30) to obtain $\dot{m}_{in}$ and $\dot{m}_{out}$. $\dot{m}_l$ could be obtained through assuming leakage areas to be rectangular shaped and the mass flow of the leaking fluid can be expressed by the continuity equation.

$$\dot{m}_l = \mu_l\rho_l\omega_l A_g \tag{35}$$

where ρ, ω and μ are density, velocity and flow coefficient of the leaking gas. $A_g = l_g\delta_g$, where l_g is the clearance length and δ_g is the sealing line.

The mass flow rate of oil can be written in the form shown in equation (36). The oil to gas mass ratio is considered as a convenient parameter to define the injected oil mass flow and the injected is assumed to be uniformly distributed.

$$\dot{m}_{oil} = \frac{\dot{m}_{oil}}{\dot{m}_{gas}}\dot{m}\frac{z_1}{2\pi} \tag{36}$$

To account for cooling, heat exchange with the gas and oil is determined from the differential equation form of the energy balance shown in equation (37).

$$\frac{dT_{oil}}{d\theta} = \frac{h_{oil}A_{oil}(T_{gas} - T_{oil})}{\omega m_{oil}c_{oil}} \tag{37}$$

Using, $Nu = 2 + 0.6Re^{0.6}Pr^{0.33}$ and integration of the equation (37), gives the droplet temperature at each time step.

$$T_{oil} = \frac{T_{gas} - kT_{oil,p}}{1 + k} \tag{38}$$

$T_{oil,p}$ is the oil droplet temperature at the previous time step.

k is the non-dimensional time constant which can be written according to the equation (39).

$$k = \frac{\omega m_{oil}c_{oil}}{h_{oil}A_{oil}\Delta\theta} \tag{39}$$

Considering oil droplets as spherical shaped with Sauter mean diameter, *k* can be further written as,

$$k = \frac{\omega d_s c_{oil}}{6h_{oil}\Delta\theta} \tag{40}$$

If k tends to zero, the oil and gas temperatures will be equal. However, for the finite values of *k*, the gas and oil temperatures will differ. This approach is based on the assumption that the oil droplet time is smaller than the droplet travelling through the gas before it hits the rotor or casing wall, or reaches the discharge port. This means that the heat exchange between gas and oil is completed during the compression process. In order to fulfil this prerequisite, the oil Sauter mean diameter sizes are assumed to be as small as 50μ.

Appendix 1.2 Wavelet finite element model

Heat transfer of injected oil and gas within a single screw compressor can be established through Hermitian wavelet function, expressed as follows [25],

$$\emptyset(t) = (1 + it - t^2)\frac{1}{\sqrt{2\pi}}e^{-\frac{t^2}{2}} \tag{41}$$

The Hermitian wavelet functions $\emptyset_1(\alpha), \emptyset_2(\beta)$ and $\emptyset_3(\alpha)$ is used to construct the multi-resolution subspaces $\{V_{1j}\}$, $\{V_{2j}\}$ and $\{V_{3jk}\}$, the tensor product of $\{V_{1j}\}$, $\{V_{2j}\}$and $\{V_{2k}\}$form the higher order space $\{V_j\}$, and the corresponding expression is expressed by equation (42).

$$V_j = V_{1j} \otimes V_{2j} \otimes V_{3k} \tag{42}$$

where $\{V_j\}$ denotes the higher space, *j = 0,1,..., N-1*; $\otimes$ denotes Kronecker symbol, α, β and γ denote the local coordinates (x,y) is expressed as follows,

$$\alpha = \frac{x - x_1}{x_2 - x_1} \tag{43}$$

$$\beta = \frac{y - y_1}{y_2 - y_1} \tag{44}$$

$$\gamma = \frac{z - z_1}{z_2 - z_1} \tag{45}$$

where x_1 and x_2 denote the maximum and minimum values in x direction, where y_1 and y_2 denote the maximum and minimum values in y direction, z_1 and z_2 denote the maximum and minimum values in z direction.

The Hermitian wavelet scale function on subspace is defined by,

$$\vec{\emptyset}_1 = \{\psi_1(\alpha), \psi_1(\alpha + 1), \dots, \psi_1\big(\alpha + (N - 2)\big)\} \tag{46}$$

$$\vec{\emptyset}_2 = \{\psi_2(\beta), \psi_2(\beta + 1), \dots, \psi_2\big(\alpha + (N - 2)\big)\} \tag{47}$$

$$\vec{\emptyset}_3 = \{\psi_3(\gamma), \psi_3(\gamma + 1), \dots, \psi_3\big(\alpha + (N - 2)\big)\} \tag{48}$$

The Hermitian wavelet scale function on higher order space $\{V_j\}$ can be expressed as follows,

$$\vec{\emptyset} = \vec{\emptyset}_1 \otimes \vec{\emptyset}_2 \otimes \vec{\emptyset}_3 \tag{49}$$

The temperature function T(α, β,γ) of screw compressor can be defined by,

$$T(\alpha, \beta, \gamma) = \vec{\emptyset}\vec{b} \tag{50}$$

where $\vec{b} = (b_0, b_1, \dots, b_{-(N-2)})$ denotes Hermitian wavelet coefficient vector.

Appendix 2 Grids for Rotating Domains

Appendix 2.1 Grid types

Algebraic grid generation is the prominently available technique for generating computational grids for twin-screw machines pioneered by Kovacevic [38]. This technique is classified as Rotor-Casing (R-C) method. In this grid case, the rotor grid is generated in the ‘O' form, which requires a flow domain between the rotors and the casing in two blocks for the male and female rotor. The division between male and female rotor is achieved through the rack to split them into two ‘O’ domains. Boundary nodes are positioned on the rotor domains; these nodes retain a relative position with the rotor and rotate together with the rotor. The flow chart for the R-C method is shown in Figure 80. This method is robust, but it introduces a non-conformal interface. Therefore, this method improved further by Rane to resolve undesired features caused by the R-C method and this improved method is called Casing-Rotor (C-R) type [6].

With the C-R grid, the rotor blocks are stationary, and the nodes slide on the rotor surface. Equidistant distribution is applied where several points are distributed on the casing and the rack. This leads to a conformal interface, followed by regularising the rotor profile distribution using analytical control function or background blocking distribution [45].

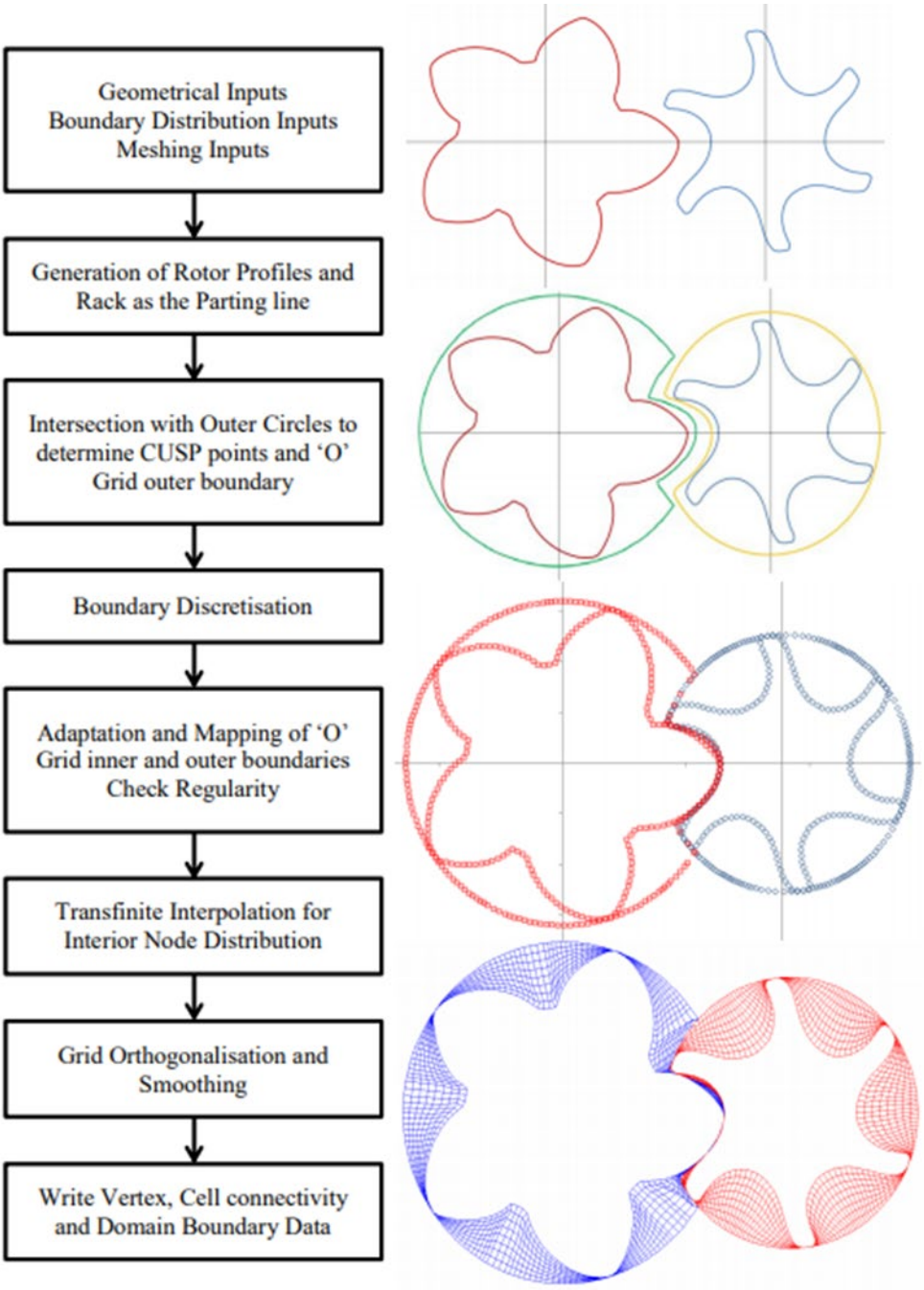

Figure 80. Simplified flow chart for Algebraic rotor grid generation [56].

Appendix 2.2 Benchmarking case

Within C-R conformal mesh, male and female rotor interfaces are merged to form C-R single domain mesh. In this section, R-C non-conformal, C-R conformal and C-R single domain mesh are assessed for their accuracy in a real compressor case where validations can be conducted with the experimental data.

Figure 81 shows the grids generated with the C-R and R-C techniques. At the interlobe region, there is a clear connection with for C-R grid type and no connection between the nodes for the R-C grid type. These meshing features are available in the computer code called SCORG.

The grid divisions obtained for different grid types are shown in Table 34. The analysis is carried out in ANSYS CFX for the air compressor mentioned in Section 4.3.1 of Chapter 4. The details of compressor specification, boundary conditions and numerical setup for the analysis are mentioned in Table 5, Table 6 and Table 7 of the same chapter.

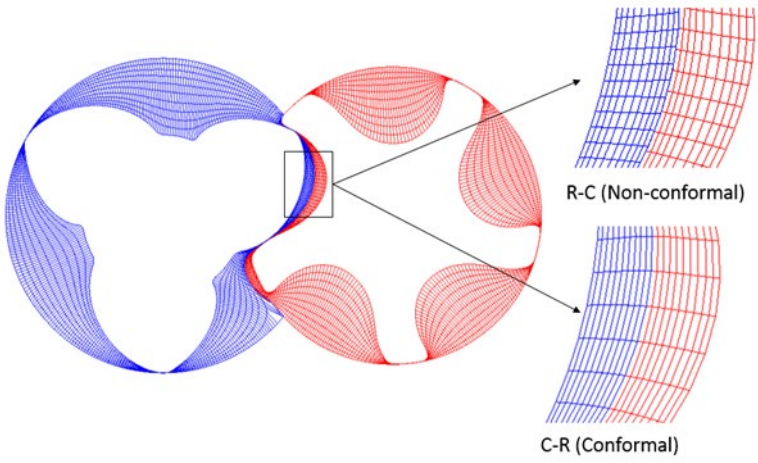

Figure 81. Difference in node connections for grid types.

Table 34. Rotor divisions for various grid types.

Grid Type	Radial	Angular	Circumferential		
			Total	Interlobe	Casing
R-C	10	50	350	50	300
C-R (Conformal)	10	50	350	50	300
C-R (Single Domain)	10	50	350	50	300

Appendix 2.3 Influence of grid types

Figure 82 and Figure 83 shows the variation in pressure according to the angle of male rotor rotation in the compression chamber. Under compression is visible at 8000 rpm and 6000 rpm.

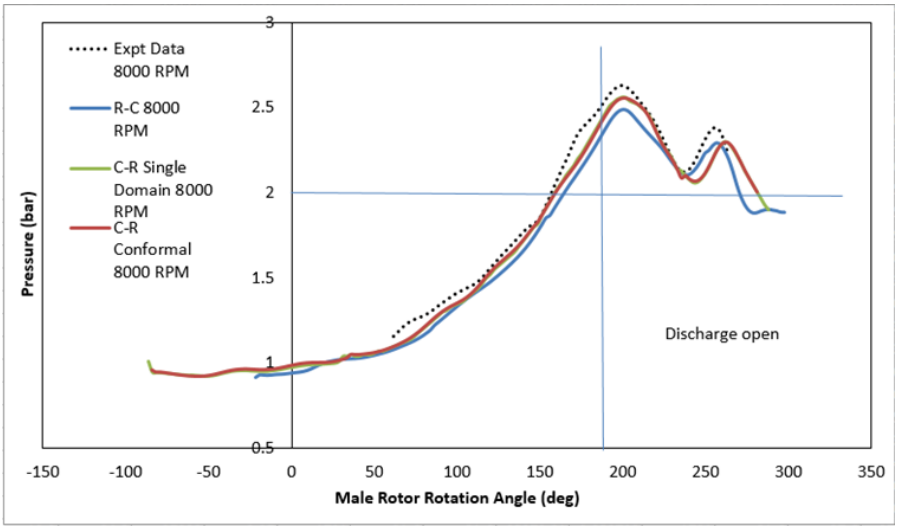

Figure 82. Pressure versus male rotor angle for 8000 rpm.

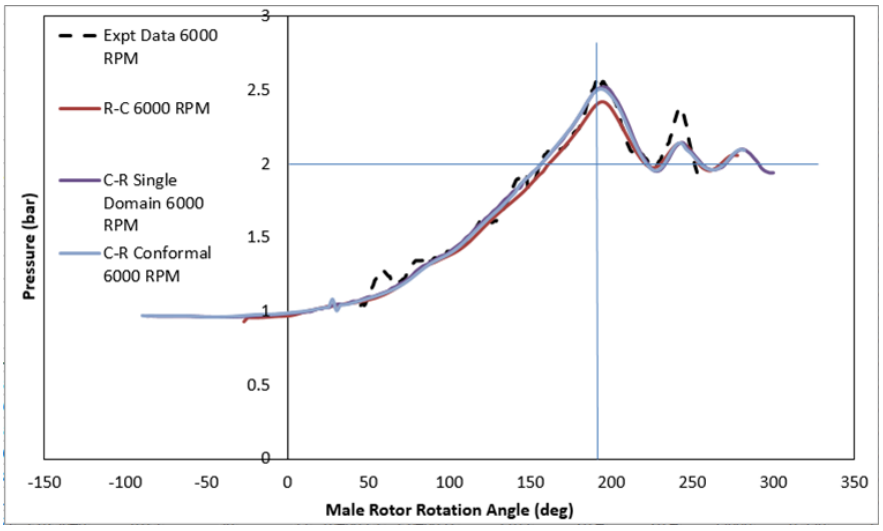

Figure 83. Pressure versus male rotor angle for 6000 rpm.

The CFD predictions match well with the experimental data. Pressure predicted by the C-R method is close to experimental data for 8000 and 6000rpm, but with the R-C method, there is higher leakage loss due to the non-conformal interface. At the non-conformal interface, there occurs an interpolation which leads to numerical dissipation. Therefore, with the R-C grid type,

the peak pressures are lower compared to the experimental data. C-R Conformal or Single Domain is a recommended grid type.

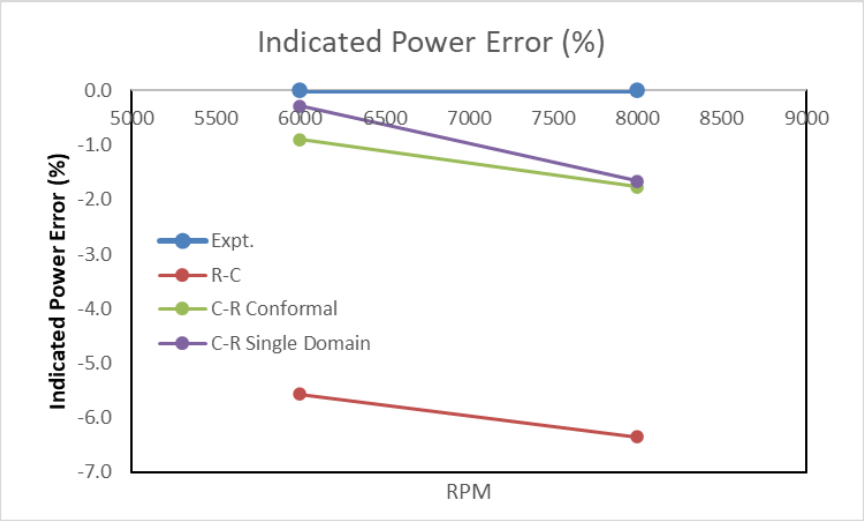

Figure 84. Error percentage with indicated power for various grid types compared with measured data.

Figure 84 shows the error percentage in predicting indicated power compared to the measured value with speed. In comparison to 8000 rpm, the predicted values for 6000 rpm lie closer to the experimental data. C-R single domain matches with the experimental data by -1.66% at 8000 rpm and by -0.28% at 6000 rpm. Whereas, R-C matches the experimental data by a higher error percentage of -6.35% at 8000 rpm and -5.57% at 6000 rpm.

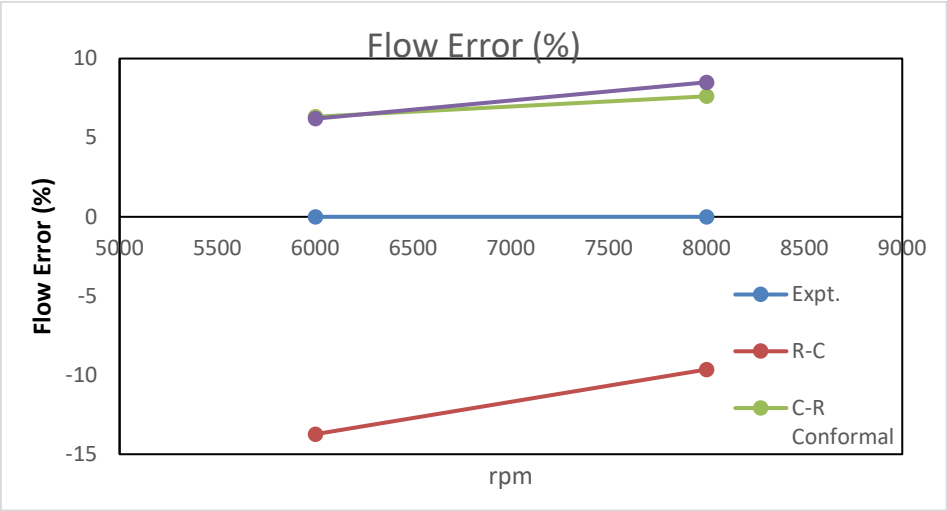

Figure 85. Error percentage with air flow rate for various grid types compared with measured data.

Figure 85 shows the error percentage in flow rate compared to the experimental data against male rotor shaft speed. Again, C-R grid types of the conformal and single domain show better prediction in values as they can capture flow across the leakages. R-C grid type under predicts the flow rate due to numerical error in calculating fluxes over the interface.

Appendix 2.4 Summary

In this chapter, grid generation techniques for twin-screw machines are explored. Currently, available grid types for screw machines in SCORG software are R-C non-conformal, C-R conformal and C-R single domain. These grids are tested for an air compressor rotating at 6000 rpm and 8000 rpm. The C-R grid types of conformal interface and single domain have shown both indicated power and air flow rate closer to experimental data. Accuracy with C-R type is attributed to the better resolution of fluxes at the male-female rotor interface. Therefore, the C-R type will be used for analysis where it is expected to achieve better mass balance for the air and oil phase.

Appendix 3 Two-Phase Computational Methods

In addition to the complexities of a single-phase flow modelling such as non-linearities, a transition to turbulence and instabilities, modelling of two-phase flows includes additional complexities such as motion and deformation of an interface, non-equilibrium effects and momentum interaction between phases. These complexities affect the stability of the solver. Particularly for oil-injected twin-screw compressor, key challenges faced are:

- The sudden change of cell sizes due to rotor rotation, if not treated properly, can lead to abrupt changes in the physical properties of the working fluid, such as a localised and unphysical increase in pressure and temperature. This may affect the stability of the solution.
- Air and oil may have a density ratio difference up to three orders of magnitude. Numerical simulations with higher density ratios tend to have sharp discontinuities across the interface leading to solver instability. These discontinuities and instability are further pronounced if one of the fluid phases is highly compressible such as air.

Oil injection in an air compressor is a case of gas-liquid flow. Gas-liquid flows in Ansys Fluent can be resolved with Eulerian-Eulerian, Volume of fluids (VOF), mixture and Euler-Lagrangian approach. The Euler-Lagrangian approach is not considered suitable for modelling oil-injected compressor as initial data on oil droplet sizes is not available, and the oil volume fraction loading is higher than 12% which is the limit specified by CFD vendors [108].

The governing equations for Eulerian-Eulerian, VOF and mixture model are detailed below. These models assume that both oil and gas are Newtonian immiscible fluids. The assumption on immiscibility holds true for this study as air and oil are normally immiscible in a typical oil-injected air compressor. However, for applications that include compression of organic fluids, suitable assumptions need to be made when using the two-phase models [118].

Appendix 3.1 Governing equations for two-phase models

This section describes the governing equations for two-phase models. All these equations are taken from the Ansys Fluent theory guide [108].

i. Eulerian-Eulerian model

Eulerian-Eulerian model is the most elaborate model compared to the VOF and mixture model as it solves continuity, momentum and energy for each of the air and oil phase. Also, the air and oil phase in the domain are treated as interpenetrating continua.

Continuity equation:

$$\frac{\partial(\alpha_{air}\rho_{air})}{\partial t} + \nabla.(\alpha_{air}\rho_{air}\vec{v}_{air}) = 0 \tag{51}$$

$$\frac{\partial(\alpha_{oil}\rho_{oil})}{\partial t} + \nabla.(\alpha_{oil}\rho_{oil}\vec{v}_{oil}) = 0 \tag{52}$$

Momentum equation:

$$\frac{\partial(\alpha_{air}\rho_{air}\vec{v}_{air})}{\partial t} + \nabla.(\alpha_{air}\rho_{air}\vec{v}_{air}\vec{v}_{air}) = -\alpha_{air}\nabla P + \nabla.\overline{\overline{\tau_{air}}} + \alpha_{air}\rho_{air}\vec{g} + \vec{R}_{oil-air} \tag{53}$$

$$\frac{\partial(\alpha_{oil}\rho_{oil}\vec{v}_{oil})}{\partial t} + \nabla.(\alpha_{oil}\rho_{oil}\vec{v}_{oil}\vec{v}_{oil}) = -\alpha_{oil}\nabla P + \nabla.\overline{\overline{\tau_{oil}}} + \alpha_{oil}\rho_{oil}\vec{g} + \vec{R}_{air-oil} \tag{54}$$

The terms on the left are transient and convection terms. The terms on the right are pressure gradient shared between the phases, stress-strain, gravity and the interaction between the air-oil phase.

Interphase momentum transfer $\vec{R}_{air-oil}$ can be written as

$$\vec{R}_{air-oil} = [\frac{\alpha_{oil}\alpha_{air}\rho_{air}f}{\tau_{air}}(\vec{v}_{air} - \vec{v}_{oil})] \tag{55}$$

$$f = \frac{C_D Re}{24} \tag{56}$$

f is a friction factor depending on the drag coefficient C_D as 0.44 and Re is the Reynolds number.

Energy equation:

$$\frac{\partial}{\partial t}(\alpha_{air}\rho_{air}h_{air}) + \nabla.\left(\alpha_{air}(\rho_{air}\overrightarrow{u_{air}}h_{air} - \delta\nabla T)\right) = Q_{oil-air} \quad (57)$$

$$\frac{\partial}{\partial t}(\alpha_{oil}\rho_{oil}h_{oil}) + \nabla.\left(\alpha_{oil}(\rho_{oil}\overrightarrow{u_{oil}}h_{oil} - \delta\nabla T)\right) = Q_{air-oil} \quad (58)$$

$Q_{oil-air}$ or $Q_{air-oil}$ is the interfacial heat transfer between the air and oil phase and can be defined according to the equations (59) and (60).

$$Q_{oil-air} = h(T_{oil} - T_{air}) \quad (59)$$

$$Q_{air-oil} = h(T_{air} - T_{oil}) \quad (60)$$

Here h is the interfacial heat transfer coefficient, and T is the temperature. h can be defined according to the equation (61) with Nusselts number (Nu) as 50 for the simulation case study in Chapter 4 of this thesis.

$$h = \frac{NuK}{L} \quad (61)$$

L is the characteristic length, and K is the thermal conductivity of the respective phase.

ii. Volume of Fluid- VOF model

The form of the VOF model used in this study is developed by Hirt and Nichols [100]. The VOF model tracks the interface between the air and oil phase by solving the conservation equation for the volume fraction of the oil phase, as shown in equation (62). In each cell, $\alpha_{oil} = 1$ represents pure oil phase and $\alpha_{oil} = 0$ represents pure air phase. If $0 < \alpha_{oil} < 1$ it means that air-oil interface exists in that cell. In that case, the volume fraction of the air phase can be determined by the constraint shown in equation (63).

$$\frac{1}{\rho_{oil}}\left(\frac{\partial(\alpha_{oil}\rho_{oil})}{\partial t} + \nabla.(\alpha_{oil}\rho_{oil}\vec{v}) = 0\right. \quad (62)$$

$$\alpha_{oil} + \alpha_{air} = 1 \quad (63)$$

In the VOF model, the flow variables are volume fraction averaged in each computational cell. For instance, equation (64) shows the density ρ of the air-oil two-phase flow. Similarly, viscosity and thermal conductivity are volume fraction averaged for an air-oil mixture. The enthalpy and temperature in a computational cell are mass fraction averaged. They are unique for each phase in the mixture but could be shared depending on the methods used in a

multiphase model to define an interface between the phases within a computational cell. This is based on the volume fraction of each fluid in the computational cell and the surrounding cells.

Density of the mixture:

$$\rho = \alpha_{air}\rho_{air} + \alpha_{oil}\rho_{oil} \quad (64)$$

These flow variables are then used in a single set of governing equations for continuity, momentum and energy as follows:

Continuity:

$$\frac{\partial \rho}{\partial t} + \nabla.(\rho\vec{v}) = 0 \quad (65)$$

Momentum:

$$\frac{\partial}{\partial t}(\rho\vec{v}) + \nabla.(\rho\vec{v}\vec{v}) = -\nabla p + \nabla.[\mu(\nabla\vec{v} + \nabla\vec{v}^T)] + \rho\vec{g} + \vec{F} \quad (66)$$

The transient and convection terms are located on the left-hand side of the equation (66), while the terms on the right-hand side describe the pressure gradient, stress-strain, gravity and external body forces.

Energy:

$$\frac{\partial}{\partial t}\sum_{k=1}^{n}(\alpha_k\rho_k h_k) + \nabla.\left(\alpha_k(\rho_k\overrightarrow{u_k}h_k - \delta\nabla T)\right) = 0 \quad (67)$$

Where *k* represents the air and oil phase.

iii. Mixture model

The mixture model differs from the VOF model by including an additional term on interphase momentum transfer in the momentum equation and treating the air-oil phase to be interpenetrating.

The flow variables density ρ and viscosity μ are volume fraction averaged in each computational cell. For instance, equation (68) shows the density ρ of the air-oil two-phase flow.

Density of the mixture:

$$\rho_m = \alpha_{air}\rho_{air} + \alpha_{oil}\rho_{oil} \tag{68}$$

Continuity:

$$\frac{\partial \rho_m}{\partial t} + \nabla.(\rho_m \vec{v}_m) = 0 \tag{69}$$

$$\vec{v}_m = \sum_{k=1}^{n} \frac{\alpha_k \rho_k \vec{v}_k}{\rho_m} \tag{70}$$

Where *k* represents the air and oil phase.

Momentum:

$$\frac{\partial}{\partial t}(\rho_m \overrightarrow{v_m}) + \nabla.\ (\rho_m \overrightarrow{v_m}\overrightarrow{v_m}) = -\nabla p + \nabla.\left[\mu_m\left(\nabla \overrightarrow{v_m} + \nabla \overrightarrow{v_m^T}\right)\right] + \rho_m \vec{g} + \nabla.\left(\sum_{k=1}^{n} \alpha_k \rho_k \overrightarrow{v_{dr,k}}\overrightarrow{v_{dr,k}}\right) \tag{71}$$

$$\vec{v}_{dr,\mathrm{k}} = \vec{v}_k - \vec{v}_m \tag{72}$$

$$\vec{v}_k = \frac{\tau}{f}\frac{(\rho_{air} - \rho_m)}{\rho_{air}}\vec{\alpha} \tag{73}$$

$\vec{v}_{dr,\mathrm{k}}$ is the drift velocity between the phases. f is a friction factor depending on the drag coefficient C_D as 0.44 as in equation (56)

The energy equation for the Mixture model is the same as the VOF model (equation (67)).

Appendix 3.2 Interface reconstruction and advection for the VOF model

After solving the volume fraction and transport equations, the VOF model algorithm must reconstruct the interface between the phases and propagate such an interface. Within the reconstruction of an interface, various schemes are available in a commercial solver Ansys Fluent. These schemes are geometric reconstruction, Compressive interface capturing scheme for arbitrary meshes (CICSAM), compressive, High resolution interface capturing (HRIC) and donor-acceptor scheme. The basic structure is shown in Figure 86. A simple reconstruction of the interface with donor-acceptor and geometric reconstruction is shown in Figure 87.

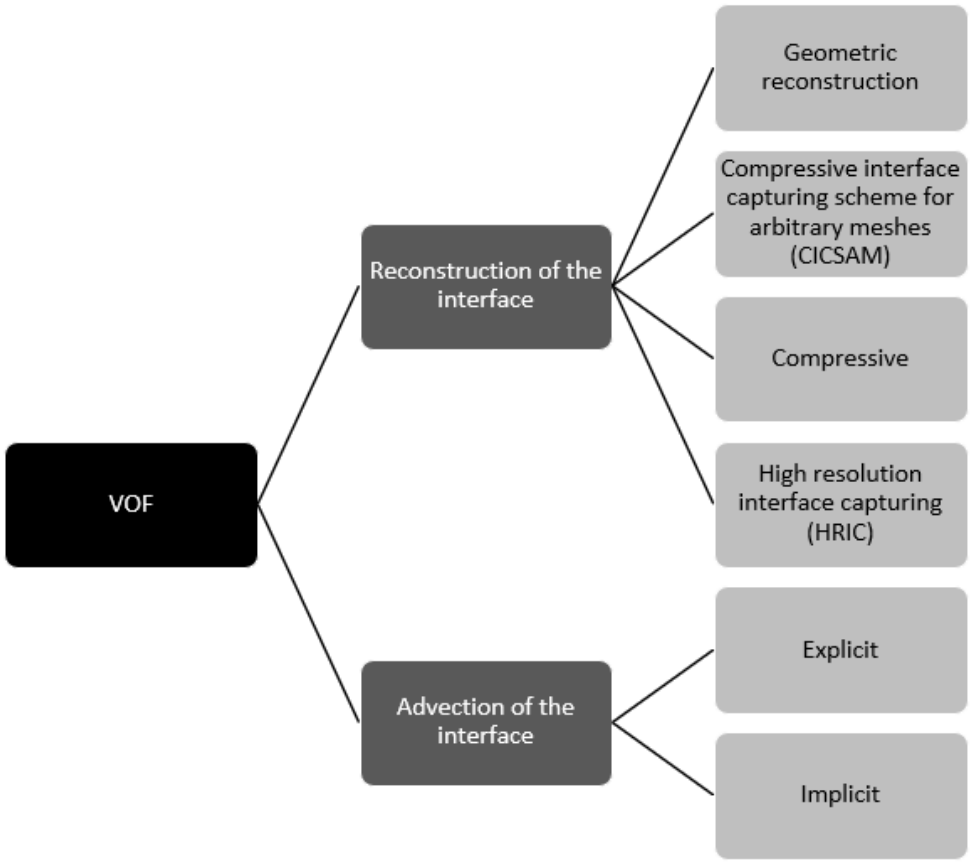

Figure 86. Interface reconstruction and advection schemes with VOF approach.

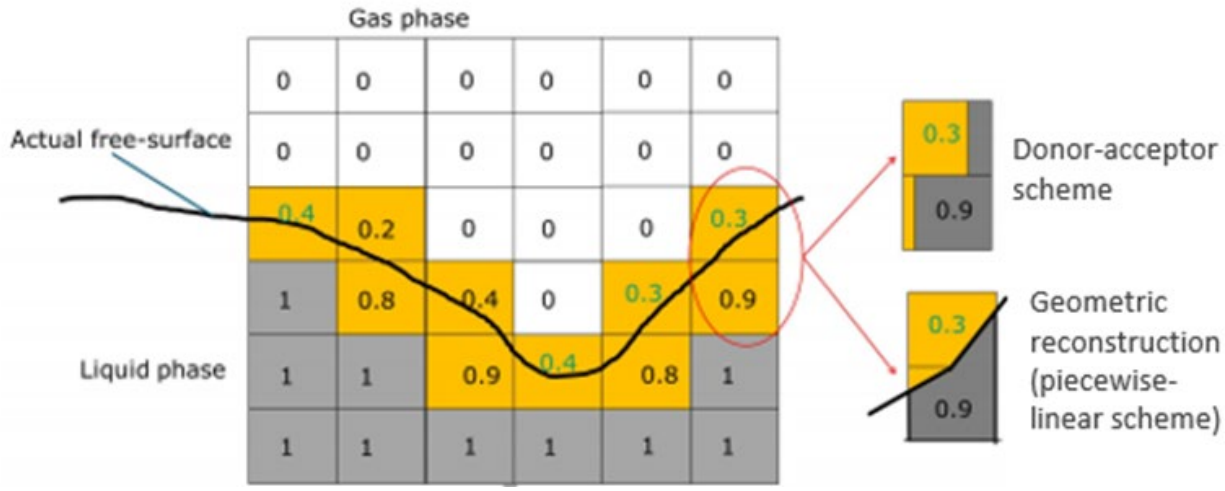

Figure 87. Reconstruction of interface for volume fraction in computational cells [21].

The geometric reconstruction scheme represents the interface between the fluids using a piecewise-linear approach. This scheme assumes that the interface between two fluids has a linear slope and uses this linear shape to calculate the advection of the fluid through the cell faces [119]. The CICSAM and HRIC are both high-resolution schemes and are similar to the geometric reconstruction scheme. Still, they focus on discretising the convective term to prevent artificial smearing due to numerical diffusion [120]. The compressive scheme is a second-order reconstruction scheme based on the slope limiter. The scheme is suitable for complex flows and therefore selected for use in this thesis.

$$\emptyset_f = \emptyset_d + \beta \nabla \emptyset_d \quad (74)$$

Here, $\emptyset_f$ is the face VOF value, $\emptyset_d$ is the donor cell VOF value, β is the slope limiter value and $\nabla \emptyset_d$ is the donor cell VOF gradient value.

The volume fraction equation (equation (62)) can be solved either through implicit or explicit time discretisation. The implicit equation requires the volume fraction values at the current time step. A standard scalar transport equation is solved iteratively for each of the secondary-phase volume fractions at each time step. Whereas for an explicit approach, interpolation schemes are applied for the volume fraction values computed at the previous time step.

Implicit approach:

$$\frac{\alpha_q^{n+1}\rho_q^{n+1} - \alpha_q^n \rho_q^n}{\Delta t} V + \sum_f (\rho_q^{n+1} U_f^{n+1} \alpha_{q,f}^{n+1}) = 0 \quad (75)$$

Explicit approach:

$$\frac{\alpha_q^{n+1}\rho_q^{n+1} - \alpha_q^n \rho_q^n}{\Delta t} V + \sum_f (\rho_q U_f^n \alpha_{q,f}^n) = 0 \quad (76)$$

Where n+1 is the index of the current time step, n is the index of the previous time step, $\alpha_{q,f}$ is the face value of the q[th] volume fraction (computed from the first, second-order upwind, QUICK, modified HRIC, compressive or CICSAM scheme), V is the volume of cell and U_f is the volume flux through the face based on normal velocity.

Implicit advection of interface is used to model the oil-injected compressor as this scheme allows for large solution time steps [108].

Appendix 3.3 Solution-based cell refinement

Refinement of the cell based on the oil volume fraction gradient can efficiently capture complex deforming interface, as shown in Figure 88a.

This refinement in Ansys Fluent [108] is an equidistribution adaptation technique [108]. It multiplies the undivided Laplacian of the selection solution variable, which is the oil volume fraction by a characteristic length scale (equation (77)).

$$|e_{i2}| = (A_{cell})^{\frac{r}{2}} |\nabla^2 f| \quad (77)$$

Where e_{i2} is the error indicator, A_{cell} is the computational cell area, r is the gradient (or derivative) volume weight, and $\nabla^2 f$ is the undivided Laplacian of the desired field variable (oil volume fraction).

If the domain begins as a single cell marked for adaptation, smaller cells can be created by recursive subdivision of the parent cell into children cells until a desired level of refinement is achieved. The cell size will depend on the refinement level. If we designate the unit square to be level 0, then the size of any cell is $l = (\frac{1}{2})^{level}$. If the parent cell is full (α=1) or empty (α =0), all child cells will have volume fractions of one or zero, respectively. If the parent cell contains an interface, the volume fraction of each child cell is determined geometrically, as illustrated in Figure 88b from the reconstruction of the interface in the parent cell. Refinement shown here involves dividing a cell into four child cells and determining the volume fraction for each child. Coarsening is simpler to refinement as the volume fraction of a parent cell is the average of the four child cells volume fractions.

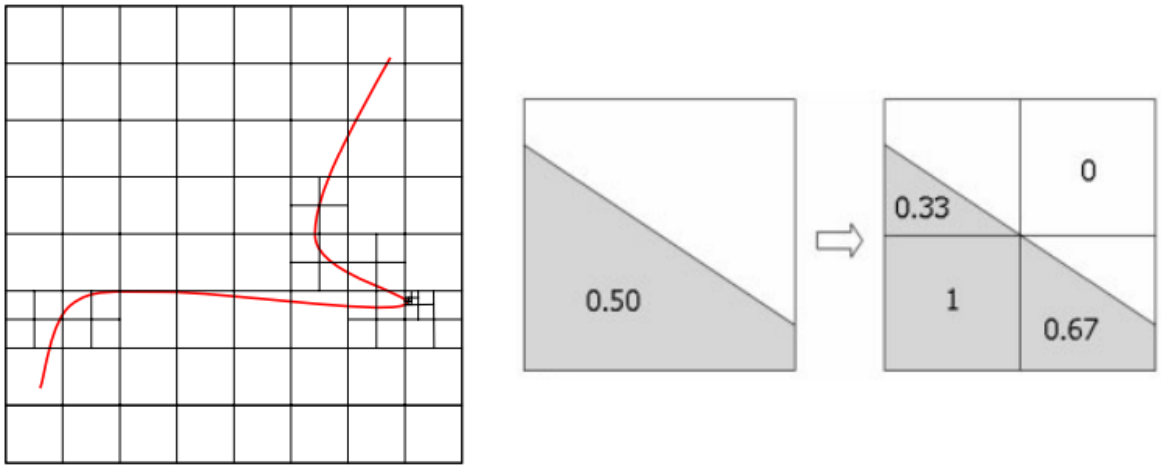

(a) (b)

Figure 88. (a) Refinement based on the volume fraction gradient and (b) Refinement: children cell volume fractions are calculated from the reconstructed interface in the parent cell [21].

Appendix 3.4 Comparison of two-phase models

The applied multiphase flow model depends on the dominant flow regime and grid scales. In a twin-screw compressor, a mixture of flow regime exists in the compression chamber with oil existing in the form of film as well as droplets.

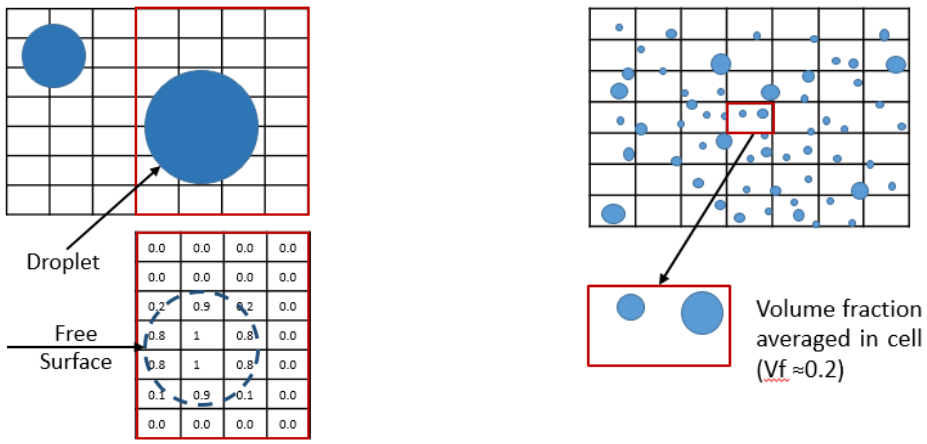

(a) (b)

Figure 89. Droplets bigger than grid scale- VOF model b, droplets smaller than grid scale – Mixture and Eulerian-Eulerian model.

Depending on grid scales, VOF is known to resolve better oil phase/droplet size bigger than grid scales. In contrast, the Mixture and Eulerian-Eulerian model is better in resolving droplets smaller than grid scales Figure 89. A free surface is obtained using a VOF model based on the cell volume fraction and interface tracking algorithm. Mixture properties are applied to the cells with partial volume fraction. On the other hand, for the Mixture/Eulerian- Eulerian model, phase properties are averaged based on volume fraction in discrete domain, and no free surface is obtained.

Table 35. Parameters considered within multiphase flow models.

	Suitability	**Continuity Equation (C)**	**Momentum Equation (M)**	**Energy Equation (E)**	**No. of equations solved**
Eulerian-Eulerian	Strong coupling between phases Ex: bubble columns, particle suspension and fluidised beds	Solved for each phase. 2 equations	-Separate equation for each phase -Strong coupling term between phases	Additional term for heat exchange	C-2 M-6 E- 2 Total:10
VOF	Interface present between the phases and is of interest Ex: Stratified, free-surface flows, annular flows	Single equation	-Single equation with properties mass averaged -No considered for interphase slip	-Single energy equation shared -Properties mass averaged in a cell	C-1 M-3 E- 1 VF -1 Total: 6
Mixture	Wide distribution of dispersed phases. Ex. Droplet laiden flows, sedimentation or cyclone separators	Single equation	-Single equation with properties mass averaged -Additional term on interphase forces and slip velocities	Similar to VOF	C- 1 M- 3 E- 1 VF- 1 Total: 6

The above-described multiphase models are summarised in Table 35. VOF model is generally used for the cases where there are deforming interfaces, and these interfaces are of interest. Eulerian-Eulerian model is a good fit when the flow regime is unknown and lift forces are of importance. Mixture model, in many cases, can be a good replacement for full Eulerian-Eulerian models, however, the slip velocities need to be formulated appropriately.

Appendix 4 Description of Ansys Fluent macros

UDF is used in Ansys Fluent to enhance the capabilities of the solver. UDFs are written in a 'C' programming language and are compiled before running the solver. Predefined macros are available in 'udf.h' library; these macros are utilised for executing the codes. Based on the macros, UDFs are executed before, during and after the solver run. All the macros need to be hooked for execution in the Ansys Fluent solver.

Following macros are used in this thesis to the development of a model suitable for an oil-injected twin-screw compressor.

1. DEFINE_ON_DEMAND

   The user executes this macro before or after the run. DEFINE_ON_DEMAND macro is used in this study for the purpose of node mapping before the calculation. Also, the temperature and volume fraction on cell faces is extracted for further processing.

2. DEFINE_GRID_MOTION

   This macro is used to control the motion of each node in the mesh. The solver executes it during the calculation. Under this macro, UDND code is written to translate the nodes with time-based on the positions generated from the SCORG grid generator.

3. DEFINE_CG_MOTION

   This macro is used to specify the motion of a specific dynamic zone by providing needed velocities at every time step and is executed by the solver during the transient calculation. In this study, the male rotor and female rotor rotational velocities and directions are specified under this macro.

4. DEFINE_PROFILE

   This macro is used for customising boundary conditions as a function of spatial coordinates or time. The solver executes it during the calculation. As already mentioned in this thesis, the pressure boundary condition at the outlet is ramped up with the time step to achieve full pressure. This is done for stability reasons, and the code is implemented under the DEFINE_PROFILE macro.